Spin-momentum locking in oxide interfaces and in Weyl semimetals

Nicandro Bovenzi

geboren te Capua (Italië) in 1989

On the cover: schematic illustration of two electrons with opposite spins
— one spinning clockwise and one anticlockwise — with respect to the
direction of the momentum (the yellow arrow). The momentum arrows
(on the front) bend and connect with arc segments (on the back) to form
closed orbits, that represent the two "lobes" of the figure–8 cyclotron orbit
(see Chapter 5).

To Vanna and to my parents

Contents

Contents

1 Introduction

1.1 Preface

Spin-orbit coupling is a relativistic effect: A charged particle moving in an electric field experiences a magnetic field in a frame of reference in which it is at rest. This magnetic field acts on the spin magnetic moment, resulting in a coupling of the spin to the motion (the "orbit"). For massless particles the coupling reaches the extreme limit that the spin direction is tied to the direction of motion. One speaks of *spin-momentum locking*.

Since the discovery of graphene we have become familiar with the notion that conduction electrons can have a vanishing effective mass and thereby exhibit relativistic effects at velocities much smaller than the speed of light. In graphene spin-orbit coupling is very weak but the electrons have a sublattice degree of freedom (a "pseudo-spin") that plays a similar role: it is oriented parallel to the momentum. Relativistic effects such as Klein tunneling emerge in graphene because of this pseudo-spin–momentum locking.

The topic of our thesis is to study the effects of spin-momentum locking in materials where it is the *real* spin, rather than a pseudo-spin, that is locked to the motion. We focus on two classes of materials: firstly on electrons confined to an oxide interface and secondly on the three-dimensional counterpart of graphene, known as a Weyl semimetal.

The remainder of this chapter is as follows. In Sec. 1.2 we introduce the topics of spin-orbit coupling and spin-momentum locking in condensed-matter systems. In Sec. 1.3 we discuss the electronic properties of interfaces in oxide heterostructures, with a focus on the high-mobility conducting system at the $LaAlO_3$ / $SrTiO_3$ interface and the investigation of its spin-orbit–driven physics through magnetotransport. In Sec. 1.4 the discussion shifts to Weyl semimetals, that offer the unique combination of gapless bulk spectrum, with relativistic energy–momentum relation, and topological surface states. For more accurate and self-contained treatments, references are provided throughout the text. We conclude with summaries of the following chapters.

1.2 Spin-orbit coupling and spin-momentum locking

The non-relativistic limit of the Dirac theory applied to atomic electrons leads to the Pauli Hamiltonian [1]

$$H_{SO} = -\frac{\hbar}{4m_0^2 c^2} \boldsymbol{\sigma} \cdot \boldsymbol{p} \times \boldsymbol{\nabla} V_0 \,, \tag{1.1}$$

that encodes the interaction between the spin magnetic moment — represented by the vector of Pauli operators $\boldsymbol{\sigma} = (\sigma_x, \sigma_y, \sigma_z)$ — and the kinetic momentum $\boldsymbol{p}$ of the electron. (V_0 is the electric potential of the atomic core, $\hbar$ the reduced Planck's constant, m_0 the bare electron mass and c the speed of light.)

In a solid crystal, electrons are subject to the periodic potential $V(\boldsymbol{r})$ of the ions' lattice. The eigenfunctions of the one-particle Hamiltonian

$$H(\boldsymbol{r}) = \frac{\boldsymbol{\nabla}^2}{2m} + V(\boldsymbol{r}) \tag{1.2}$$

are Bloch waves $\Psi_{n\boldsymbol{k}}(\boldsymbol{r}) = u_{n\boldsymbol{k}}(\boldsymbol{r})e^{i\boldsymbol{k}\cdot\boldsymbol{r}}$, where $u_{n\boldsymbol{k}}(\boldsymbol{r})$ is a periodic function with the periodicity of the lattice, and the eigenvalues $E_n(\boldsymbol{k})$ form bands as a function of the wave vector $\boldsymbol{k}$, labeled by the discrete index n.

The theory of electronic energy bands powerful tool that allows to classify "ordinary" materials in two big families: *insulators* and *metals*. The first ones have completely-filled (valence) bands that are separated by an energy gap from empty (conduction) bands, the second ones instead have partially-filled conduction bands. An insulator with a "small" gap between valence and conduction band can be made conducting via extrinsic doping, therefore it is called *semiconductor*. Semiconductors are the basic constituents of the electronic devices that we use in our daily life.

Spin-orbit coupling has remarkable effects on the band structure of semiconductors, such as splitting the spin-degeneracy of bands with finite angular momentum and enhancing — even by order of magnitudes — the Zeeman effect of an external magnetic field if the material lacks spatial-inversion symmetry [2].

Recently it has been realized that spin-orbit coupling can also lead to *topological* quantum states. For instance, due to large spin-orbit splitting in certain heavy-atom materials, valence and conduction bands are "inverted". Although a finite gap remains for the bulk spectrum, conducting (gapless) states appear at energies within the bulk gap, that are localized at the boundaries of the system and robust against disorder [3–5]. A bulk insulator
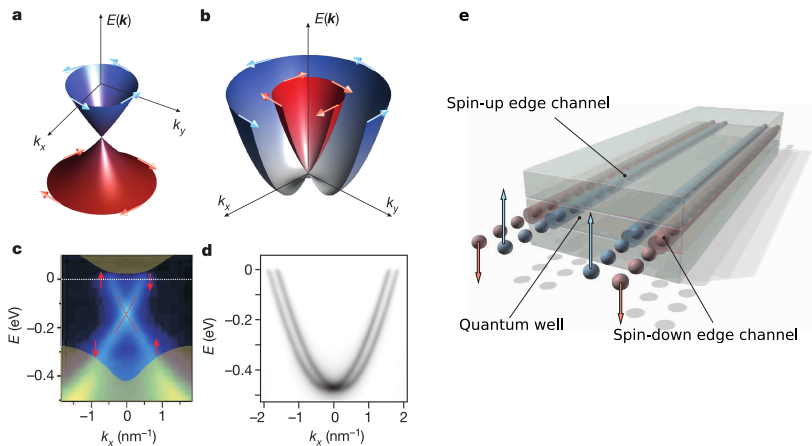
Figure 1.1: (a) Schematics of the helical spin structure of a Dirac cone at the surface of a three-dimensional topological insulator and (b) the chiral spin structure of two-dimensional parabolic bands with Rashba spin-orbit coupling. (c) ARPES measurements of the dispersion at the surface of the topological insulator $Bi_{2-x}Ca_xSe_3$ and (d) the surface of the normal metal Au(111) (plotted as a function of the momentum component k_x at a fixed k_y). Reprinted by permission from Springer Customer Service Centre GmbH: Springer Nature, Nature, A. Soumyanarayanan, N. Reyren, A. Fert and C. Panagopoulos, *Emergent phenomena induced by spin–orbit coupling at surfaces and interfaces*, Nature **539**, 509-517 (2016), Copyright 2016. Adapted by permission from Ref. 6, Nature Publishing Group. (e) Sketch of the conducting spin-polarized edge channels in a Quantum Spin Hall Insulator. From M. König, S. Wiedmann, C. Brüne, A. Roth, H. Buhmann, L. W. Molenkamp, X. L. Qi and S. C. Zhang, *Quantum Spin Hall Insulator State in HgTe Quantum Wells*, Science **318**, 766 (2007). Reprinted with permission from AAAS.

with conducting surfaces is topologically distinct from an ordinary insulator, thereby it is called *topological insulator*.

The combination of spin-orbit coupling and low-dimensionality, as e.g. at the surface of a topological insulator, gives rise to emergent physical effects in thin films and heterostructures [6]. The *Rashba effect* [7] at surfaces and interfaces describes the coupling between the inversion-symmetry–breaking electric field $\boldsymbol{E}$ along the out-of-plane $\boldsymbol{z}$-direction and the spin magnetic moment of itinerant electrons. The Rashba Hamiltonian for s electrons (without orbital angular momentum) has the form

$$H_{\mathrm{R}} = \alpha_{\mathrm{R}}\hat{\boldsymbol{z}} \cdot (\boldsymbol{p} \times \boldsymbol{\sigma}), \qquad (1.3)$$

where α_{R} is the coupling constant of the interaction, proportional to the electric field and to the intrinsic spin-orbit coupling.

In semiconductor-heterostructures, the magnitude of the Rashba effect can be electrically-modulated by means of external gates, that change

the interface electric-potential and thereby the effective magnetic field [8]. This striking feature is at the basis of the spin field-effect transistor theoretically proposed by Datta and Das [9], where the strength of the spin-orbit coupling controls the rate of the spin-precession, and through that, the electrical current carried by electrons injected by a ferromagnetic contact into a gated semiconducting region and extracted at an opposite ferromagnetic contact.

The (spin) Rashba effect produces linear-in-momentum energy splitting of opposite-spin states and constrains the electron spin to lie in the direction perpendicular to the momentum. This is an example of "spin-momentum locking", that can be generalized as a striking feature of surface (interface) states, such as:

- surface bands in ordinary metals [10],

- Dirac-cone states on the surfaces of three-dimensional topological insulators [11],

- edge channels in two-dimensional topological insulators (quantum spin Hall effect [12, 13]),

- Fermi-arc states in topological Weyl semimetals [14].

The basic picture of the Rashba effect becomes more complex when describing particles that have, in addition to the spin angular momentum, a finite orbital angular momentum, e.g. d electrons in oxide interfaces. In these systems, multiorbital effects produce a strong energy–dependence of the spin splitting and, at fixed energy, the magnitude of the splitting as a function of the momentum often deviates from linearity [15]. We can generalize the concept of spin-momentum locking in order to account for additional entanglement between spin and orbital polarizations.

1.3 Oxide interfaces

1.3.1 Transition-metal oxides

Transition metals are called the elements of the periodic table whose atoms either have an incomplete d subshell or can give rise to cations with an incomplete d subshell (IUPAC definition). They can form compounds with very different oxidation states: their oxide compounds (TMOs) show very interesting properties due to combination of the "hybrid" d electrons — partially bound to their own nuclei but with a certain freedom to interact

with neighboring atoms — and narrow electronic bands (between 1 and $2\,eV$) due to the small overlap between metal d orbitals and oxygen p orbitals. Hence, d electrons can show both itinerant and localized properties; the narrow band-width is expected to make electronic correlations relevant [16].

Two large subfamilies of the TMOs family are the *cuprates* and the *perovskites*. The former are famously known to show high-temperature superconductivity [17], the latter are among the most promising materials for highly efficient solar cells [18].

The perovskites have chemical formula AMO_3 and a cubic crystal structure, with the transition-metal (M) ion sitting at the center of the cubic cell, surrounded by an octahedron of oxygen (O) ions. and A ions at the eight corners. The crystal field generated by the O ions splits the five-fold degenerate d orbitals in two subsets, the lower-energy t_{2g} triplet (d_{xy}, d_{xz}, d_{yz} orbitals) and the higher-energy e_{2g} doublet ($d_{x^2-y^2}, d_{z^2}$).

Strontium titanate ($SrTiO_3$) has a long history as the *most dilute superconductor* — until the discovery of superconductivity in pure bismuth single crystals at ambient pressure and carrier density $n_e \approx 10^{15}\,cm^{-3}$ [19] — with a transition temperature $T_c \approx 300\,mK$ [20]. Although a long history of studies, the nature of the electron-electron pairing mechanism in strontium titanate is still questioned [21]. Above T_c, the material is a band insulator with a gap of $3.2\,eV$ and huge dielectric constant varying between $\epsilon_{STO} \approx 300$ at room temperature and $\epsilon_{STO} \approx 10000$ at sub-Kelvin temperatures [22].

Many TMOs have almost-matching lattice constants, whereby it is possible to grow layered heterostructures with atomic-size precision by placing one material on top of another layer by layer, using techniques developed in the context of semiconductor-heterostructures. Compared to the semiconducting counterparts, complex-oxide heterostructures are characterized by a richer mixing of different degrees of freedom — further enriched by the quantum confinement. Many oxide heterostructures are based on $SrTiO_3$, due to its important dielectric properties.

1.3.2 The LaAlO$_3$/SrTiO$_3$ interface

A paradigmatic example of this class of materials is the heterostructure formed by growing a thin film of lanthanum aluminate ($LaAlO_3$) on a substrate of $SrTiO_3$. Both materials are individually band-insulators. However, a breakthrough experiment reported evidence of electrical conductivity with high-mobility carriers at the interface of heterostructures grown along the (001) crystalline direction [23]. Since then, conducting
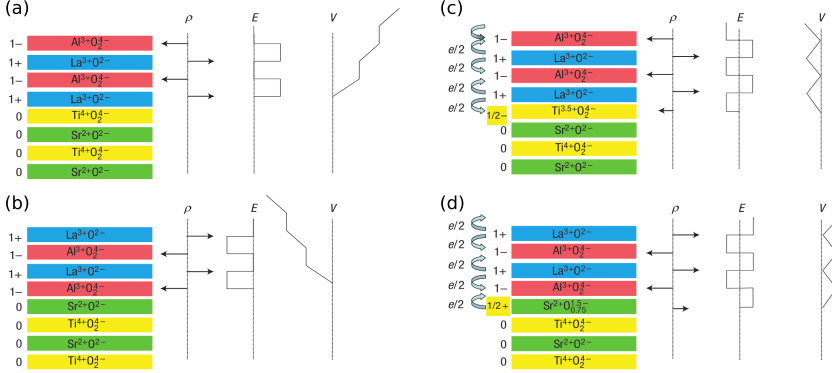
Figure 1.2: LAO / STO (001)–heterostructures are made of electrically neutral planes on the STO side and charged planes on the LAO side. (a)–(b) Charge density ρ, electric field E and potential V along the growth direction at the unreconstructed interface with (a) TiO$_2$-LaO connection and (b) SrO-AlO$_2$ connection. (c)–(d) Electronic reconstruction, with (c) half an electron per unit cell transferred to the TiO$_2$ interfacial plane and (d) half a hole transferred to the interfacial SrO plane, creates electric dipoles at the interface that leads to oscillating electric fields and bounded potentials. Reprinted by permission from Springer Customer Service Centre GmbH: Springer Nature, Nature Materials, N. Nakagawa, H. Y. Hwang and D. A. Muller, *Why some interfaces cannot be sharp*, Nat. Mater. **5**, 204–9 (2006), Copyright 2015.

interfaces were found in many SrTiO$_3$-based heterostructures [21]. Nevertheless most of the (theoretical and experimental) research in the field has focused on the LaAlO$_3$/SrTiO$_3$ interface (henceforth, LAO/STO).

The (001) LAO / STO heterostructure is made of alternating AO and MO$_2$ planes — A=La(Sr) and M=Al(Ti). LAO planes are electrically polarized with alternating $\pm e$ charge (per two-dimensional unit cell), instead STO planes are neutral. Two types of interface are formed depending on the termination layer of the STO substrate: a *n*-type interface if the termination layer is TiO$_2$ (TiO$_2$-LaO connectivity), a *p*-type interface in the case SrO-AlO$_2$ connectivity instead. The *n*-type interface becomes conducting when the thickness of the LAO film exceeds the threshold thickness of 3 unit cells, while the *p*-type interface does not show metallic behavior at any thickness [23, 24].

The origin of the interface conductivity is still debated. The *polar catastrophe* hypothesis [25] is consistent with many, but not all, the experimental observations. According to this hypothesis, a reconstruction of the electronic landscape of the interface occurs at a polar/non-polar junction in order to avoid the large cost in terms of electrostatic energy due to an unbounded growth of the electric potential in the bulk of the

polar material (see Fig. 1.2a–b).

The polar catastrophe mechanism predicts an insulator-metal transition (in *n*-type interfaces) as a function of the thickness of the LAO-film, when the bottom of the STO conduction band falls below the top of the LAO valence band, and charge-transfer is activated from the latter to the former. This prediction is consistent with the experiments. However, the electron density predicted by the polar catastrophe argument is much larger than the density of mobile electrons that is measured in transport [26, 27]. The discrepancy may be explained with the remaining electrons being bound at impurities or defects, thereby not contributing to the interface conductivity [28]. Moreover, conducting interfaces also exist in structures without polar discontinuity, as e.g. LAO / STO (110)– heterostructures [29].

Alternative proposals rely on the role played by oxygen-vacancies introduced in the system during the growth process [30–32].

1.3.3 Properties of the interface: superconductivity, magnetism, spin-orbit coupling

The huge STO dielectric constant allows to use electric gates to tune the charge-density of the interface between the fully-depleted regime and the overdoped regime with relatively low electric fields. The electric-field–dependence of physical properties such as spin-orbit coupling and superconductivity was experimentally reported [33, 34], that is a striking feature of the interface.

Regarding spin-orbit coupling, transport measurements clearly highlight the importance of it, although we are still waiting for ARPES (Angle Resolved Photo-Emission Spectroscopy) experiments that can resolve spin-split electronic bands. Signatures of weak-antilocalization peaks and their evolution as a function of the applied gate-voltage suggest that the magnitude of the spin-orbit coupling (spin-splitting) sharply increases of an order of magnitude at a doping level that seems to correlate with the appearance of superconductivity [35].

The density(voltage)-temperature phase diagram reveals a superconducting dome peaked at temperature $T_c^{max} \sim 300 \, mK$ (very close to the critical temperature of bulk STO) and at a density in proximity of a Lifshitz transition [36], where the topology of the Fermi surface is altered by the appearance of additional bands. Contrary to the dome-structure of T_c, the magnitude of the superconducting gap measured (locally) via tunneling spectroscopy is found to increase both in the underdoped and in the overdoped regime [37], suggesting either the presence of a *pseudogap*

phase like high-T_c superconductors [38] or that the system is spatially inhomogeneous, with coexisting superconducting and insulating (metallic) patches of nanometric size. In this scenario, patches with different densities would turn superconducting at slightly different temperatures, leading to a characteristic tail in the resistance-vs-temperature curves [39–41], unlike the usual sharp transition in homogeneous superconductors.

Signatures of inhomogeneous ground states of the interface appeared in magnetometry experiments [30, 42, 43] — that measured a ferromagnetic response superimposed to a diamagnetic (superconducting) signal. The inhomogeneity may be intrinsic, as the result of an electronic phase separation due to self-consistent adjustments of the confining potential that can make a homogeneous phase thermodynamically unstable [44]. However, alternative theoretical proposals pointed out that an exotic homogeneous phase that allows coexistence of superconductivity and magnetism, such as the FFLO (Fulde-Ferrel-Larkin-Ovchinnikov) phase [45], may be established in the system.

Interface superconductivity is a property inherited by the bulk STO parent compound. Instead, magnetism is an emergent property of the LAO / STO interface, since both LAO and STO are non-magnetic materials. Magnetic properties of the interface have been directly probed by means of many different techniques — Torque Magnetometry, SQUID Magnetometry, X-Ray Magnetic Circular Dichroism, Polarized Neutron Reflectometry, Magnetic Force Microscopy — and indirectly through magnetotransport measurements, with rather controversial outcomes. Even there are experiments that only measured finite magnetization at insulating interfaces and no signal in the conducting regime [46]. Many different groups have provided lots of magnetotransport whose interpretation is still subject of active research. A number of experimental signatures have been interpreted as originating from a Kondo–type interaction [47] between localized magnetic moments and delocalized electrons [48]:

- non-monotonic temperature–dependence of the sheet resistance [49];

- non-monotonic low-field Hall resistivity [36];

- giant negative magnetoresistance and crystalline anisotropy, with all-in-plane magnetic field [50];

- anomalous Hall effect [50].

However, the interaction-based interpretation of these observations was recently challenged by new experimental results obtained by Caviglia's group at Delft University [51] for the case of in-plane magnetic field.
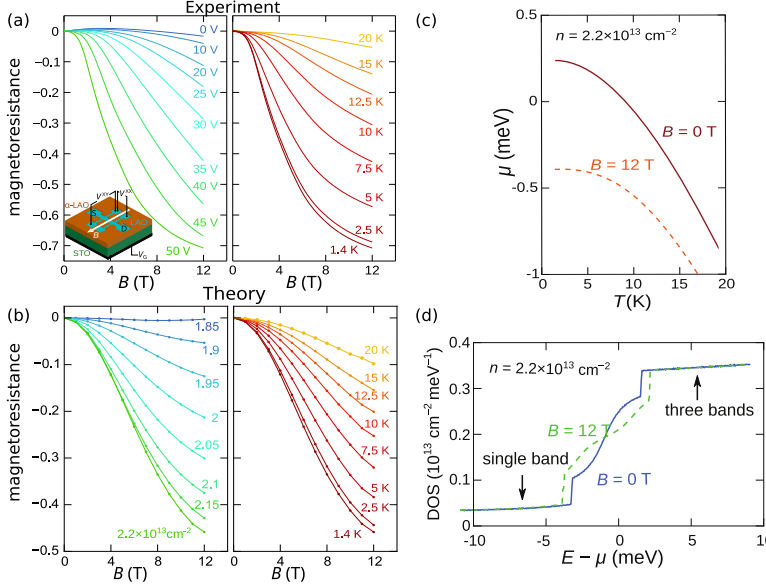
Figure 1.3: (a) Measured magnetoresistance of the LAO/STO interface, at temperature $T = 1.4\,K$ for several values of the gate voltage V_G (left panel) and at $V_G = 50\,V$ for various temperatures. (b) Magnetoresistance calculated within the semiclassical transport theory, at fixed temperature $T = 1.4\,K$ for various carrier-densities (left panel) and at density $n = 2.2 \times 10^{13}\,cm^{-2}$ for various temperatures. (c) Temperature–dependence of the chemical potential μ and (d) density of states, calculated from the Hamiltonian 2.1 for an electron density $n = 2.2 \times 10^{13}\,cm^{-2}$. Reprinted figures with permission from M. Diez, A. M. R. V. L. Monteiro, G. Mattoni, E. Cobanera, T. Hyart, E. Mulazimoglu, N. Bovenzi, C. W. J. Beenakker and A. D. Caviglia, *Giant negative magnetoresistance driven by spin–orbit coupling at the LaAlO$_3$ / SrTiO$_3$ interface*, Phys. Rev. Lett. **115**, 016803 (2015). Copyright (2015) by the American Physical Society.

Besides reporting a large negative magnetoresistance (up to 70% less than the zero-field resistance, in agreement with previous experiments), the experiments addressed the gate-voltage– and the temperature–dependence of the magnetoresistance, systematically, reporting that:

- the negative magnetoresistance survives up to $\sim 20\,K$;

- the "critical" field, namely the value of the magnetic field where the the slope of the magnetoresistance vs. field curves becomes negative, increases with the temperature;

- a striking similarity of the temperature–dependence (at fixed voltage) and the voltage–dependence (at fixed T) of the magnetoresistance.

9
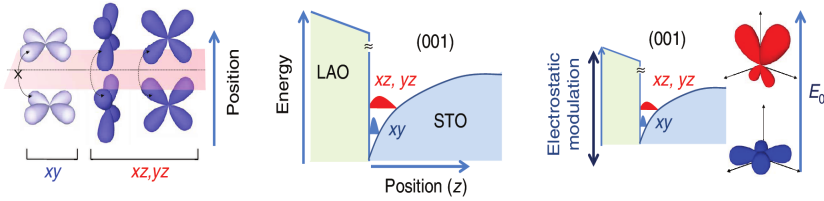
Figure 1.4: Confined orbitals in the quantum well at the (001) LAO / STO interface. Reprinted with permission from G. Herranz, G. Singh, N. Bergeal, A. Jouan, J. Lesueur, J. Gázquez, M. Varela, M. Scigaj, N. Dix, F. Sánchez and J. Fontcuberta, *Engineering two-dimensional superconductivity and Rashba spin–orbit coupling in LaAlO$_3$ / SrTiO$_3$ quantum wells by selective orbital occupancy*, Nat. Commun. **6**, 6028 (2015).

These observations required an alternative explanation, that is the subject of the theoretical work in Ref. 51. A semiclassical transport model for non-interacting electrons, that accounts for including multiorbital effects due to spin-orbit coupling and scattering by extended impurities, can qualitatively reproduce the features listed above. In particular, the striking similarity of temperature– and density–dependence of the magnetoresistance naturally arises from the renormalization of the chemical potential as a function of the temperature (see Fig. 1.3c).

Henceforth we refer to the mobile interface electrons as a two-dimensional electron gas (2DEG).

1.3.4 Band-structure model of the interface electron gas

Experiments report a dependence of the frequency of the conductance oscillations (Shubnikov–de Haas effect) only on the perpendicular component of the field [27, 52], as for a conventional two-dimensional electron gas. This means that the envelope wave function in the out-of-plane z-direction exists only in the lowest energy subband of the quantum well, although it can still extend over several unit cells away from the interface [53].

For the theoretical calculations of Chapter 2 we used the tight-binding model introduced in Ref. 48, that describes the conduction band of STO surface states. Restricting to the low-energy t_{2g} subspace, the Hamiltonian is calculated in the basis $|d_{xy}, \uparrow\rangle |d_{xy}, \downarrow\rangle |d_{xz}, \uparrow\rangle |d_{xz}, \downarrow\rangle |d_{yz}, \uparrow\rangle |d_{yz}, \downarrow\rangle$. The minimum of the band is at the Γ-point.

The orbital degeneracy of the bulk bands is partially removed due to the quantum confinement — d_{xy} orbitals have weak bonding along the out-of-plane direction — that results with the pair of d_{xy} bands, "light"
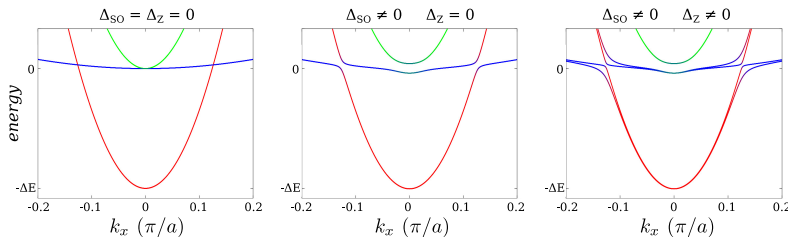
Figure 1.5: Band structures from diagonalization of the Hamiltonian 2.1, for three cases: only kinetic energy H_L; with atomic spin-orbit coupling H_SO (center); with both atomic spin-orbit coupling and inversion-symmetry breaking H_Z (right).

(small effective mass) and isotropic, having lower energy than d_{xz} / d_{yz} bands, that are "light" in one in-plane direction and "heavy" in the other one.

The intrinsic spin-orbit coupling, inherited from the atomic orbitals, is an off-diagonal matrix in this basis, thereby it mixes spin and orbital polarizations. The main effects on the band structure are to remove the remaining orbital degeneracy between d_{xz} and d_{yz} states at the Γ point and to produce hybridized $d_{xy}/d_{xz}(d_{yz})$ states, opening gaps in correspondence of band-crossing points.

Finally, hopping elements between orbitals with different parity under $(x, y, z) \rightarrow (x, y, -z)$ transformation are non-zero in the absence of inversion symmetry [54]. These are next-nearest-neighbor spin-preserving processes between the even d_{xy} orbitals and the odd d_{xz}/d_{yz} orbitals.

In combination with the intrinsic spin-orbit coupling, this term produces a strongly energy–dependent spin-splitting, that abruptly increases near the hybridization gaps. More details about the Hamiltonian and the band structure are provided in Sec. 2.6 of Chapter 2.

1.4 Weyl Semimetals

1.4.1 Weyl fermions in crystals

Accidental degeneracies in the band structure of three-dimensional solids — where low-energy excitations have linear energy–momentum relation — are not rare [55]. However these degeneracies are lifted by any weak perturbation unless they are enforced by symmetry constraints or by the so-called "topological invariants" of the band structure.

Symmetry-protected Dirac points exists both in two-dimensional (e.g. graphene) and in three-dimensional systems. Instead, the topologically-protected Weyl points are a unique property of three-dimensional crystals.

Each Weyl point (node) is a monopole of Berry curvature (a sort of momentum-space analog of the magnetic field) with a charge $\chi = \pm 1$ depending on the flux enclosed by a sphere surrounding the point. The sign determines the *chirality* (the "handedness") of the Weyl-fermion's wave function in real space.

Chiral fermions must always occur in pairs of opposite chirality according to the Nielsen-Ninomiya theorem [56] – in other words, the total Berry flux across the Brillouin zone must vanish. The low-energy physics around the Weyl point with chirality $\chi = \pm 1$ is governed by the Weyl Hamiltonian [57], that in momentum representation is

$$H_W = \chi v_F (p_x \sigma_x + p_y \sigma_y + p_z \sigma_z), \tag{1.4}$$

where $\sigma_{\alpha\,(\alpha=x,y,z)}$ are Pauli matrices and p_α the components of the crystal momentum $\boldsymbol{p} = \hbar \boldsymbol{k}$. The low-energy excitations have isotropic conical dispersion, with velocity v_F and the spin parallel or antiparallel to the momentum. Although Eq. (1.4) looks just like a trivial generalization of the two-dimensional graphene Hamiltonian, the third dimension enables topological protection to the band-touching points. Weyl cones cannot be gapped by local perturbations, as the only effect of adding a mass term $m\sigma_\alpha$ to H_W is of moving the Weyl cones around the Brillouin zone. The only way to make chiral fermions disappear is to pair them up, merging Weyl cones with opposite chirality that lead to the creation of a gap in the energy spectrum.

In order to acquire topological protection against local perturbations, a Weyl semimetal must not be invariant under the product of time-reversal and inversion symmetry. (If both symmetries are present, the Berry curvature is identically zero at any $\boldsymbol{k}$-point).

More "flavors" of Weyl fermions can exist in the band-structure of three-dimensional crystals, where the effective low-energy theory is not constrained by Lorentz invariance, that instead forces the energy-momentum relation of a fundamental particle to be independent of the direction where the particle travels. Therefore, Weyl cones are often anisotropic and tilted — the tilting is realized by adding the term $\propto p_\alpha \sigma_0$ to the Weyl Hamiltonian. In some materials the distortion can be so strong that it tips the cone over the momentum axis p_α, realizing a topologically distinct class of protected band touchings, the type–II Weyl points. These protected crossing points connect electron-like and hole-like states coexisting at the energy of the Weyl point [58].
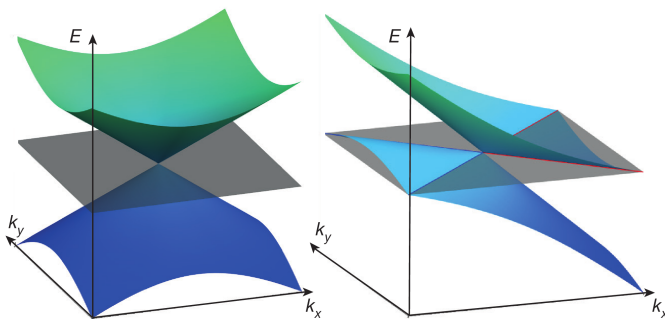
Figure 1.6: Type–I (left) and type–II (right) Weyl cones as a function of the momentum components k_x, k_y (at $k_z = 0$). The type–II Weyl cone has finite density of states at the energy of the Weyl node. Up to linear terms in the energy-momentum dispersion the equi-energy contours near the Weyl-node energy are open. On a lattice, higher-order terms close the contours. Reprinted by permission from Springer Customer Service Centre GmbH: Springer Nature, Nature, A. A. Soluyanov, D. Gresch, Z. Wang, Q.S. Wu, M. Troyer *et al.*, *Type–*II *Weyl semimetals*, Nature **527**, 495-98 (2015), Copyright 2015.

Furthermore, combinations of point-group symmetries of the crystal structure [59] can force more Weyl points with same chirality to merge, producing Berry monopoles with topological charge larger than one. These are called "multi–Weyl" points. Type–II and multi–Weyl points are studied in Chapter 5.

1.4.2 Lattice model of time-reversal–symmetry breaking Weyl semimetals

For lattice simulations, we use the tight-binding model of a time-reversal–symmetry breaking Weyl semimetal on a cubic lattice (with lattice parameter $a \equiv 1$) introduced in Ref.132, defined by the Hamiltonian

$$H_{\mathrm{W}}(\boldsymbol{k}) = \tau_z(\sigma_x t_x \sin k_x + \sigma_y t_y \sin k_y + \sigma_z t_z \sin k_z)$$
$$+ m_{\boldsymbol{k}}\tau_x\sigma_0 + \beta\tau_0\sigma_z + \lambda\tau_z\sigma_0 - \mu_{\mathrm{W}}\tau_0\sigma_0, \qquad (1.5a)$$
$$m_{\boldsymbol{k}} = m_0 + t'_x(1 - \cos k_x) + t'_y(1 - \cos k_y)$$
$$+ t'_z(1 - \cos k_z). \qquad (1.5b)$$

The σ and τ Pauli matrices refer to a spin and orbital degree of freedom, σ_0 (τ_0) is the 2×2 identity matrix in spin (orbital) space. t_α and t'_α are respectively kinetic hopping and spin-dependent hopping terms —

originating from spin-orbit coupling. The mass term $m_{\boldsymbol{k}}$ ensures that the spectrum is gapped everywhere except at $\boldsymbol{k} = (0, 0, \pm K)$, with

$$K^2 \approx \frac{\beta^2 - m_0^2}{t_z^2 + t'_z m_0} \tag{1.6}$$

where the origins of two Weyl cones with opposite chirality are located. β (λ) is the parameter that breaks time-reversal (inversion) symmetry providing a difference in momentum (energy) of the two Weyl points.

The Hamiltonian 1.5a is mathematically equivalent — up to a unitary transformation and redefinition of the τ degree of freedom — to the model of Ref. 63, where Weyl fermions are engineered in the phase diagram of a multilayer heterostructure realized by alternating layers of a magnetically doped topological insulator (such as Bi_2Se_3) and normal-insulator layers. Although experimentally very challenging, the latter model is fascinating also because by replacing the normal-insulator layers with thin films of *s*-wave superconductor, it is predicted to realize a *Weyl superconductor* [60]. We make use of the heterostructure models in Chapter 3 in the context of Andreev reflection in Weyl superconductor – Weyl semimetal junctions.

1.4.3 Surface states

A closed system whose bulk band structure exhibits Weyl fermions is further characterized by a special type of surface states. To understand how the surface states arise, let us consider two Weyl cones centered at momenta $\chi \boldsymbol{k}_0 = (\chi k_0, 0, 0)$ and let us slice the 3D Brillouin zone in a series of planes, parametrized by the momentum component k_x. To each plane corresponds a two-dimensional band structure that has a gap for all values of k_x except for $k_x = \pm k_0$. A Chern number is associated to each gapped band structure as:

$$\mathcal{C}_{k_x} = \frac{1}{2\pi} \int_{S_{k_x}} d\boldsymbol{S}_{k_x} \cdot \boldsymbol{\Omega}_{\boldsymbol{k}} \tag{1.7}$$

with

$$\boldsymbol{\Omega}_{\boldsymbol{k}} = \boldsymbol{\nabla}_{\boldsymbol{k}} \times \boldsymbol{A}_{\boldsymbol{k}} \quad \boldsymbol{A}_{\boldsymbol{k}} = \sum_n i \langle u_{n\boldsymbol{k}} | \boldsymbol{\nabla}_{\boldsymbol{k}} | u_{n\boldsymbol{k}} \rangle , \tag{1.8}$$

where $\boldsymbol{A}_{\boldsymbol{k}}$ is the Berry potential summed over all filled bands labeled by the index n an $u_{n\boldsymbol{k}}$ are Bloch states.

By tuning the parameter k_x continuously, the system undergoes a topological phase transition with gap closing and reopening across a Weyl point, that is accompanied by a change of the Chern number of the planes. Planes with $|k_x| < k_0$ carry non-zero Chern numbers, hence they support
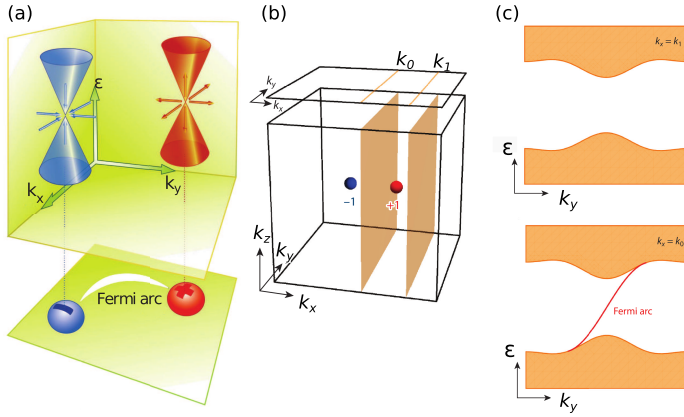
Figure 1.7: (a) Pair of opposite-chirality Weyl cones in the three-dimensional Brillouin zone. (b) Graphic argument for the development of the Fermi arcs from connecting edge states of the Chern insulators defined by the band structure on two-dimensional slices of the Brilluoin zone in between the Weyl nodes. (c) At $k_x = k_1$ (top) the effective two-dimensional Hamiltonian describes a trivial insulator (Chern number $\nu = 0$) with a gapped bulk spectrum and no edge states. At $k_x = k_0$ (bottom) instead the band structure has non-trivial Chern number $\nu = \pm 1$, that corresponds to the presence of one edge state within the bulk gap. Adapted from Ref. [14].

chiral states propagating along the edges. The surface bands appear on the two-dimensional surface by joining together edge states supported by the non-trivial planes in-between the Weyl points. The intersection of the surface bands with the Fermi energy generates open curves that connect the projections of the Weyl points onto the surface Brillouin zone, that are called "Fermi arcs".

In real space, the surface states are "chiral", meaning that they circle around the magnetization axis in a single direction. If inversion symmetry is broken they acquire finite velocity along the magnetization axis; in cylinder geometry with the Weyl points along the axis of the cylinder, the surface states form a solenoid structure [61].

However, Fermi arcs on opposite material's surfaces must be thought as complementary parts of a single Fermi surface. Indeed, in thin-film Weyl semimetals arcs on top and bottom surfaces merge to form a closed equi-energy contour. Interestingly, when both time-reversal and inversion symmetry are broken in a Weyl thin-film, the intersection of the constant energy planes with the lowest energy subband produces a figure-8, that is topologically distinct from simple deformations of the Fermi circle in conventional 2DEGs. Magnetotransport signatures of this Fermi surface
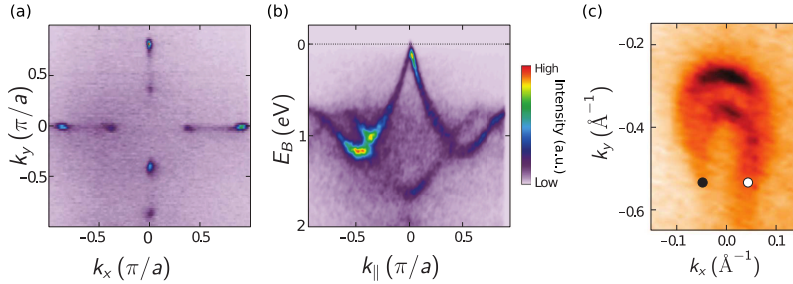
Figure 1.8: (a) ARPES-measured dispersion on the surface Brillouin zone and (b) in the bulk of the recently discovered TaAs Weyl semimetal. (c) High-resolution image of two Fermi arcs terminating at the projections of opposite-chirality Weyl nodes. From S.-Y. Xu, I. Belopolski, N. Alidoust, M. Neupane, G. Bian, *et al.*, *Discovery of a Weyl fermion semimetal and topological Fermi arcs*, Science **349**, 613 (2015). Reprinted with permission from AAAS.

are investigated in Chapter 4.

1.4.4 Experimental relizations

The search for a Weyl-semimetal phase initially focused on inversion-symmetric systems with broken time-reversal symmetry. Early proposals suggested magnetic pyrochlore iridates [62], multilayer heterostructures of alternating magnetically doped topological insulators and normal insulators [63], magnetically doped topological insulators at the critical point of transition to a normal insulator [64]. Moreover the recently discovered Dirac semimetals [65–67] — where the band-touching point is at leas four-fold degenerate due to crystalline symmetries — can be turned to a Weyl semimetal by splitting a single Dirac point into two Weyl points with a Zeeman field. All these proposals suffer a number of experimental challenges that prevented the realization of any of them to date.

Meanwhile, time-reversal–invariant Weyl semimetals have been brought to life: first in tantalum arsenide (TaAs), later in niobium arsenide (NbAs) and tantalum phosphide (TaP) [68] — all these materials break inversion symmetry and have 24 Weyl cones in the Brillouin zone — the bulk conical dispersion and the surface Fermi arcs where resolved with good resolution in ARPES experiments.

Transport signatures of a magnetic Weyl semimetal were identified in different topological Heusler compounds [69, 70] and, very recently, evidences for a magnetic Weyl semimetal have been reported in photoemission

data from the correlated manganese-tin alloy (Mn$_3$Sn) [71], an hexagonal antiferromagnet with a stacked Kagome lattice.

1.4.5 Chiral anomaly and related magnetotransport signatures

Weyl fermions in condensed-matter systems are predicted to show the *chiral anomaly* [72, 73] — the non-conservation of the currents carried by the individual chiral species in the presence of parallel electric and magnetic field [74]. The anomaly manifests itself as the pumping of chiral electrons between oppositely charged Weyl points, leading to "valley" polarization. The anomaly is a general feature of chiral fermions in odd spatial dimensions. Its simplest one-dimensional version only requires an electric field, whose action on the electron dynamics is given by the semiclassical equation of motion $dk/dt = eE/\hbar$. If right-moving and left-moving carriers are connected at high energies (as is the case of any realistic band-structure), change of momentum implies transferring electrons from the left-moving to the right-moving Weyl point. As a result the difference between the densities of left and right movers n_L and n_R grows according to

$$\frac{d(n_R - n_L)}{dt} = 2\frac{e}{h}E \ . \tag{1.9}$$

This is the chiral anomaly in one-dimensional systems. The right-hand-side of Eq. (1.9) will have an additional term that oppose to the growth of the left-hand-side if the density imbalance can be relaxed via inter-node scattering. In the three-dimensional space, the quantizing effect of the magnetic field is necessary to recover an effective one-dimensional transport problem. Indeed an external magnetic field produces Landau levels that disperse only in the direction of the field. The Landau level with quantum number $n = 0$ in a Weyl semimetal is chiral, namely it has velocity parallel or antiparallel to field-direction, depending on the chirality of the Weyl node from where it is generated. If an electric field is applied parallel to the magnetic field, electrons start propagating along one-dimensional chiral channels, that have cross-sectional area (divided by the number of the degenerate states) $\mathcal{A} = \phi_0/B$, the ratio between the flux quantum and the magnetic field. Therefore, formula 1.9 holds, upon substituting E with $\boldsymbol{E} \cdot \hat{\boldsymbol{B}}$ and and dividing by the cross sectional area $\mathcal{A}$ to obtain the three-dimensional density. Although no current in equilibrium is allowed, in a non-equilibrium setup the chiral anomaly result in a contribution to the total electrical current of a Weyl semimetal that leads to the longitudinal

negative magnetoresistance [75–77] and the chiral magnetic effect with and without Landau levels [78, 79].

1.5 This thesis

1.5.1 Chapter 2

The study of magnetotransport effects, in connection with spin-orbit coupling, at the LAO /STO interface requires more theoretical efforts that may help interpret the experiments. The work presented in this chapter extends the results of Ref. [51]. Here we address — by applying the semiclassical transport theory to spin-coupled electrons scattered by extended impurities on the plane of the interface — the anisotropy of the longitudinal magnetoresistance under in-plane magnetic fields, that was reported by several experimental groups in recent years, but not reproduced by any theoretical model so far.

We calculate the full resistivity tensor as a function of the orientation of the in-plane field, for different values of the field-strength and several electron densities. The results show that the high-field angular-modulation of the magnetoresistance has a behavior similar to what observed in the experiments: because of the peculiar spin-orbital-momentum locking of the states at the Fermi level, the largest contributions to the resistance come from *inter-band* scattering processes, that are extremely sensitive to the applied magnetic field. Finally, we show that a sizable Hall resistivity is possible even in the absence of an orbital magnetic field and/or magnetic impurities. Unlike the longitudinal magnetoresistance, the Hall signal is due to *intra-band* scattering processes. We also comment on the differences with respect to the experiments.

1.5.2 Chapter 3

A Weyl semimetal with broken time-reversal symmetry (*magnetic Weyl semimetal*) has a minimum of two species of Weyl fermions, distinguished by their opposite chirality. Therefore, a hydrogen-atom model of the band structure of a (unbounded) magnetic Weyl semimetal consists of a pair of Weyl cones at opposite momenta $\pm K$ that are displaced in the direction of the internal magnetization. In the presence of inversion symmetry, the (pseudo)spin degree of freedom of a Weyl fermion with positive (negative) chirality is tied parallel (antiparallel) to its kinetic momentum.

At a normal-metal/superconductor junction, an electron injected from
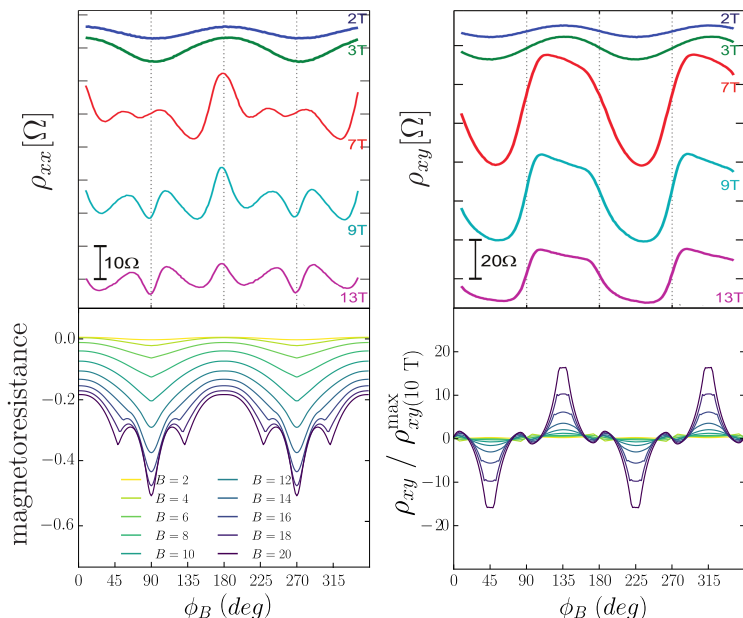
Figure 1.9: (Top) Experimental measurements of the longitudinal (ρ_{xx}) and Hall (ρ_{xy}) resistivity of a Hall-bar device patterned at the LAO/STO interface, as a function of the angle ϕ_B between the current and an in-plane magnetic field. The chemical potential is presumably above the Lifshitz point. Reprinted with permission from A. Joshua, J. Ruhman, S. Pecker, E. Altman and S. Ilani, *Gate-tunable polarized phase of two-dimensional electrons at the LaAlO₃ / SrTiO₃ interface*, Proc. Natl Acad. Sci., **110**, 9633 (2013). (Bottom) Theoretical calculations of the in-plane magnetoresistance and Hall resistivity (renormalized by the maximum at $B = 10$ T), from Ref. [80]. (These quantities have same angular modulations as ρ_{xx} and ρ_{xy} respectively.)

the metal contact at energy lower than the superconducting gap can be reflected by the interface as a hole, with an additional Cooper pair transferred to the superconductor. This process, called *Andreev reflection*, converts a dissipative current into a (dissipationless) supercurrent.

In the specific case of the interface between a Weyl semimetal in the normal state (N) and a superconductor (S) that pairs electrons at $\pm K$, Andreev reflection must involve a switch of chirality, otherwise it is blocked as long as inversion symmetry is preserved and the internal magnetization of the Weyl semimetal lies in the plane parallel to the NS interface.

The blockade requires the combination of conical dispersion of the Weyl semimetal and spin-momentum locking, thereby it is not a general property of materials with relativistic dispersions. A Zeeman field at the interface

or breaking inversion symmetry can activate Andreev reflection.

1.5.3 Chapter 4

The spectrum of a Weyl semimetal confined to a slab-geometry has a gap for the bulk states, while the dispersion of the surface states is insensitive to the spatial confinement as long as there is no overlap between states on opposite surfaces. Therefore, at energies close to the Weyl points of the unbounded system electrons in the slab have hybrid surface/bulk character depending on the momentum.

The Fermi surface of a conventional two-dimensional electron gas is equivalent to a circle, up to smooth deformations that preserve the orientation of the equi-energy contour. Instead, we show in this chapter that a thin-film magnetic Weyl semimetal with additionally broken inversion symmetry can have a topologically distinct two-dimensional Fermi surface, twisted into a figure-8 — opposite orientations are coupled at a crossing which is protected up to an exponentially small gap due to overlap between wave-functions localized at opposite surfaces.

The topology of the Fermi surface can be probed via quantum oscillations of magnetization (De Haas–Van Alphen effect) or conductance (Shubnikov–De Haas effect) in the presence of an external magnetic field. The frequencies and phase shifts of the oscillations can be extracted from the semiclassical Landau levels, that for this particular system we have computed numerically.

The spectral response of the twisted Fermi surface is distinct from that of a deformed Fermi circle, because the two lobes of a figure-8 cyclotron orbit give opposite contributions to the Aharonov-Bohm phase acquired by the electron wave-function when completing a full orbit. In a strong magnetic field, two counter-propagating types of quantum Hall edge channels appear at the boundaries, when the system is further confined to a strip. However, when an electrical current is driven through the system between two metal reservoirs, only one of the two co-propagating channels is populated, providing unique magnetotransport signatures. For instance, the edge along which the current propagates can be changed by reversing the direction of the magnetic field.

1.5.4 Chapter 5

The work of this chapter was motivated by one of the main results of Chapter 4, that is the value of the phase offset $\gamma = \pi$ obtained as the quantum correction to the semiclassical quantization condition applied to

the figure-8 cyclotron orbit in a thin-film Weyl semimetal. This valued of the phase offse differs from the value $\gamma = 0$ offset found for a different type of figure-8 cyclotron orbit, as the energy of the Weyl point in a type–II Weyl semimetal [81].

This apparent inconsistency and the increasing interest in identifying topological semimetals in quantum-oscillation experiments, require a better understanding of how the phase shift encodes information about the topological features of the band structure.

Here we predict the characteristic parameter dependence of the phase shift for Weyl fermions with tilted and overtilted dispersion (type–I and type–II Weyl fermions) and an arbitrary topological charge, including elliptical and 8-shaped Fermi surfaces. Remarkably, for type–II Weyl fermions the phase shift only depends on the quantized topological charge, being insensitive to the specifics of the band structure.

2 Semiclassical theory of anisotropic transport at LaAlO$_3$ / SrTiO$_3$ interfaces

The development of *quantum-matter heterostructures* paves the way to the realization of novel electronic states, due to the combination of the capabilities and rich variety of heterostructure engineering, the collective interactions of complex oxides, and the emergent properties of quantum materials [82, 83].

A paradigmatic example is the heterostructure formed by the transition-metal oxides LaAlO$_3$ and SrTiO$_3$. Since the experimental demonstration of electrical conduction at the interface between these two materials [23], large attention has been drawn to this system in particular due to its gate-tunable superconductivity [33, 34, 84] at $T \lesssim 300$ mK. At slightly higher temperatures — in the range $1 - 20$ K — magnetotransport has been an important tool for the investigation of electronic and magnetic properties of the interface that are believed to be strongly determined by mixing of charge, spin, orbital and lattice degrees of freedoms.

A number of signatures in the normal-state transport [49, 50, 85, 86], such as giant negative magnetoresistance, crystalline anisotropy, anomalous Hall effect and their striking change of behavior when the system is tuned across a Lifshitz transition [36] have been considered as an evidence of magnetism at the interface. In particular, Ruhman et al. [48] suggested that the action of the field on the interaction between conduction electrons and localized magnetic moments induces a phase transition from a Kondo-screened (high and isotropic resistance) phase to a (low and anisotropic resistance) polarized phase, where the unscreened moments act as magnetic scatterers.

However, experimental investigations of the magnetic landscape at the interface [30, 42, 43, 87–89] reported qualitatively different results. A strong ferromagnetic phase with large total magnetization was recently observed by magnetic force microscopy [46] at room-temperature in the depleted (insulating) regime of top-gated interfaces. On the other hand,

the total magnetization was found to disappear when the interface was doped enough to be conducting. More questions about the origin and the nature of magnetism at low temperature remain to be answered.

A particular type of spin-orbit coupling at the interface is produced by the interplay of atomic spin-orbit interaction (intrinsic to d electrons) and the next-nearest-neighbour hopping from d_{xy} to d_{xz}/d_{yz} orbitals, a process that is forbidden in the bulk due to inversion symmetry, but it is activated at the interface. Spin-splitting without magnetic field has been experimentally measured: the magnitude of the splitting is strongly dependent on the position of the Fermi level (tuned via external gate-voltage) and seems to increase steeply in the overdoped regime [35, 84, 90]. Motivated by the experimental observations, models including tunable spin-orbit coupling through an explicit density–dependence of the parameters have been applied to study thermodynamic properties of the interface, pointing out the possibility of realizing electronic phase separation in a self-consistent manner [91, 92]. Furthermore, controllable spin-orbit interaction offers a way to achieve room temperature spin-charge conversion and generation of spin currents [93] for spintronics implementations.

However, spin-orbit coupling was often considered to be too small of an effect to contribute to the transport properties of the interface on a much bigger scale than quantum corrections. Contrary to this belief, Diez *et al.* [51] demonstrated that the semiclassical conductivity of spin-orbit coupled electrons scattered by extended impurities is surprisingly very sensitive to an in-plane magnetic field, that may explain the large drop of the in-plane magnetoresistance (up to 70% reduction at $B = 12$ T) measured by the experiments. Furthermore, the semiclassical model provides a simple explanation for the striking similarity between gate-voltage– and temperature–dependence of the magnetoresistance.

Here we use the same semiclassical framework to investigate the dependence of the full resistivity tensor as a function of the magnitude and the in-plane orientation of the magnetic field, revealing the onset and peculiar evolution of a strongly anisotropic response. The large anisotropy survives within a range of chemical potentials such that multiple electronic subbands, with different dispersions and orbital polarizations, are populated at the same time. In this regime, the anisotropic magnetoresistance comes from a complex interplay of inter-band and intra-band scattering processes.

The structure of the chapter is as follows. In Sec. 2.1 we report and discuss the results of two magnetotransport experiments at LaAlO$_3$/SrTiO$_3$ interfaces. In Sec. 2.2 we introduce the various ingredients of the theoretical model employed for transport calculations. In Sec. 2.3 we present the

numerical results. In Sec. 2.4 we extensively discuss how our results arise from the interplay of spin-orbit coupling and magnetic field that dramatically affects the amplitudes of scattering between Bloch states. Sec. 2.5 contains a final summary and outlook. Details about the parameters of the model and additional results are provided in the Appendices.

2.1 Anisotropic planar magnetotransport: experimental signatures

To date there is a very broad collection of experimental studies [26, 36, 42, 49–52, 84–86, 90, 94] of the conducting (001) LAO/STO interface in the presence of an external magnetic field $\boldsymbol{B}$. Here we restrict to electrical transport at low temperature (yet above the superconducting critical temperature $T_c \approx 300$ mK), and to magnetic field applied in the plane of the interface.

First striking observation is the abrupt change of the qualitative behavior of the measured resistance when the carrier density is tuned across the Lifshitz point in the band structure of the interface [36]. by tuning the density of carriers via an applied gate voltage. Joshua *et al.* [50] reported the angular–dependence of the longitudinal (ρ_{xx}) and transverse (ρ_{xy}) resistivity measured at a Hall-bar device, by tuning the carrier density with a back-gate (back-gated), as a function of the planar angle between the current running between source and drain contacts and applied field. At low gate-voltage ρ_{xx} depend very weakly on the orientation ϕ_{B} of the magnetic field relative to the direction of the current, and the maximum and minimum resistivity are measured along the crystalline axes. At high voltage the response of the system is extremely sensitive to the magnetic field: a large drop in ρ_{xx} while increasing the field-strength occurs above a characteristic field B_c of order of a few T. The latter is shown to have a dependence on the gate-voltage V_{G}, e.g. decreasing while increasing V_{G} and diverging while approaching the Lifshitz point from above. Moreover the magnetoresistance is strongly anisotropic and its angular modulation is considered as the signature of a change of some symmetry of the system. Additional peaks and dips points appears at intermediate angles. The percentage of anisotropy measured at $B = 14$ T is about 20% of the average resistivity. Along with that, the authors report an abrupt increase of the transverse resistivity ρ_{xy} by increasing the field. At a field larger than 10 T, ρ_{xy} becomes comparable to ρ_{xx} and characterized by a striking step-like angular modulation.

The magnitude of ρ_{xy} and its symmetry ($\rho_{xy} \simeq \rho_{yx}$) rule out any relevant contributions of the orbital field due either to minimal misalignment between the direction of $\boldsymbol{B}$ and the plane of the interface, or to the finite extension of the gas in the out-of-plane direction. The *crystalline* symmetry of the anisotropic response is revealed by the evolution of the direction of the principal axes of the resistivity tensor. While at low voltage (density) the principal axes follow the direction of $\boldsymbol{B}$, at high voltage and high magnetic field the principal axes are pinned to diagonal directions ($45°, 135°, 225°, 315°$): the directions where maximum and minimum resistivity are measured do not depend on the orientation of the magnetic field.

Similar behavior on different samples was previously reported by Ben Shalom *et al.* [85] who also investigated the temperature–dependence of the effect. Sharp minima (maxima) of the longitudinal resistivity are measured when the magnetic field is perpendicular (parallel) to the current. The magnitude of the high-field anisotropy is consistent with the finding of Joshua *et al.* [50] and is suppressed on the same temperature-scale which governs the magnetoresistance [51].

2.2 Electronic structure and the Boltzmann equation with correlated disorder

The low-energy electronic structure is obtained from the single-particle Hamiltonian introduced by Ruhman *et al.* [48]. In terms of creation (annihilation) operators $c_{\boldsymbol{k},l,\sigma}^{\dagger}$ ($c_{\boldsymbol{k},l,\sigma}$) of an electron with momentum $\boldsymbol{k}$ in the $l = (d_{xy}, d_{xz}, d_{yz})$ orbital, the tight-binding Hamiltonian is

$$\mathcal{H} = \sum_{\boldsymbol{k},l,l',\sigma,\sigma'} c_{\boldsymbol{k},l,\sigma}^{\dagger} \, H_{l\sigma,l'\sigma'}(\boldsymbol{k}) \, c_{\boldsymbol{k},l',\sigma'}$$

$$H = H_{\mathrm{L}} + H_{\mathrm{SO}} + H_{\mathrm{Z}} + H_B \,, \tag{2.1}$$

including the kinetic term H_{L}, the atomic spin-orbit coupling H_{SO}, the inversion-symmetry-breaking inter-orbital coupling H_{Z} and the Zeeman coupling of the magnetic field with spin and angular orbital momentum (see Sec. 2.6 for the details).

The energy spectrum near the Lifshitz point is plotted in Fig. 2.1. At low density only d_{xy} bands are populated and the effective spin-orbit interaction of ordinary Rashba-type, with coupling constant $\alpha_{\mathrm{R}} \sim \Delta_{\mathrm{Z}}\Delta_{\mathrm{SO}}/\Delta_{\mathrm{E}}$ [95] (Δ_{Z} and Δ_{SO} are the inversion-symmetry breaking and atomic spin-orbit parameter respectively, see Sec. 2.6.) A change in the topology of the

Figure 2.1: (Top) Dispersion at $k_y = 0$ near the Lifshitz point, obtained by numerical diagonalization of the Hamiltonian 2.1. Different orbital polarizations are distinguished by different colors. (Bottom) Equi-energy contours at $\epsilon - \mu = 0$, showing the average spin and orbital angular momentum. Blue (yellow) arrows refer to the outermost (innermost) band of each pair. The complete set of parameters used for generating the plots are listed in the first row of Table 2.1 (Sec. 2.7).

Fermi surface occurs at a threshold density, due to the onset of occupation of a new pair of bands.

The interplay of H_{SO} and H_Z produces strong orbital hybridization and spin-splitting for electronic states at points in the Brillouin zone where light and heavy bands would cross each other at $H_{SO} = H_Z = 0$. In the absence of magnetic field, analytical expressions for the effective Rashba-like coupling of the surface states of $SrTiO_3$ and $KTaO_3$ were derived by Kim *et al.* [96]. A similar derivation (valid near the Γ-point) was worked out by Zhou *et al.* [97]. Here we resort to numerical diagonalization of the Hamiltonian including the Zeeman coupling $H_B = \mu_B(\boldsymbol{L} + g\boldsymbol{S}) \cdot \boldsymbol{B}/\hbar$ of the magnetic field $\boldsymbol{B}$ with the orbital ($\boldsymbol{L}$) and spin ($\boldsymbol{S}$) angular momentum.

As shown in Fig. 2.1, at $T = 0$ the Fermi level is characterized by two small surfaces, elongated along the symmetry axes of the crystal, and two larger and less anisotropic ones. Importantly, the group velocity $\boldsymbol{v}_{\boldsymbol{k},\nu} = \hbar^{-1}\partial\epsilon_{\boldsymbol{k},\nu}/\partial\boldsymbol{k}$ is no longer parallel to the momentum for large sections of the Fermi surfaces.

We calculate the expectation-value of the spin and orbital angular momentum operators on the eigenstates. At $B = 0$, the z-component of both is quenched to zero because of time-reversal and π-rotation symmetry around the z-axis and will stay zero as long as the magnetic field has no component in the out-of-plane direction. Following the evolution of the expectation-value of the spin on the large Fermi surfaces in the top-right quadrant of the Brillouin zone ($\vartheta < 90°$), it is found to be parallel to the y-axis at small ϑ (small k_y), it suddenly undergoes a 90°-rotation in the vicinity of $\vartheta = 45°$ and finally aligns to the x-axis at $\vartheta > 45°$. The magnitude of the average orbital angular momentum is peaked near the hybridization gaps while it is very small on the remaining sectors of the Fermi surfaces. Electronic spectrum and the spin-orbital structure at the Fermi level are consistent with the data reported by King *et al.* [98] for the surface states of SrTiO$_3$.

The eigenstates $|\psi_{\boldsymbol{k},\nu}\rangle = |u_{\boldsymbol{k},\nu}\rangle e^{i\boldsymbol{k}\cdot\boldsymbol{r}}$ and the eigenvalues $\epsilon_{\boldsymbol{k},\nu}$ of the Hamiltonian 2.1 enter the Boltzmann transport equation

$$- e(\boldsymbol{v}_{\boldsymbol{k},\nu} \cdot \boldsymbol{E})\frac{\partial f_0}{\partial\epsilon_{\boldsymbol{k},\nu}} = \sum_{\boldsymbol{k}',\nu'}(g_{\boldsymbol{k},\nu} - g_{\boldsymbol{k}',\nu'})q_{\boldsymbol{k}\nu,\boldsymbol{k}'\nu'}\delta(\epsilon_{\boldsymbol{k},\nu} - \epsilon_{\boldsymbol{k}',\nu'})\,, \quad (2.2)$$

that returns returning the out-of-equilibrium shift $g_{\boldsymbol{k},\nu}$ in the electron distribution function due to an accelerating electric field $\boldsymbol{E}$ and scattering by impurity centres. $f_0(\epsilon)$ is the equilibrium Fermi-Dirac distribution function and $\boldsymbol{v}_{\boldsymbol{k},\nu} = \hbar^{-1}\partial\epsilon_{\boldsymbol{k},\nu}/\partial\boldsymbol{k}$. Spatial correlations between different impurities can be introduced via a Gaussian potential

$$U(\boldsymbol{r}) = \sum_i U_i e^{-|\boldsymbol{r}-\boldsymbol{r}_i|^2/\xi^2}\,. \quad (2.3)$$

where the amplitudes U_i of the individual scatterers are randomly distributed with uniform probability in the symmetric range $[-\delta/2, \delta/2]$ and ξ is the characteristic decay-length of the two-point correlator (that is Gaussian as well).

At leading order in the Born approximation and averaging over the ensemble of impurity configurations, the amplitude of elastic scattering from the initial state $|u_{\boldsymbol{k}\nu}\rangle$ to the final state $|u_{\boldsymbol{k}'\nu'}\rangle$ is

$$q_{\boldsymbol{k}\nu,\boldsymbol{k}'\nu'} = \tfrac{2}{3}\pi^3\hbar^{-1}\delta^2\xi^4 n_{\text{imp}}\, e^{-\xi^2|\boldsymbol{k}-\boldsymbol{k}'|^2/2}|\langle u_{\boldsymbol{k}\nu}|u_{\boldsymbol{k}'\nu'}\rangle|^2\,, \quad (2.4)$$

n_{imp} being the density of impurities.

An alternative model was considered by Fu *et al.* [99] who calculated the density–dependence of the resistivity in multi-subband accumulation layers (heterojunctions of polar and non polar perovskites such as LAO and STO) where electrons are scattered by the potential generated by surface roughness. In their model, spatial disorder-correlations decay exponentially. In momentum-space, the elastic scattering amplitude

$$q_{\boldsymbol{k}\nu,\boldsymbol{k}'\nu'} = \frac{2\pi^2\delta^2\xi^2}{\hbar}n_{imp}(1 + \xi^2|\boldsymbol{k} - \boldsymbol{k}'|^2)^{-3/2}|\langle u_{\boldsymbol{k}\nu}|u_{\boldsymbol{k}'\nu'}\rangle|^2 \qquad (2.5)$$

decays algebraically as a function of the momentum transferred to the impurity ($q_{\boldsymbol{k}\nu,\boldsymbol{k}'\nu'} \propto |\boldsymbol{k} - \boldsymbol{k}'|^{-3}$ at large $|\boldsymbol{k} - \boldsymbol{k}'|$). The scattering with large momentum-transfer (and hence backscattering) is stronger for this model than for the Gaussian model of Eq. (2.4).

Here we only consider scalar impurities, described by single-impurity-potential operators that are diagonal in the basis of the unperturbed Hamiltonian. The scattering processes can occur from a band to itself ("intra-band"), or to a different one("inter-band").

We present results of magnetotransport calculations for two models of disorder — Gaussian-correlated impurites and surface-roughness — that show a similar behavior of the fixed-density magnetoresistance, albeit the density–dependence of bare resistance may be substantially different in the two cases [99].

2.3 Numerical results

At linear order in the electric field $\boldsymbol{E}$, the out-of-equilibrium distribution $g_{\boldsymbol{k},\nu}$ is in terms of the band– and momentum–dependent vector mean-free-path $\boldsymbol{\Lambda}_{\boldsymbol{k},\nu}$ [100] is

$$g_{\boldsymbol{k},\nu} = -e(\partial f_0/\partial\epsilon_{\boldsymbol{k},\nu})\boldsymbol{E} \cdot \boldsymbol{\Lambda}_{\boldsymbol{k},\nu}. \qquad (2.6)$$

Eigenvalues $\epsilon_{\boldsymbol{k},\nu}$ and eigenvectors $u_{\boldsymbol{k},\nu}$ of the Hamiltonian 2.1 are calculated numerically. for each value of the in-plane magnetic field ($B\cos\phi_B, B\sin\phi_B$), where ϕ_B is the angle measured counterclockwise from the x-axis. The electron density is kept constant at any B. as a consequence, therefore the chemical potential $\mu(B,\phi_B) \equiv \mu(B)$ is determined self-consistently according to

$$n_e = \int_{\epsilon_0}^{\infty} d\epsilon\, f_0\big(\epsilon, \mu(B), T\big)\, N(\epsilon)\,, \qquad (2.7)$$

where $N(\epsilon)$ is the density of states at energy ϵ and ϵ_0 the energy of the bottom of the lowest conduction band.

The conductivity tensor $\boldsymbol{\sigma}$ follows from the distribution function as

$$(\boldsymbol{\sigma})_{ij} = e \sum_{\boldsymbol{k},\nu} (\boldsymbol{v}_{\boldsymbol{k},\nu})_i \frac{\partial g_{\boldsymbol{k},\nu}}{\partial E_j}. \tag{2.8}$$

By matrix-inversion of $\boldsymbol{\sigma}$ we finally extract the longitudinal resistivity and the transverse resistivity, as

$$\rho_{xx} = \frac{\sigma_{yy}}{\sigma_{xx}\sigma_{yy} - \sigma_{xy}^2} \ , \ \rho_{xy} = -\frac{\sigma_{xy}}{\sigma_{xx}\sigma_{yy} - \sigma_{xy}^2}. \tag{2.9}$$

In this section we show the results of calculations performed at a temperature $T = 1$ K and a carrier-density $n = 2.2 \times 10^{13}\,\text{cm}^{-2}$, corresponding to a chemical potential crossing the second pair of bands. Two bands remain a few meV ($\approx \Delta_{\text{SO}}/2$) higher than μ and do not play any role here since we only consider elastic scattering. (The spin-orbit gap between d_{xz} and d_{yz} states is much larger than the thermal broadening of the Fermi-Dirac distribution.)

In Fig. 2.2 the magnetoresistance $\rho_{xx}(B)/\rho_{xx}(0) - 1$ and the transverse resistivity ρ_{xy} are plotted as a function of the angle ϕ_B, for values of B between 2 and 20T. The transverse resistivity has been rescaled by its maximum value at $10\,\text{T}$ — obtained around $\phi_{\text{B}} = 45°$ — in order to get a quantity that (as the magnetoresistance) is independent of the parameters n_{imp} and δ. In the range $4 - 10\,\text{T}$ (at lower fields the effects are moderate) the angular modulation of the magnetoresistance has cusp-like dips at $\phi_{\text{B}} = 90°, 270°$ (magnetic field perpendicular to the current) and rounded maxima at $\phi_{\text{B}} = 0°, 180°$ (magnetic field aligned to the current). The magnitude of the negative magnetoresistance and the anisotropy progressively increase with the field-strength. The transverse resistivity has a sinusoidal modulation with maxima and minima shifted by $45°$ with respect to the magnetoresistance extrema. However ρ_{xy} is two orders of magnitude smaller than ρ_{xx}. Above $10\,\text{T}$, the angular magnetoresistance develops additional maxima and minima near diagonal orientations ($\phi_B = 45°, 135°, 225°, 315°$) that unlike the main extremal points – fixed at multiples of $90°$ – do not only move up and down but also shift in angular position as the field is progressively increased. In the same field-range where these additional features characterize the magnetoresistance, ρ_{xy} increases by (more than) one order of magnitude. Another striking feature is the change in the angular modulation of the transverse resistivity that substantially deviates from the sinusoidal low-field behaviour. Other parameters are considered in Sec. 2.7.
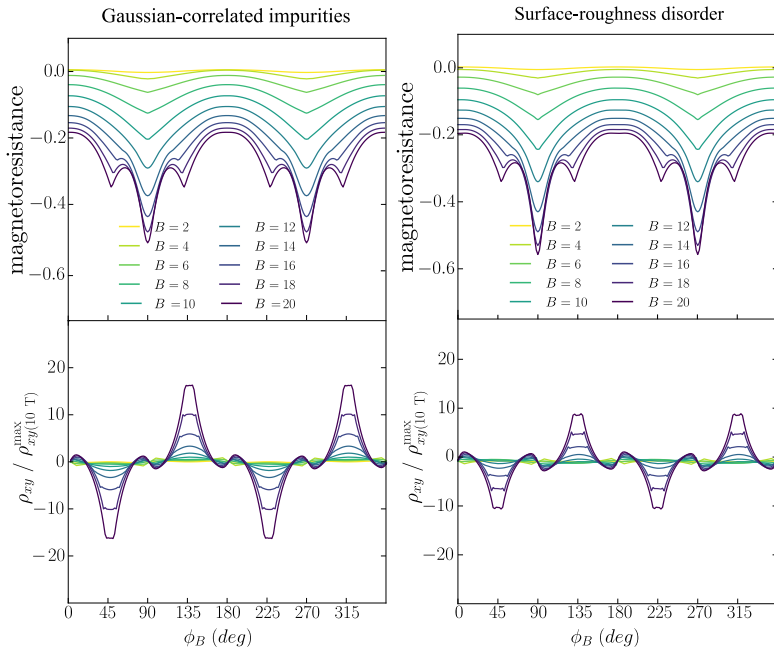
Figure 2.2: (Top) Magnetoresistance $\rho_{xx}(B)/\rho_{xx}(0) - 1$ and (bottom) transverse resistivity ρ_{xy} (rescaled by the maximum ρ_{xy} at $B = 10\,\mathrm{T}$), as a function of the angle between the direction of the magnetic field and the x-axis, at different values of the field-strength. The left panel is for calculations with scattering by Gaussian-correlated impurities, with amplitudes from Eq. (2.4). The right panel is for calculations with scattering by surface-roughness disorder, with amplitudes from Eq. (2.5). The temperature is $T = 1\,\mathrm{K}$ and the density $n = 2.2 \times 10^{13}\,\mathrm{cm}^{-2}$. Other parameters from the first row of Table 2.1 (Sec. 2.7).

The B–dependence of the magnetoresistance at different angles ϕ_B is shown in Fig. 2.3. Amplitude, shape and the field-scale of the magnetoresistance, all change with ϕ_B. Moving from a configuration with magnetic field parallel to the direction of the current ($\phi_\mathrm{B} = 0°$) towards the opposite configuration ($\phi_\mathrm{B} = 90°$), the magnitude of the magnetoresistance grows by a factor ~ 3 at 20 T. Moreover, the field-scale where the slope of the magnetoresistance becomes negative – and large in magnitude – decreases by moving the field away from the direction of the current. The results are consistent with previous calculations [51] of the magnetoresistance at $\phi_B = 90°$, albeit here calculated in a different spin-orbit–coupling regime (see Sec. 2.7). The angular-maximum of the transverse resistivity ρ_{xy} exhibits a strong enhancement around starting at $\sim 10\,\mathrm{T}$ for the Gaussian
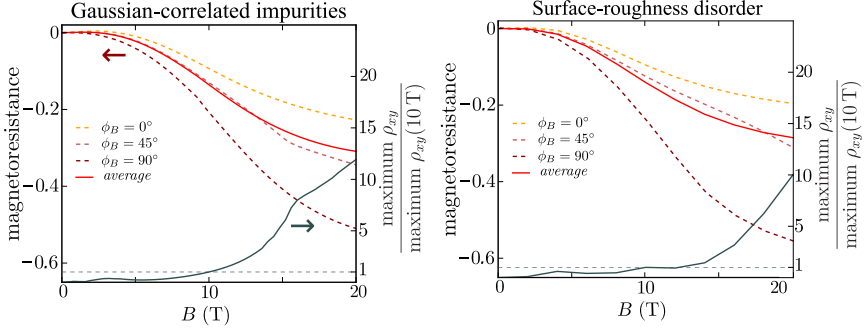
Figure 2.3: Magnetoresistance as a function of the field-strength, for different values of the angle ϕ_B (dashed lines) and after averaging over all angles (solid red line); The solid gray line represents the field–dependence of the (angular) maximum of ρ_{xy} divided by its value at $B = 10$, that is taken as a reference value. (Left) Scattering amplitudes from Eq. (2.4). (Right) Scattering amplitudes from Eq. (2.5).

model (slightly higher field for the exponential model).

The slope of $\rho_{xy}(B)$ softens at the very high fields, where the magnetoresistance at $\phi_B = 45°$ shows the onset of saturation in the case of Gaussian disorder-potential. For the other model, instead, the curvature of the magnetoresistance at $\phi_B = 45°$ is still negative at $B = 20\,T$ (no saturation in this field-range) that also produces a non-saturating ρ_{xy}.

2.4 Discussion

At $T = 0$ only electrons at the Fermi level contribute to the conductivity of a metal. In favour of a clearer discussion, hereafter we neglect the effects of a finite low temperature — these are crucial quantitatively, but do not alter the underlying mechanism.

At densities much lower than the threshold density of the Lifshitz transition ($n_e \ll n_L$), the chemical potential $\mu(B)$ — determined at any B self-consistently according to Eq. (2.7) — lies deep into the d_{xy} bands, that have a tiny k-linear Rashba splitting [95]. In this regime, the anisotropy is extremely weak (less than 1%) (see Fig. 2.7 in Sec.2.7). A previous work shows that even the inclusion of spin-selective scatterering does not give any sizable anisotropy [101].

At densities slightly larger than n_L, instead, the chemical potential crosses the hybridization gaps where the spin-splitting is about ten times larger than at low density. We have not considered densities right at the

Lifshitz transition to avoid artifacts in the numerics due to the sudden appearance of band-edges where almost-zero Fermi momentum.

For the scattering models of Eq.(2.4) and Eq.(2.5), in the outermost bands — characterized by large Fermi surfaces and high band velocities — the backscattering is suppressed for correlation lengths much larger than the inverse of the average Fermi momentum. Hence, relaxation via intra-band scattering takes place on a slow time-scale (that includes many low-angle scattering events), while the most effective mechanism of velocity relaxation is provided by forward-scattering processes to the inner bands. Indeed, the inner bands have low mobilities, due to the small velocities and large intra-band scattering rates.

At $B = 0$ the spin-ordering near the hybridization gaps in the top-right quadrant of the Brillouin zone is $|\downarrow\rangle|\uparrow\rangle|\uparrow\rangle|\downarrow\rangle$ (see Fig. 2.1b). At some non-universal value of B (dependent on the specifics of the band structure), the ordering is reversed for the inner bands (not shown in the figure). This results in reduction of the scattering rates between pairs of states $(\mathbf{k}, \nu)$ and $(\mathbf{k}', \nu')$ that have minimal inter-band distances $|\mathbf{k} - \mathbf{k}'|$ and parallel spins at $B = 0$. The field-suppression of inter-band scattering leads to enhanced (reduced) longitudinal conductivity (resistivity) with increasing magnetic field. The enhancement is particularly large at orientations $\phi_{\mathrm{B}} = 90°, 270°$, where the magnetic field is aligned to the spin-orbit field acting on states with the highest velocity $v_{\mathbf{k},\nu}^x$ in the direction of the electric field.

The qualitative behavior changes for $B > 10\,\mathrm{T}$, because the intra-band scattering starts giving a non-negligible contribution. In Fig. 2.4 the calculated vectors mean-free-path $\mathbf{\Lambda}_{\mathbf{k},\nu}$ are plotted on top of the equi-energy contours at the Fermi level, for different magnetic-field configurations. At $\phi_{\mathrm{B}} = 45°$ (c–d), the magnetic field is far from the crystalline axis. The outermost contours (almost) cross each other at a polar coordinate $\vartheta = \overline{\vartheta} \approx 10°$, but not at the complementary angle $(90° - \overline{\vartheta})$ (top-right quadrant). As a consequence, the rates of scattering between d_{xy}–polarized (red) states — of polar coordinate $\overline{\vartheta} < \vartheta < 90° - \overline{\vartheta}$ — and hybrid d_{xy}/d_{xz} (purple) states at $\vartheta \approx \overline{\vartheta}$ are enhanced by the field, as opposed to the complementary-scattering rates.

To better illustrate the consequences of this, we formally express the

solution of the Boltzmann equation (2.2) in the recursive form

$$\boldsymbol{\Lambda}_{\boldsymbol{k},\nu} = \boldsymbol{v}_{\boldsymbol{k},\nu}\tau_{\boldsymbol{k},\nu} + \sum_{\boldsymbol{k}'\neq\boldsymbol{k}} q_{\boldsymbol{k}\nu,\boldsymbol{k}'\nu'} \Big\{ \boldsymbol{v}_{\boldsymbol{k}',\nu'}\tau_{\boldsymbol{k}',\nu'}$$
$$+ \sum_{\boldsymbol{k}''\neq\boldsymbol{k},\boldsymbol{k}'} q_{\boldsymbol{k}'\nu',\boldsymbol{k}''\nu''} \Big\{ \boldsymbol{v}_{\boldsymbol{k}'',\nu''}\tau_{\boldsymbol{k}'',\nu''}$$
$$+ \sum_{\boldsymbol{k}'''\neq\boldsymbol{k},\boldsymbol{k}',\boldsymbol{k}''} q_{\boldsymbol{k}''\nu'',\boldsymbol{k}'''\nu'''}\,\boldsymbol{v}_{\boldsymbol{k}''',\nu'''} + \cdots \Big\} \Big\}, \qquad (2.10)$$

where $\tau_{\boldsymbol{k},\nu}$ is the bare band– and momentum–dependent relaxation-time

$$\tau_{\boldsymbol{k},\nu} = \sum_{\boldsymbol{k}',\nu'} q_{\boldsymbol{k}\nu,\boldsymbol{k}'\nu'}. \qquad (2.11)$$

The low-angle scattering is strongly anisotropic, thereby the scattering-in corrections to the vector mean-free-path $\boldsymbol{\Lambda}_{\boldsymbol{k},\nu}^{\mathrm{RTA}} = \tau_{\boldsymbol{k},\nu}\boldsymbol{v}_{\boldsymbol{k},\nu}$ — calculated in relaxation-time approximation [102, 103] — substantially affect magnitude and direction of the vector mean-free-path, that gets tilted (away from the direction of the velocity $\boldsymbol{v}_{\boldsymbol{k},\nu}$) towards the direction of enhanced scattering ($\bar{\vartheta}$). The anisotropy of the scattering effectively acts as a Lorentz force, driving a shift of the electron distribution around the equi-energy contours [104, 105]. However, unlike the actual Lorentz force, magnitude and direction of this "effective Lorentz force" at a point $(\boldsymbol{k},\nu)$ change non monotonically as a function of the magnetic-field parameters B and ϕ_{B}, and so do the intra-band scattering rates. The direction of the tilting of the vector mean-free-path $\boldsymbol{\Lambda}_{\boldsymbol{k},\nu}$ may then undergo multiple reversals when the magnetic field changes in magnitude and/or direction, thereby the out-of-equilibrium distribution

$$g_{\boldsymbol{k},\nu} \propto \boldsymbol{\Lambda}_{\boldsymbol{k},\nu} \cdot \boldsymbol{E} \qquad (2.12)$$

can increase or decrease, depending on whether the direction of the tilt-ing "tends" to the direction of the electric field or not. The appearance of secondary maxima and minima (whose positions also change with B) of the magnetoresistance vs. field curves, when the field is along inter-mediate directions away from the crystalline axes, is explained by the field–dependence of the effective Lorentz force.

Unlike the longitudinal magnetoresistance, the transverse resistivity ρ_{xy} is entirely dominated by the intra-band scattering, that is the reason why it is substantially zero for $B < 10\,\mathrm{T}$. We need to look at the total contribution to the conductivity carried by states with opposite velocities
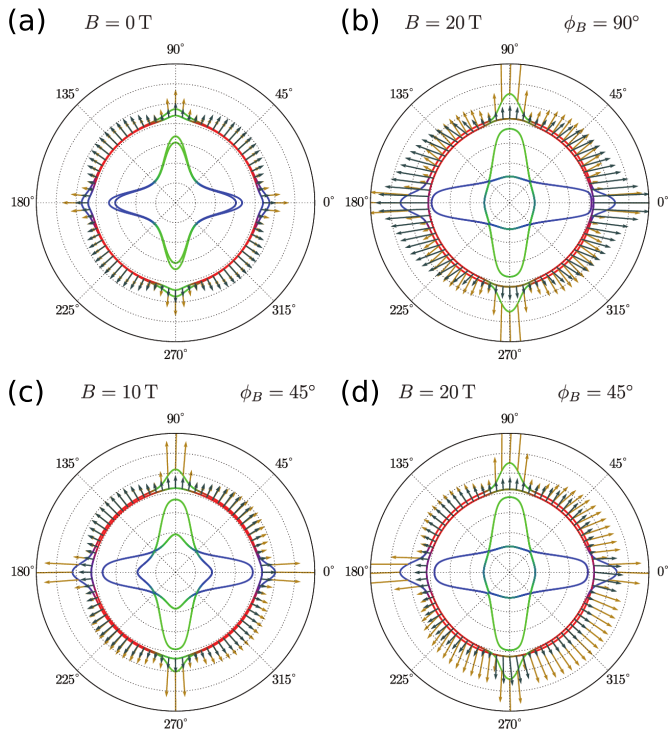
Figure 2.4: Fermi surfaces at $n = 2.2 \times 10^{13}\,\mathrm{cm}^{-2}$ for different configurations of the in-plane magnetic field: (a) $B = 0\,\mathrm{T}$, (b) $B = 20\,\mathrm{T}$ $\phi_B = 90°$, (c) $B = 10\,\mathrm{T}$ $\phi_B = 45°$, (d) $B = 20\,\mathrm{T}$ $\phi_B = 45°$. Magnitude and direction of the vector mean-free-path $\boldsymbol{\Lambda_k}$ as a function of the momentum $\boldsymbol{k}$ on the outermost bands (which support all of the total conductivity at any fields) are represented by arrows - colors distinguish the two bands of each pair. The longitudinal conductivity σ_{xx} is proportional to the average x-component of the vector mean-free-path. (At $\phi_{\mathrm{B}} = 0,\,90°$ $\rho_{xx} = \sigma_{xx}^{-1}$.) The modulation of the vector mean-free-path in (c) is mirror-symmetric with respect to the crystalline axes; therefore $\sigma_{xy}(\rho_{xy}) \approx 0$ because states with opposite velocities compensate each other with equal weights Λ^x. Instead in (d) the texture of the vector mean-free-path is manifestly asymmetric, producing sizable σ_{xy}.

in the direction perpendicular to the electric field and understand why an imbalance between their occupations is generated by the magnetic field. For the states in the bottom-right quadrant ($270° < \vartheta < 360°$), the scattering-in rates are large and isotropic, thereby they only affect the magnitude — but not the direction — of the vector mean-free-path. Hence $\boldsymbol{\Lambda}_{\boldsymbol{k},\nu} \propto \boldsymbol{v}_{\boldsymbol{k},\nu}$ still holds, although the proportionality coefficient deviates from the bare relaxation-time $\tau_{\boldsymbol{k},\nu}$. Similarly, states in the top-left quadrant of the Brillouin zone have $\boldsymbol{\Lambda}_{\boldsymbol{k},\nu} \propto \boldsymbol{v}_{\boldsymbol{k},\nu}$. However the latter receive smaller scattering-in corrections because the magnetic field does not reduce – but rather enhances – the spin-orbital splitting at any point in the quadrant. This imbalance is large enough to produce an unexpectedly-large ρ_{xy} ($\rho_{xy}/\rho_{xx} \approx 0.1$ at $B = 20\,\text{T}$) even in the absence of orbital effects of the magnetic field.

Finally, the angular modulation of ρ_{xy} sharply ramp up when the angle ϕ_B takes a value such that at isolated points in the Brillouin zone the spin-orbital splitting is totally suppressed by the Zeeman field. Once this occurs, the low-angle scattering abruptly develops a preferential direction, and then remains stable until the field is rotated far enough to let the spin-orbital splitting open again. This results in a flattening of the peaks of ρ_{xy} more or less pronounced in all the plots shown in this chapter.

2.5 Conclusions

In this work, we have investigated magnetotransport at the LaAlO$_3$ / SrTiO$_3$ interface with a simple theoretical model based on semiclassical Boltzmann transport. In particular, we have studied the dependence of the resistivity tensor on the magnitude and orientation of an in-plane magnetic field, leaving out the investigation of the effects of an orbital field.

Many-body effects, e.g. electron-electron [106, 107] and magnetic interactions [48, 50]), are neglected. Spin-orbit coupling effects on the low-energy states of the conduction band are included by means of an effective tight-binding model including three atomic orbitals. The Boltzmann equation (2.2) for electrons scattered by correlated impurities – with correlations decaying on a characteristic length scale ξ – is solved numerically as a function of the external field. Our main finding is a crossover from the low-field regime of weak anisotropy to the high-field regime of strong anisotropy which results from important changes in the electronic structure at the Fermi level when the carrier-density is tuned above the Lifshitz point [48]. However, we remark that is not simply the onset of the occupation of anisotropic bands to determine a change of

the magnetotransport properties, but rather the selective modulation of the impurity-scattering connecting pairs of states at the Fermi level. In presence of magnetic field, the spin-orbital structure of the Bloch states is locally modified depending on the relative orientation of spin-orbit and magnetic fields. In particular, the effect is enhanced in the vicinity of (avoided) band crossings when the component of the magnetic field on the local (band– and momentum–dependent) axis of the spin-orbit field is comparable to the magnitude of the latter. Scattering amplitudes *to* and *from* these states are then extremely sensitive to the magnitude and direction of the magnetic field. Our results are in good qualitative agreement with experiments [50], although some features of the experimental data remain not fully captured by our simple model.

2.6 Appendix A. Single-particle Hamiltonian

To model the conduction bands at the interface we use a single-electron Hamiltonian [48] where the electronic states are derived from the t_{2g} (d_{xy}, d_{xz} and d_{yz}) orbitals of Ti-atoms. Accounting for a total number of six degrees of freedom (three orbitals times two spin components), the translational invariant Hamiltonian in momentum space has a 6×6 matrix-representation that is the sum of the four terms in Eq. (2.1). The kinetic Hamiltonian

$$H_{\mathrm{L}} = \begin{pmatrix} \epsilon_{xy}(k) - \Delta_{\mathrm{E}} & 0 & 0 \\ 0 & \epsilon_{xz}(k) & \delta(k) \\ 0 & \delta(k) & \epsilon_{yz}(k) \end{pmatrix} \otimes \hat{\sigma}_0, \qquad (2.13)$$

$$\begin{aligned} \epsilon_{xy}(k) &= 2t_l(2 - \cos k_x - \cos k_y), \\ \epsilon_{xz}(k) &= 2t_l(1 - \cos k_x) + 2t_h(1 - \cos k_y), \\ \epsilon_{yz}(k) &= 2t_h(1 - \cos k_x) + 2t_l(1 - \cos k_y), \\ \delta(k) &= 2t_d \sin k_x \sin k_y. \end{aligned} \qquad (2.14)$$

describes electrons hopping between Ti-orbitals on adjacent sites in the interfacial (xy) plane. d_{xy} orbitals have all the lobes lying on the xy-plane, x- and y- hopping amplitudes are equivalently described by a single *light* matrix elements t_l. Instead d_{xz} and d_{yz} orbitals have both lobes in-plane and in the direction normal to the interface, giving rise to one light and one *heavy* ($t_h < t_l$) matrix element, respectively. Δ_{E} is the gain in the on-site energy of d_{xy} states confined at the interface compared to the on-site energy of d_{xz}/d_{yz} states. Inter-orbital matrix elements $\propto \sin k_x \sin k_y$

account for d_{xz}/d_{yz} hybridization with a strength $t_d \approx t_h$ (however, this term does not affect at all the results of our calculations).

At the interface the confining electric field along the z-direction breaks the inversion-symmetry and activates transitions from d_{xy} orbitals – which are even under mirror symmetry – to d_{xz} and d_{yz} orbitals – odd under mirror symmetry – on adjacent metal sites. The inversion-breaking term has the form

$$H_{\mathrm{Z}} = \Delta_{\mathrm{Z}} \begin{pmatrix} 0 & i\sin k_y & i\sin k_x \\ -i\sin k_y & 0 & 0 \\ -i\sin k_x & 0 & 0 \end{pmatrix} \otimes \hat{\sigma}_0. \qquad (2.15)$$

Atomic spin-orbit coupling is the same as for the bulk STO system, that is

$$H_{\mathrm{SO}} = \frac{\Delta_{\mathrm{SO}}}{2} \sum_{i=x,y,z} \sigma_i \otimes L_i = \frac{\Delta_{\mathrm{SO}}}{2} \begin{pmatrix} 0 & i\hat{\sigma}_x & -i\hat{\sigma}_y \\ -i\hat{\sigma}_x & 0 & i\hat{\sigma}_z \\ i\hat{\sigma}_y & -i\hat{\sigma}_z & 0 \end{pmatrix}, \qquad (2.16)$$

with

$$L_x = \hbar \begin{pmatrix} 0 & i & 0 \\ -i & 0 & 0 \\ 0 & 0 & 0 \end{pmatrix}, \; L_y = \hbar \begin{pmatrix} 0 & 0 & -i \\ 0 & 0 & 0 \\ i & 0 & 0 \end{pmatrix}, \; L_z = \hbar \begin{pmatrix} 0 & 0 & 0 \\ 0 & 0 & i \\ 0 & -i & 0 \end{pmatrix} \qquad (2.17)$$

the representations of the components of the orbital angular momentum. Lastly, the Zeeman Hamiltonian $H_{\mathrm{B}} = \mu_{\mathrm{B}}(\boldsymbol{L} + g\boldsymbol{S}) \cdot \boldsymbol{B}/\hbar$ is

$$H_{\mathrm{B}} = \mu_{\mathrm{B}} \begin{pmatrix} g(\mathrm{B}_x\hat{\sigma}_x+\mathrm{B}_y\hat{\sigma}_y)/2 & i\mathrm{B}_x\hat{\sigma}_0 & -i\mathrm{B}_y\hat{\sigma}_0 \\ -i\mathrm{B}_x\hat{\sigma}_0 & g(\mathrm{B}_x\hat{\sigma}_x+\mathrm{B}_y\hat{\sigma}_y)/2 & 0 \\ i\mathrm{B}_y\hat{\sigma}_0 & 0 & g(\mathrm{B}_x\hat{\sigma}_x+\mathrm{B}_y\hat{\sigma}_y)/2 \end{pmatrix}, \qquad (2.18)$$

with $\mathrm{B}_x = |\boldsymbol{B}|\cos\phi_{\mathrm{B}}$, $\mathrm{B}_y = |\boldsymbol{B}|\sin\phi_{\mathrm{B}}$ and $\boldsymbol{S} = \hbar\hat{\boldsymbol{\sigma}}/2$.

2.7 Appendix B. Dependence of the anisotropy on the parameters of the model

The parameters which define the model of the interface are taken within the ranges that are set by theoretical and experimental results in literature, e.g. first-principles calculations, ARPES measurements on the cleaved surface of strontium titanate [98, 108, 109] and, more recently, soft-X-ray ARPES on the LAO/STO interface [110]. Further estimates from transport measurements [35, 84, 94, 111] give more informations at least about the

order of magnitude of the energy scales in the system. In Table 2.1 we list and discuss the choice of the parameters used for our calculations and in addition we show results for different values of parameters. The comparison with the results in the main text highlight the robustness of the most remarkable features of the data that we have previously highlighted. (The calculations here are for Gaussian-correlated impurities.)

Fig.	t_l	t_h	Δ_E	Δ_{SO}	Δ_Z	g	ξ
2.2, 2.3, 2.7	400	12.5	65	7	2.5	5	5
2.5	400	12.5	65	9	4	-3.4	5
2.6	400	12.5	65	7	2.5	5	4, 8

Table 2.1: Sets of parameters used for the magnetotransport calculations in the chapter, with reference to the figures.

Hopping elements t_l, t_h, confinement energy Δ_E, atomic-spin orbit strength Δ_{SO} and inversion-asymmetry parameter Δ_Z are measured in meV; the g-factor is dimensionless and the disorder correlation-length ξ is measured in units of the lattice constant a. The values of the light and heavy mass corresponding to the hopping parameters t_l and t_h are $0.6\,m_e$ and $19\,m_e$ respectively (m_e is the bare electron mass).

The value of Δ_{SO} from ab-initio calculations [112] or transport experiments [35, 84] is estimated in a wide range $10 \div 25$meV. (In a seminal work on Raman scattering for the bulk STO system Uwe *et al.* [113] extracted the value $18\,$meV). Here we consider the values $\Delta_{SO} = 7\,$meV and $\Delta_{SO} = 9\,$meV (so just below the lower limit of the estimated range) and produce qualitatively similar results for the anisotropy, while at the same time changing also g and Δ_Z. In principle one could take larger values of Δ_{SO} and slightly different hopping elements and still remain in a regime where our results still hold. Moreover, we point out that the strong anisotropy of the spin-orbit field around the Fermi surfaces [98] – with a large enhancement of the effective orbital angular momentum near hybridization gaps – so far has not been considered in fitting transport measurements, that might return overestimated values of Δ_{SO}.

Outcomes of Boltzmann calculations [51] were found in good agreement with the experimentally measured magnetoresistance at $\phi_B = 90°$ (no
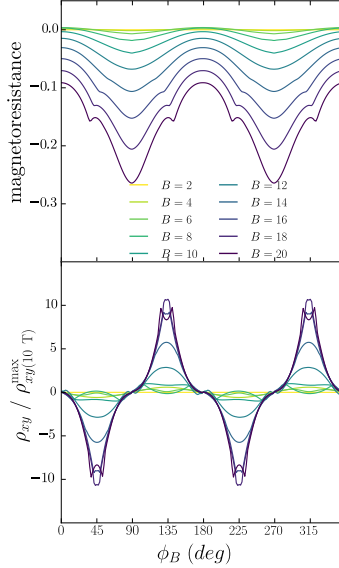
Figure 2.5: Magnetoresistance and transverse resistivity for a negative *g*-factor (parameters from the second row of Table 2.1).

transverse current, hence $\sigma_{xy} = 0$) in the regime of strong inversion-symmetry-breaking $\Delta_{\mathrm{Z}} > \Delta_{\mathrm{SO}}$. Here we obtain similar magnetoresistance – and comparable field–dependence – in the different (and maybe more realistic) regime $\Delta_{\mathrm{Z}} < \Delta_{\mathrm{SO}}$. We can understand this similarity observed in two completely different regimes by realizing that the reversal of the spin-ordering on neighbouring Fermi surfaces induced by the magnetic field, which reduces the overall forward scattering and hence lowers the resistance, occurs in both cases regardless of the relative orientation of orbital and spin angular momenta (which is different in the two regimes). For Δ_{Z} we consider values up to 5 meV, that is the upper bound estimated by Ruhman *et al.* [48].

It is known that the *g*-factor for electrons confined in quantum wells, like InSb and GaAs [114] can substantially differ from the conventional value $g = 2$. In Sec. 2.3 we show results for $g = 5$, one of the two possible outcomes (the other one is $g = -3.4$) of a fit to Shubnikov-de Haas oscillations at low temperature [94]. (Note that changing the *g*-factor is not simply equivalent to rescale the magnetic field: magnetic field also couples to the orbital angular momentum and the relative strength
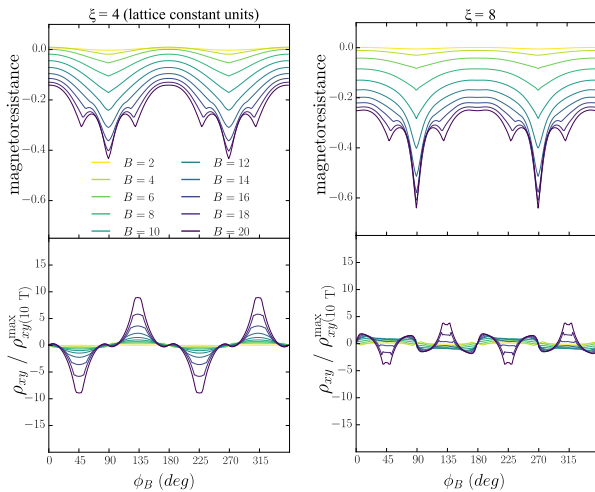
Figure 2.6: Magnetoresistance and transverse resistivity for different values of the correlation-length ξ (parameters from the third row of Table 2.1).

$\langle \boldsymbol{\mu} \cdot \boldsymbol{B} \rangle / \langle \boldsymbol{L} \cdot \boldsymbol{B} \rangle$ is dependent on g.) Yet the phenomenology of the anisotropy which we extensively discussed in Sec. 2.4 is recovered at negative $g = -3.4$ (Fig. 2.5).

Variations in the correlation-length ξ are also considered. While there is no simple way to extract informations from experiments, it is reasonable to limit ξ within a range of one order of magnitude. Indeed, a too large ξ (> 10 a_0 with $a_0 = 0.4$nm the lattice constant) would require to treat the impurities as a disordered medium rather than independent scatterers. Calculations in the main text refer to $\xi = 5\,a_0$. In Fig. 2.6, results for $\xi = 4, 6, 8$ are shown. Qualitatively the results are very similar if $\xi|\Delta\boldsymbol{k}^{bs}| > 1$ where $|\Delta\boldsymbol{k}^{bs}| \sim 2k_F^{out}$ is the momentum-transfer for backscattering in the large outer band (approximately equal to twice the average Fermi momentum) and at the same time not larger than $10 - 15$ a_0 – with $a_0 = 0.4$nm the lattice constant – whereby also the zero-field inter-band scattering is highly reduced. This upper limit is also consistent with the assumption of scattering by individual impurities (rather than by a disordered medium that is a more suitable description for very large ξ).

Finally, we shortly comment on the density– vs. field–dependence of the resistivities. Universal scaling of the magnetoresistance curves as a function of carrier-density, after the magnetic field is rescaled by a density–dependent characteristic value, appears to be a general feature of the experimental data [50, 51]. This is not recovered by the Boltzmann
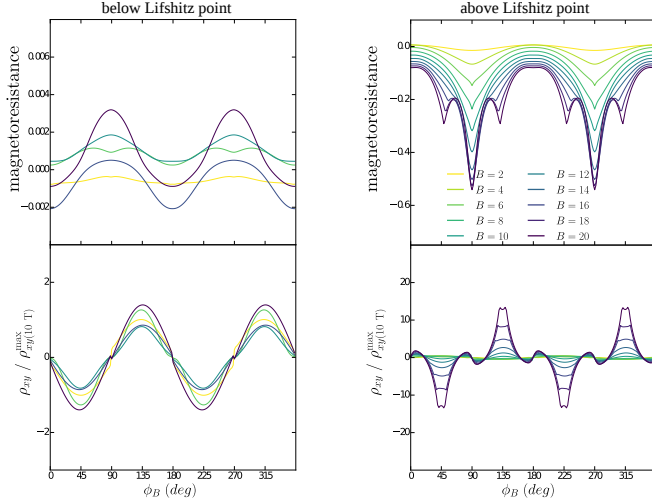
Figure 2.7: Magnetoresistance and transverse resistivity for two different densities (both lower than the density considered in the main text). There is a clear difference in pattern and the magnitude of the anisotropy between the two cases.

model (even within this different spin-orbit regime) pointing to a physical mechanism that might be unrelated to spin-orbit coupling.

In Fig. 2.7 we show results of calculations at two different densities, $n = 1.5 \cdot 10^{13}$cm^{-2} (below the Lifshitz point) and $n = 2.1 \cdot 10^{13}$cm^{-2} (above the Lifshitz point). The total absence of magnetoresistance at the lowest density (left panel) simply comes from the absence of inter-band scattering (since only the lowest d_{xy} states are filled). At higher density (right panel) the large-field magnetoresistance is characterized by multiple maxima and minima as in Fig. 2.2, but there is larger discrepancy between the magnetoresistance calculated at $\phi_B = 0$ and the one at $\phi_B = 90$. This gap is progressively reduced as the chemical potential tends to the middle of the spin-orbit gap at the Γ-point.

3 Chirality blockade of Andreev reflection in a magnetic Weyl semimetal

3.1 Introduction

Spin-momentum locking is a key feature of topological states of matter: In both topological insulators and topological semimetals the massless quasiparticles are governed by a Hamiltonian $H_{\pm} = \pm v_{\mathrm{F}} \boldsymbol{p} \cdot \boldsymbol{\sigma}$ that ties the direction of motion to the spin polarization.[3, 14, 115, 116] In a topological insulator the $\pm$ sign distinguishes spatially separated states, e.g., the opposite edges of a quantum spin-Hall insulator along which a spin-up electron moves in opposite directions.[117] In a topological semimetal the $\pm$ sign distinguishes Weyl cones in the band structure. A magnetic Weyl semimetal has the minimum number of two Weyl cones centered at opposite points $\pm \boldsymbol{K}$ in the Brillouin zone, containing left-handed and right-handed Weyl fermions displaced in the direction of the magnetization.[63]

It is the purpose of the work presented in this chapter to point out that the switch in chirality between the Weyl cones forms an obstacle to Andreev reflection from a superconductor with conventional, spin-singlet s-wave pairing, when the magnetization lies in the plane of the normal-superconductor (NS) interface. The obstruction is illustrated in Fig. 3.1. Andreev reflection is the backscattering of an electron as a hole, accompanied by the transfer of a Cooper pair to the superconductor. For a given spin band and a given Weyl cone, electrons and holes move in the same direction, [1] so backscattering must involve either a switch in spin band ($\boldsymbol{\sigma} \mapsto -\boldsymbol{\sigma}$) or a switch in Weyl cone ($\boldsymbol{K} \mapsto -\boldsymbol{K}$), but not both. This is at odds with the requirement that zero spin and zero momentum is transferred to the Cooper pair.

---

[1] A quick way to see that electrons and holes in a given spin band and Weyl cone move in the same direction, is to note that their dispersion relations are related by $E_{\mathrm{electron}}(k) = -E_{\mathrm{hole}}(-k)$, so a linear dispersion $E = v_{\mathrm{F}} k$ remains the same.
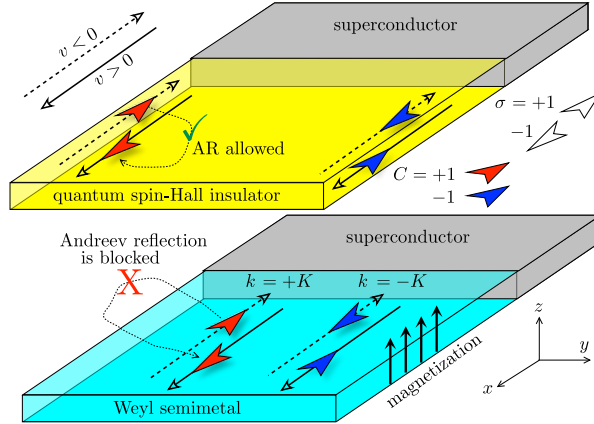
Figure 3.1: Andreev reflection (AR) from a superconductor in a quantum spin-Hall insulator (top panel) and in a Weyl semimetal (bottom panel.) The red and blue wedges designate electron and hole quasiparticles (Weyl fermions) moving towards or away from the interface (solid versus dashed arrows indicate v in the $\pm x$ direction). The orientation of the wedge distinguishes the polarization $\sigma = \pm 1$ of the spin band and the color indicates the chirality $C = \text{sign}\,(v\sigma)$. Andreev reflection switches σ and v, which is blocked if it must also switch C.

This "chirality blockade" of Andreev reflection is specific for the conical dispersion in a Weyl semimetal, and it does not appear in other contexts where spin-momentum locking plays a role. In a quantum spin-Hall insulator, there is no need to switch the chirality because the hole can be reflected along the same edge as the incident electron.[118] There is a formal similarity with graphene,[119] where Andreev reflection switches between valleys at $\pm\boldsymbol{K}$, but there $\boldsymbol{\sigma}$ is an orbital pseudospin and the real spin is not tied to the direction of motion.

We will show that the chirality blockade can be lifted by breaking the requirement of zero-spin transfer with a Zeeman field. We also discuss the subtle role played by inversion symmetry, by contrasting a *scalar* with a *pseudoscalar* pair potential.[120] The absence of the chirality blockade for pseudoscalar pairing explains why it did not appear in the many previous studies of Andreev reflection in a Weyl semimetal.[121–129]

The outline of this chapter is as follows. In the next section, we introduce the model of an NS junction between a Weyl semimetal and a conventional superconductor. The 8×8 Bogoliubov-De Gennes Hamiltonian is block-diagonalized in Sec. 3.3, after which the chirality blockade of Andreev reflection is obtained in Sec. 3.4. In the next section 3.5, we show how to remove the blockade by a spin-active interface or by an inversion-

symmetry breaking interface. As an experimental signature, we calculate the conductance of the NS junction in Sec. 3.6. To eliminate the effects of a lattice mismatch, we consider in Sec. 3.7 the NS junction between a Weyl semimetal and a Weyl superconductor — which shows the same chirality blockade for a scalar spin-singlet pair potential. More general pairing symmetries (spin-triplet and pseudoscalar spin-singlet) are considered in an Appendix. The Josephson effect in an SNS junction is studied in Sec. 3.8. We conclude in Sec. 3.9.

3.2 Model of a Weyl semimetal – conventional superconductor junction

We study the junction between a Weyl semimetal in the normal state (N) and a conventional (spin-singlet, *s*-wave) superconductor (S), by first considering separately the Hamiltonians in the two regions and then modeling the interface.

Throughout the chapter, we take the configuration of Fig. 3.1 (bottom panel), with the magnetization along z in the plane of the NS interface at $x = 0$. An out-of-plane rotation of the magnetization by an angle α does not change the results for isotropic Weyl cones, provided that the Fermi surfaces of opposite chirality are not coupled upon reflection at the interface. The geometric condition for this is $\cos\alpha \geq k_{\mathrm{F}}/K$, with k_{F} the Fermi wave vector and $(0, 0, \pm K)$ the location of the two Weyl points. We assume $k_{\mathrm{F}}/K \ll 1$ in order to have well-resolved Weyl cones, and then there is a broad range of magnetization angles α over which our analysis applies.

3.2.1 Weyl semimetal region

The Weyl semimetal in the region $x > 0$ has the generic Hamiltonian[130–132]

$$H_{\mathrm{W}}(\boldsymbol{k}) = \tau_z(\sigma_x t_x \sin k_x + \sigma_y t_y \sin k_y + \sigma_z t_z \sin k_z)$$
$$+ m_{\boldsymbol{k}}\tau_x\sigma_0 + \beta\tau_0\sigma_z - \mu_{\mathrm{W}}\tau_0\sigma_0, \tag{3.1a}$$
$$m_{\boldsymbol{k}} = m_0 + t'_x(1 - \cos k_x) + t'_y(1 - \cos k_y) + t'_z(1 - \cos k_z). \tag{3.1b}$$

The units are normalized by $\hbar \equiv 1$ and lattice constant $a_0 \equiv 1$. The Pauli matrices τ_α and σ_α refer to orbital and spin degrees of freedom (with τ_0,

σ_0 the 2×2 unit matrix). The Weyl points are at $\boldsymbol{k} = (0, 0, \pm K)$, with

$$K^2 \approx \frac{\beta^2 - m_0^2}{t_z^2 + t_z' m_0} \tag{3.2}$$

displaced by the magnetization β in the z-direction. The mass term $m_{\boldsymbol{k}}$ ensures that there are no other states near the Fermi energy, so that we have the minimal number of two Weyl cones of opposite chirality.

While time-reversal symmetry is broken by the magnetization β, the inversion symmetry of the material is preserved:

$$\tau_x H_{\mathrm{W}}(-\boldsymbol{k})\tau_x = H_{\mathrm{W}}(\boldsymbol{k}). \tag{3.3}$$

The presence of inversion symmetry plays a crucial role when superconductivity enters, because the pair potential couples electrons and holes at opposite momentum.

To describe the superconducting proximity effect we add the electron-hole degree of freedom ν, with electron and hole Hamiltonians related by the operation of time-reversal:

$$H_{\mathrm{W}}^{(e)}(\boldsymbol{k}) = H_{\mathrm{W}}(\boldsymbol{k}), \quad H_{\mathrm{W}}^{(h)}(\boldsymbol{k}) = \sigma_y H_{\mathrm{W}}^*(-\boldsymbol{k})\sigma_y. \tag{3.4}$$

The two Hamiltonians are incorporated in the Bogoliubov-De Gennes (BdG) Hamiltonian

$$\begin{aligned}
\mathcal{H}_{\mathrm{W}} &= \begin{pmatrix} H_{\mathrm{W}}^{(e)} & 0 \\ 0 & -H_{\mathrm{W}}^{(h)} \end{pmatrix} \\
&= \nu_z \tau_z (\sigma_x t_x \sin k_x + \sigma_y t_y \sin k_y + \sigma_z t_z \sin k_z) \\
&\quad + m_{\boldsymbol{k}} \nu_z \tau_x \sigma_0 + \beta \nu_0 \tau_0 \sigma_z - \mu_{\mathrm{W}} \nu_z \tau_0 \sigma_0.
\end{aligned} \tag{3.5}$$

Electron-hole symmetry is expressed by

$$\nu_y \sigma_y \mathcal{H}_{\mathrm{W}}^*(-\boldsymbol{k})\nu_y \sigma_y = -\mathcal{H}_{\mathrm{W}}(\boldsymbol{k}). \tag{3.6}$$

Note that the electron-hole symmetry operation squares to $+1$, as it should in symmetry class D (fermions without spin-rotation or time-reversal symmetry).

3.2.2 Superconducting region

The region $x < 0$ contains a conventional spin-singlet s-wave superconductor (real pair potential Δ_0), with BdG Hamiltonian

$$\mathcal{H}_{\mathrm{S}} = \begin{pmatrix} p^2/2m - \mu_{\mathrm{S}} & \Delta_0 \\ \Delta_0 & -p^2/2m + \mu_{\mathrm{S}} \end{pmatrix}. \tag{3.7}$$

For a chemical potential $\mu_S \gg \mu_W$, the momentum components p_y, p_z parallel to the NS interface at $x = 0$ can be neglected relative to the perpendicular component p_x. We expand $p_x = \pm p_F + k_x$ around the Fermi momentum $p_F = mv_F$ (with $\mu_S = p_F^2/2m$), by carrying out the unitary transformation

$$
\begin{aligned}
\mathcal{H}_S &\mapsto e^{-i\tau_z p_F x} \mathcal{H}_S e^{i\tau_z p_F x} \\
&= v_F k_x \nu_z \tau_z \sigma_0 + \Delta_0 \nu_x \tau_0 \sigma_0 + \mathcal{O}(k_x^2).
\end{aligned} \tag{3.8}
$$

Left-movers and right-movers in the x-direction are distinguished by the τ degree of freedom, and we have inserted a σ_0 Pauli matrix to account for the spin degeneracy in S.

Electron-hole symmetry in S is expressed by

$$
\nu_y \tau_x \sigma_y \mathcal{H}_S^*(-k_x) \nu_y \tau_x \sigma_y = -\mathcal{H}_S(k_x). \tag{3.9}
$$

There is an additional τ_x Pauli matrix, in comparison with the corresponding symmetry relation (3.6) in N, to account for the switch from $+p_F$ to $-p_F$. (The electron-hole symmetry operation still squares to $+1$.)

3.2.3 Interface transfer matrix

The wave functions ψ_W and ψ_S on the two sides of the NS interface at $x = 0$ are related by a transfer matrix,

$$
\psi_S = (t_x/v_F)^{1/2} \mathcal{M} \psi_W, \quad \mathcal{M} = \begin{pmatrix} M_e & 0 \\ 0 & M_h \end{pmatrix}, \tag{3.10}
$$

which ensures that particle current is conserved across the interface. We assume that the interface does not couple electrons and holes, [2] hence the block-diagonal structure, and we also assume that $\mathcal{M}$ is independent of energy. The symmetry relations (3.6) and (3.9) imply that the electron and hole transfer matrices are related by

$$
M_h = \tau_x \sigma_y M_e^* \tau_0 \sigma_y. \tag{3.11}
$$

Particle current conservation is expressed by

$$
\langle \psi_S | v_F \nu_z \tau_z \sigma_0 | \psi_S \rangle = \langle \psi_W | t_x \nu_z \tau_z \sigma_x | \psi_W \rangle, \tag{3.12}
$$

---

[2]It is justified to ignore electron-hole coupling in the interface matrix (3.10), because this describes the transmission through a length of order $1/k_F$ in S, which is smaller than the electron-hole coupling length v_F/Δ_0 by a factor $E_F/\Delta_0 \gg 1$.

where we have also linearized H_W in k_x. The resulting restriction on the electron transfer matrix is

$$M_e^\dagger \tau_z \sigma_0 M_e = \tau_z \sigma_x. \tag{3.13}$$

Eq. (3.11) then implies that the hole transfer matrix M_h satisfies the same restriction.

It is helpful to factor out the unitary matrix Ξ_0,

$$M_e \equiv \Xi\Xi_0, \;\; \Xi_0 = \exp\left[i\frac{\pi}{4}\tau_x(\sigma_0 - \sigma_x)\right], \tag{3.14}$$

with $\Xi_0\tau_z\Xi_0^\dagger\tau_z = \Xi_0^2 = \sigma_x$, because now instead of Eq. (3.13) we have a quasi-unitarity restriction

$$\Xi^{-1} = \tau_z\Xi^\dagger\tau_z \tag{3.15}$$

that is satisfied by the unit matrix.

The corresponding factorization of the hole transfer matrix is

$$M_h = \tau_x\sigma_y(\Xi\Xi_0)^*\tau_0\sigma_y, \tag{3.16}$$

as required by the electron-hole symmetry (3.11). For later use we give the inverse

$$M_h^{-1} = (\sigma_y\Xi_0\sigma_y)(\tau_z\sigma_y\Xi^\mathrm{T}\tau_z\sigma_y)\tau_x, \tag{3.17}$$

in view of the quasi-unitarity (3.15). (The superscript T denotes the transpose of a matrix.)

As an aside, we note that if the interface preserves time-reversal symmetry, we have the additional restriction

$$\Xi = \tau_x\sigma_y\Xi^*\tau_x\sigma_y. \tag{3.18}$$

Inversion symmetry is expressed by

$$\Xi = \tau_x\Xi^{-1}\tau_x. \tag{3.19}$$

3.3 Block-diagonalization of the Weyl Hamiltonian

For the mode-matching calculations at the NS interface it is convenient to block-diagonalize $\mathcal{H}_\mathrm{W}$ in the τ degree of freedom, by means of the unitary

transformation[61]

$$\tilde{\mathcal{H}}_{\mathrm{W}} = \mathcal{U}\mathcal{H}_{\mathrm{W}}\mathcal{U}^{\dagger}, \ \ \mathcal{U} = \begin{pmatrix} i\tau_y\sigma_z\Omega_\theta & 0 \\ 0 & \Omega_\theta \end{pmatrix},$$
$$\Omega_\theta = \exp(-\tfrac{1}{2}i\theta\tau_y\sigma_z), \tag{3.20}$$

with a $\boldsymbol{k}$-dependent angle $\theta \in (0,\pi)$ defined by

$$\cos\theta = -\frac{t_z\sin k_z}{M_{\boldsymbol{k}}}, \ \ \sin\theta = \frac{m_{\boldsymbol{k}}}{M_{\boldsymbol{k}}},$$
$$M_{\boldsymbol{k}} = \sqrt{m_{\boldsymbol{k}}^2 + t_z^2\sin^2 k_z}. \tag{3.21}$$

Note that $\mathcal{U}$ satisfies

$$\mathcal{U}(\boldsymbol{k}) = \nu_y\sigma_y\mathcal{U}^*(-\boldsymbol{k})\nu_y\sigma_y, \tag{3.22}$$

because $\boldsymbol{k} \mapsto -\boldsymbol{k}$ maps $\theta \mapsto \pi - \theta$, so the electron-hole symmetry relation (3.6) for $\mathcal{H}_{\mathrm{W}}$ is preserved upon the unitary transformation.

The transformed Hamiltonian,

$$\tilde{\mathcal{H}}_{\mathrm{W}}(\boldsymbol{k}) = \nu_z\tau_z(\sigma_x t_x\sin k_x + \sigma_y t_y\sin k_y) + M_{\boldsymbol{k}}\nu_0\tau_z\sigma_z$$
$$+ \beta\nu_0\tau_0\sigma_z - \mu_{\mathrm{W}}\nu_z\tau_0\sigma_0, \tag{3.23}$$

is block-diagonal in τ. The Weyl cones are in the $\tau = -1$ block, which has low-energy states near $\boldsymbol{k} = (0, 0, \pm\beta/t_z)$ when $M_{\boldsymbol{k}} \approx \beta$. The $\tau = +1$ block is pushed to higher energies of order 2β.

The unitary transformation changes the wave function in N as $\tilde{\psi}_{\mathrm{W}} = \mathcal{U}\psi_{\mathrm{W}}$, and hence the matching equation (3.10) becomes

$$\psi_{\mathrm{S}} = (t_x/v_{\mathrm{F}})^{1/2}\mathcal{M}\mathcal{U}^{\dagger}\tilde{\psi}_{\mathrm{W}}. \tag{3.24}$$

3.4 Andreev reflection

At excitation energies E below the superconducting gap Δ_0, an electron incident on the superconductor from the Weyl semimetal is reflected, either as an electron (normal reflection, with amplitude r_{ee}) or as a hole (Andreev reflection, with amplitude r_{he}). We calculate these reflection amplitudes, initially restricting ourselves to normal incidence on the NS interface, in order to simplify the formulas. The angular dependence is included in Sec. 3.6, when we calculate the conductance.

We include the energy dependence of the reflection amplitudes, but since we assume only the low-energy states in the $\tau = -1$ block are propagating our analysis is restricted to $|E| \lesssim \beta$. Typically $\beta \simeq 100\,\mathrm{meV}$ is much larger than $\Delta_0 \simeq 0.1\,\mathrm{meV}$, so this covers the relevant energy range.

3.4.1 Effective boundary condition at the NS interface

As in the analogous problem for graphene,[133] the effect of the superconducting region $x < 0$ on the Weyl semimetal region $x > 0$ can be described by an effective boundary condition on the wave functions in the limit $x \to 0$ from above, indicated as $x = 0^+$.

According to the Hamiltonian (3.8), the propagation of the wave function into the superconductor at energy E is governed by the differential equation

$$v_{\mathrm{F}} \frac{\partial}{\partial x} \psi(x) = \left(iE\nu_z + \Delta_0 \nu_y\right)\tau_z\sigma_0\psi(x) \equiv X_{\mathrm{S}}\psi(x). \qquad (3.25)$$

The eigenvalues of X_{S} are $\pm\sqrt{\Delta_0^2 - E^2}$. To ensure a decaying wave function in the S region $x < 0$ for $|E| < \Delta_0$, the state ψ_{S} at $x = 0^-$ should be a linear superposition of the four eigenvectors with positive eigenvalue. This is expressed by the boundary condition

$$\begin{aligned} \nu_x\psi_{\mathrm{S}} &= \exp(i\alpha\nu_z\tau_z\sigma_0)\psi_{\mathrm{S}}, \\ \alpha &= \arccos(E/\Delta_0) \in (0, \pi/2). \end{aligned} \qquad (3.26)$$

If we decompose $\psi_{\mathrm{S}} = (\psi_e, \psi_h)$ into electron and hole components, the boundary condition can be written as

$$\psi_h(0^-) = \exp(i\alpha\tau_z)\psi_e(0^-). \qquad (3.27)$$

This is a special case of the more general relation between electron and hole wave functions at an NS interface derived in App. 3.10.

The combination of Eqs. (3.24) and (3.27) gives on the Weyl semimetal side of the NS interface the relation

$$\begin{aligned} \tilde{\psi}_h(0^+) &= \mathcal{T}\tilde{\psi}_e(0^+), \\ \mathcal{T} &= -i\Omega_\theta M_h^{-1} \exp(i\alpha\tau_z)M_e\Omega_\theta^\dagger\tau_y\sigma_z, \end{aligned} \qquad (3.28)$$

which can be worked out as

$$\begin{aligned} \mathcal{T} &= -i\Omega_\theta(\sigma_y\Xi_0\sigma_y)(\tau_z\sigma_y\Xi^{\mathrm{T}}\tau_z\sigma_y)\tau_x \exp(i\alpha\tau_z)\Xi(\Xi_0\Omega_\theta^\dagger\tau_y\sigma_z) \\ &= U_\theta^\dagger\tau_x\sigma_x\Xi^{\mathrm{T}}\tau_y\sigma_y \exp(i\alpha\tau_z)\Xi U_\theta, \qquad &(3.29a) \\ U_\theta &\equiv \Xi_0\Omega_\theta^\dagger\tau_y\sigma_z, \qquad &(3.29b) \end{aligned}$$

upon substitution of Eq. (3.17) and using $\tau_y\sigma_z(\sigma_y\Xi_0\sigma_y)\tau_y\sigma_z = \Xi_0^\dagger$.

3.4.2 Reflection amplitudes

We consider an incident mode $\psi_{\text{incident}} = (\psi_{e,\text{inc}}, \psi_{h,\text{inc}})$ without a hole component, $\psi_{h,\text{inc}} = 0$, and initially take the simplest case of normal incidence, when $k_y = 0$ and $k_z = \pm K$ is at one of the two Weyl points. (The dependence on the angle of incidence is included later on.) We work in the transformed basis from Section 3.3, when both Weyl points are in the $\tau_z = -1$ band.

The incident electron wave function $\tilde{\psi}_{e,\text{inc}} = (0,0,1,1)$ has $\sigma_x = +1$ in the $\tau_z = -1$ band, so that its velocity $t_x \nu_z \tau_z \sigma_x$ is in the negative x-direction. The reflected wave function $\tilde{\psi}_{\text{reflected}} = (\tilde{\psi}_{e,\text{refl}}, \tilde{\psi}_{h,\text{refl}})$ contains an electron component $\tilde{\psi}_{e,\text{refl}} = r_{ee}(0,0,1,-1)$ with $\sigma_x = -1$, and a hole component $\tilde{\psi}_{h,\text{refl}} = r_{he}(0,0,1,1)$ with $\sigma_x = +1$, both waves propagating in the positive x-direction. The reflected waves are related to the incident wave by the normal reflection amplitude r_{ee} and the Andreev reflection amplitude r_{he}.

At the interface the propagating modes in the $\tau_z = -1$ band may excite evanescent modes in the $\tau_z = +1$ band. Their wave function $\tilde{\psi}_{\text{evan}}$ in N is an eigenstate of $\nu_z \sigma_y$ with eigenvalue $+1$, so that the Hamiltonian (3.23) produces a decay for $x \to \infty$. The electron and hole components of the evanescent mode are $\tilde{\psi}_{e,\text{evan}} = a(1, i, 0, 0)$ and $\tilde{\psi}_{h,\text{surf}} = b(1, -i, 0, 0)$, with unknown amplitudes a, b.

The boundary condition (3.28) then equates the vectors

$$\begin{pmatrix} b \\ -ib \\ r_{he} \\ r_{he} \end{pmatrix} = \mathcal{T} \begin{pmatrix} a \\ ia \\ 1 + r_{ee} \\ 1 - r_{ee} \end{pmatrix}. \tag{3.30}$$

There is no dependence on the chemical potential μ_W in the Weyl semimetal for normal incidence.

For an inactive interface, with $\Xi = 1$, we have

$$\mathcal{T} = \tau_y \sigma_z \cos\alpha - i\tau_x \sigma_y \sin\alpha, \tag{3.31}$$

and we find

$$r_{ee} = -ie^{-2i\alpha}, \quad r_{he} = 0, \tag{3.32}$$

i.e. fully suppressed Andreev reflection at all energies (and also at all angles of incidence, see Sec. 3.6). For $E < \Delta_0$ the incident electron is reflected as an electron with unit probability, without any transfer of a Cooper pair into the superconductor. For $E > \Delta_0$ the angle $\alpha = -i \operatorname{arcosh}(E/\Delta_0)$ is imaginary and the incident electron is partly transmitted through the NS interface — but still without any Cooper pair transfer.

3.5 Activation of Andreev reflection

Andreev reflection can be restored by a suitably chosen interface potential. We examine two types of interfaces, one that breaks time-reversal symmetry by a Zeeman coupling to the spin, and another that breaks inversion symmetry by a tunnel coupling to the orbital degree of freedom.

3.5.1 Spin-active interface

We consider an interface with a Zeeman Hamiltonian $H_{\text{interf}} = g\mu_{\text{B}}\boldsymbol{B} \cdot \boldsymbol{\sigma}$ on the S side, which gives a transfer matrix

$$\Xi = \exp\bigl[i(\ell/v_{\text{F}})\tau_z H_{\text{interf}}\bigr] = \exp\bigl[i\gamma\tau_z(\boldsymbol{n} \cdot \boldsymbol{\sigma})\bigr], \qquad (3.33)$$

with $\gamma = g\mu_{\text{B}}B\ell/v_{\text{F}}$, $\boldsymbol{n}$ a unit vector in the $\boldsymbol{B}$-direction, and ℓ is the thickness of the interface layer. The superconducting coherence length $\xi = \hbar v_{\text{F}}/\Delta_0$ is an upper bound on ℓ, and hence $\gamma \lesssim E_{\text{Zeeman}}/\Delta_0$, with $E_{\text{Zeeman}} = g\mu_{\text{B}}B$ the Zeeman spin splitting.

Depending on the direction of the field, we find the Andreev reflection amplitudes

$$H_{\text{interf}} = B_x\sigma_x \Rightarrow r_{he} = -\frac{2\cos\alpha \sin 2\gamma \sin\theta}{\sin^2 2\gamma \sin^2\theta + e^{2i\alpha}}, \qquad (3.34\text{a})$$

$$H_{\text{interf}} = B_y\sigma_y \Rightarrow r_{he} = \frac{2i\sin\alpha \sin 2\gamma \cos\theta}{\sin^2 2\gamma \cos^2\theta - e^{2i\alpha}}, \qquad (3.34\text{b})$$

$$H_{\text{interf}} = B_z\sigma_z \Rightarrow r_{he} = -\frac{2i\cos\alpha \sin 2\gamma}{\sin^2 2\gamma + e^{2i\alpha}}. \qquad (3.34\text{c})$$

At the Fermi level ($E = 0 \Rightarrow \alpha = \pi/2$), we have $r_{he} = 0$ for $\boldsymbol{B}$ in the x-direction or in the z-direction, while a field in y-direction activates the Andreev reflection.

For $m_0 \ll \beta \ll t_z$ we may approximate $K \approx \beta/t_z \ll 1$, $\sin\theta \approx \beta/2t_z \ll 1$ and $\cos\theta \approx \mp 1$. The Andreev reflection probability $R_{he} = |r_{he}|^2$ at the Fermi level for $\boldsymbol{B}$ in the y-direction is then given by

$$R_{he} = \frac{4\sin^2 2\gamma}{(1 + \sin^2 2\gamma)^2}. \qquad (3.35)$$

It oscillates with γ, reaching a maximum of unity when $\gamma = \frac{1}{4}\pi$ modulo $\pi/2$.

3.5.2 Inversion-symmetry breaking interface

We next consider interfaces that break inversion symmetry rather than time-reversal symmetry. A potential barrier on the S side of the interface couples $\pm k_{\mathrm{F}}$, and thereby switches the τ_z index. This is modeled by a tunnel Hamiltonian of the form $H_{\mathrm{interf}} = V_{\mathrm{barrier}}\tau_\alpha$ with $\alpha \in \{x, y\}$, which preserves time-reversal symmetry ($H_{\mathrm{interf}} = \tau_x \sigma_y H_{\mathrm{interf}}^* \tau_x \sigma_y$).

The choice $H_{\mathrm{interf}} = V_{\mathrm{barrier}}\tau_x$ gives the transfer matrix

$$\Xi = e^{-\gamma'\tau_y}, \ \ \gamma' = V_{\mathrm{barrier}}\ell/v_{\mathrm{F}} \lesssim V_{\mathrm{barrier}}/\Delta_0. \tag{3.36}$$

This preserves inversion symmetry [see Eq. (3.19)], and does not activate Andreev reflection: $r_{he} = 0$ for all E.

If instead we take the Hamiltonian $H_{\mathrm{interf}} = V_{\mathrm{barrier}}\tau_y$, we have $\Xi = e^{\gamma'\tau_x}$. Inversion symmetry is broken, and we find activated Andreev reflection:

$$r_{he} = \frac{2i \sin \alpha \sinh 2\gamma' \cos \theta}{\sin^2 \alpha \sinh^2 2\gamma' \sin^2 \theta + (\sin \alpha \cosh 2\gamma' - i \cos \alpha)^2}. \tag{3.37}$$

At the Fermi level, and for $m_0 \ll \beta \ll t_z$, the Andreev reflection probability is

$$R_{he} = \frac{4 \sinh^2 2\gamma'}{\cosh^4 2\gamma'}. \tag{3.38}$$

It reaches a maximum of unity for $\gamma' = \frac{1}{2}\ln(1 + \sqrt{2}) = 0.441$, decaying to zero for both smaller and larger γ'.

3.6 Conductance of the NS junction

The reflection probabilities $R_{ee} = |r_{ee}|^2$ and $R_{he} = |r_{he}|^2$ determine the differential conductance $dI/dV = G(eV)$ of the NS junction, per unit surface area, according to[134]

$$G(E) = \frac{e^2}{h} \int \frac{dk_y}{2\pi} \int \frac{dk_z}{2\pi}(1 - R_{ee} + R_{he}). \tag{3.39}$$

The reflection amplitudes r_{ee} and r_{he}, as a function of energy E and transverse momentum components k_y, k_z, follow from the solution of Eq. (3.30), suitably generalized to include an arbitrary angle of incidence.

We consider an incident electron near the Weyl point at $\boldsymbol{k} = (0, 0, K)$, with $K \approx \beta/t_z \ll 1$. [The other Weyl cone at $-K$ gives the same contribution to the conductance and we may set $\theta = 0$ in the transfer

matrix (3.29).] We take $\mu_W, E > 0$ so the electron is above the Fermi level at energy $\mu_W + E$ in the upper half of the Weyl cone. The Andreev reflected hole is below the Fermi level at energy $\mu_W - E$, which drops into the lower half of the Weyl cone when $E > \mu_W$. For brevity we denote $q_x = t_x k_x$, $q_y = t_y k_y$, $q_z = t_z k_z - \beta$.

We normalize the conductance by the total number $N(E)$ of propagating electron modes in the Weyl cones at energy E above μ_W, given by

$$
\begin{aligned}
N(E) &= 2 \int \frac{dq_y}{2\pi t_y} \int \frac{dq_z}{2\pi t_z} \, \Theta \left[(E + \mu_W)^2 - q_y^2 - q_z^2 \right] \\
&= \frac{(E + \mu_W)^2}{2\pi t_y t_z}.
\end{aligned} \tag{3.40}
$$

(The prefactor 2 sums the contributions from the two Weyl cones.)

The low-energy Hamiltonian H_K follows upon projection of the Hamiltonian (3.23) on the $\tau = -1$ band and expansion around the Weyl point,

$$
H_K = -\nu_z(\sigma_x q_x + \sigma_y q_y) - \nu_0 \sigma_z q_z - \mu_W \nu_z \sigma_0. \tag{3.41}
$$

The x-component of the momentum is $-q_x$ and $+q_x$ for the incident and reflected electron, and q_x' for the hole, with

$$
\begin{aligned}
q_x &= \sqrt{(E + \mu_W)^2 - q_y^2 - q_z^2}, \\
q_x' &= \text{sign} \, (E - \mu_W) \sqrt{(E - \mu_W)^2 - q_y^2 - q_z^2}.
\end{aligned} \tag{3.42}
$$

Only real q_x contribute to the wave vector integration in Eq. (3.39), and when q_x' becomes imaginary one should set $R_{he} \equiv 0$.

Substitution of the corresponding spinors into Eq. (3.30) (normalized to unit flux) gives the mode matching condition

$$
\sqrt{\frac{q_x(E + \mu_W - q_z)}{q_x'(E - \mu_W - q_z)}} \begin{pmatrix} b \\ -ib \\ (q_x' + iq_y)r_{he} \\ (E - \mu_W - q_z)r_{he} \end{pmatrix} =
$$

$$
= \mathcal{T} \begin{pmatrix} a \\ ia \\ q_x - iq_y + (q_x + iq_y)r_{ee} \\ (E + \mu_W - q_z)(1 - r_{ee}) \end{pmatrix}. \tag{3.43}
$$

For the inactive interface, when $\Xi = 1$, the Andreev reflection amplitude vanishes at all energies for all angles of incidence. Andreev reflection
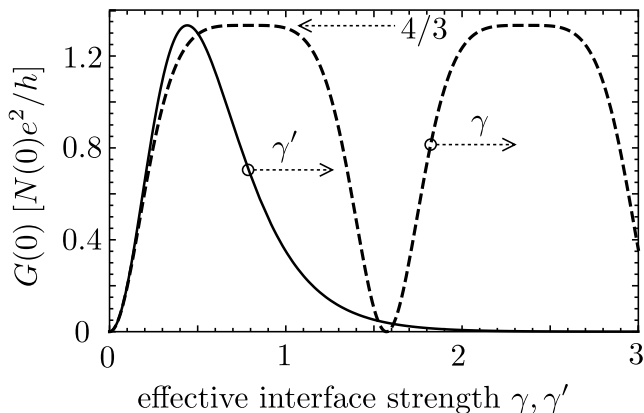
Figure 3.2: Zero-bias conductance of the NS junction, calculated from Eq. (3.44), for the spin-active interface (dashed curve) and for the inversion-symmetry breaking interface (solid curve). The conductance is normalized by the number of modes N from Eq. (3.40). For the inactive interface the conductance vanishes.

is activated by the spin-active interface or by the inversion-symmetry-breaking interface, as discussed in Sec. 3.5. At the Fermi level ($E = 0$, $q'_x = -q_x$) we recover the results (3.35) and (3.38) multiplied by the factor $q_x^2/(q_x^2 + q_z^2)$ that accounts for the deviation from normal incidence. The resulting zero-bias conductance is given by

$$\lim_{V \to 0} \frac{dI}{dV} = \tfrac{16}{3} N(0) \frac{e^2}{h} \times \begin{cases} \sin^2 2\gamma/(1 + \sin^2 2\gamma)^2, \\ \sinh^2 2\gamma'/\cosh^4 2\gamma', \end{cases} \tag{3.44}$$

as plotted in Fig. 3.2, with $\gamma = E_{\text{Zeeman}}\ell/v_{\text{F}} \lesssim E_{\text{Zeeman}}/\Delta_0$ in the spin-active interface Hamiltonian $H_{\text{interf}} = E_{\text{Zeeman}}\sigma_y$, and $\gamma' = V_{\text{barrier}}\ell/v_{\text{F}} \lesssim V_{\text{barrier}}/\Delta_0$ in the inversion-symmetry breaking case $H_{\text{interf}} = V_{\text{barrier}}\tau_y$.

The voltage-dependent differential conductance is plotted in Fig. 4.10. The conductance vanishes at $eV = \mu_{\text{W}} < \Delta_0$, when the hole touches the Weyl point. (The same feature appears at the Dirac point in graphene [135].)

3.7 Weyl semimetal – Weyl superconductor junction

So far we have considered the junction between a Weyl semimetal and a superconductor formed from a conventional metal. A doped Weyl semimetal
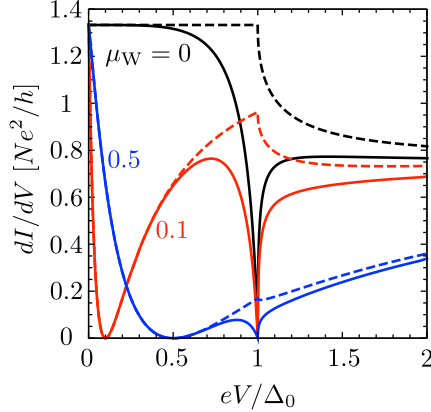
Figure 3.3: Differential conductance of the NS junction, calculated from Eqs. (3.39) and (3.43), for the spin-active interface of Sec. 3.5.1 (dashed curves, for $H_{\mathrm{interf}} = E_{\mathrm{Zeeman}}\sigma_y$ with $\gamma = \pi/4$), and for the inversion-symmetry breaking interface of Sec. 3.5.2 (solid curves, for $H_{\mathrm{interf}} = V_{\mathrm{barrier}}\tau_y$ with $\gamma' = \frac{1}{2}\ln(1 + \sqrt{2})$). For $eV \gg \Delta_0$, all curves tend to the normal-state interface conductance of $0.8\,Ne^2/h$.

can itself become superconducting, forming a Weyl superconductor.[14, 116] In this section we study how the chirality blockade manifests itself in an NS junction between the normal and superconducting state of Weyl fermions. To make contact with a specific microscopic model, we consider the heterostructure approach of Burkov and Balents [63], which can describe both a Weyl semimetal and a Weyl superconductor [60, 136].

3.7.1 Heterostructure model

For the Weyl semimetal, we start from a multilayer heterostructure, composed of layers of a magnetically doped topological insulator (such as Bi_2Se_3), separated by a normal-insulator spacer layer with periodicity d. Its Hamiltonian is[63, 137, 138]

$$
\begin{aligned}
H(\boldsymbol{k}) &= v_{\mathrm{F}}\tau_z(-\sigma_y k_x + \sigma_x k_y) + \beta\tau_0\sigma_z \\
&\quad + (m_k\tau_x - \tau_y t_z \sin k_z d)\sigma_0, \\
m_k &= t'_z + t_z \cos k_z d.
\end{aligned}
\tag{3.45}
$$

The Pauli matrices σ_i act on the spin degree of freedom of the surface electrons in the topological insulator layers. The $\tau_z = \pm 1$ index distinguishes the orbitals on the top and bottom surfaces, coupled by the t'_z hopping within the same layer and by the t_z hopping from one layer to
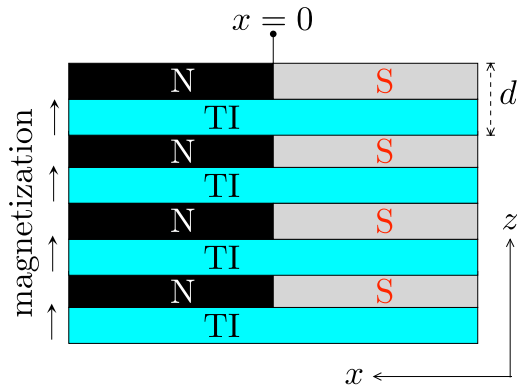
Figure 3.4: Cross-section through a layered Weyl semimetal-superconductor junction, based on the heterostructure model[60, 63] of alternating topological insulator (TI) layers and normal (N) or superconducting (S) spacer layers. In this model the orbital τ degree of freedom refers to the conducting top and bottom surfaces of the TI layers.

the next. Magnetic impurities in the topological insulator layers produce a perpendicular magnetization, leading to an exchange splitting β. The two Weyl points are at $\boldsymbol{k} = (0, 0, \pi/d \pm K)$, with

$$K^2 \approx \frac{\beta^2 - (t_z - t_z')^2}{d^2 t_z t_z'}. \tag{3.46}$$

They are closely spaced near the edge of the Brillouin zone for $|t_z - t_z'| \ll \beta \ll t_z d$.

To make contact with the generic Weyl Hamiltonian (3.1), we note the unitary transformation

$$\begin{aligned} U_0 H(\boldsymbol{k}) U_0^\dagger &= v_\mathrm{F} \tau_z(\sigma_x k_x + \sigma_y k_y) - \tau_z \sigma_z t_z \sin k_z d \\ &\quad + m_k \tau_x \sigma_0 + \beta \tau_0 \sigma_z, \\ U_0 &= \exp[-\tfrac{1}{4} i \pi (\tau_0 + \tau_x) \sigma_z]. \end{aligned} \tag{3.47}$$

We will make use of this transformation later on.

Following Meng and Balents [60], the spacer layer may have a spin-singlet s-wave pair potential Δ, with a uniform phase throughout the heterostructure (which we set to zero, allowing us to take Δ real). The pair potential induces superconductivity in the top and bottom surfaces

of the topological insulator layers, as described by the BdG Hamiltonian

$$\mathcal{H}(\boldsymbol{k}) = v_{\mathrm{F}}\nu_z\tau_z(-\sigma_y k_x + \sigma_x k_y) + \beta\nu_0\tau_0\sigma_z$$
$$+ \nu_z(m_k\tau_x - \tau_y t_z \sin k_z d)\sigma_0 - \mu\nu_z\tau_0\sigma_0 + \boldsymbol{\Delta},$$
$$\boldsymbol{\Delta} = \Delta(x)\nu_x\tau_0\sigma_0. \tag{3.48}$$

It acts on eight-component Nambu spinors Ψ with elements

$$\Psi = (\psi_{+\uparrow}, \psi_{+\downarrow}, \psi_{-\uparrow}, \psi_{-\downarrow}, \psi_{+\downarrow}^*, -\psi_{+\uparrow}^*, \psi_{-\downarrow}^*, -\psi_{-\uparrow}^*), \tag{3.49}$$

where $\pm$ refers to the top and bottom surface and $\updownarrow$ refers to the spin band.

The pair potential $\boldsymbol{\Delta}$ in Eq. (3.48) is diagonal in the τ and σ degrees of freedom. The corresponding BCS pairing interaction,

$$H_{\mathrm{BCS}} = \Delta \sum_{\boldsymbol{k}} \left[c_{+\uparrow}^\dagger(\boldsymbol{k})c_{+\downarrow}^\dagger(-\boldsymbol{k}) + c_{-\uparrow}^\dagger(\boldsymbol{k})c_{-\downarrow}^\dagger(-\boldsymbol{k}) \right] + \mathrm{H.c.}, \tag{3.50}$$

represents zero-momentum pairing of spin-up and spin-down electrons within the same conducting surface of each topological insulator layer (inversion-symmetric, spin-singlet, intra-orbital pairing).

The BCS pairing interaction (3.50) corresponds to a scalar pair potential in the spin and orbital degrees of freedom. We restrict ourselves to that pairing symmetry in this section. Other BCS pair potentials (spin-triplet and pseudoscalar spin-singlet) are considered in Appendix 3.11.

To describe a NS interface at $x = 0$, we set $\Delta(x) = 0$ for $x > 0$ and $\Delta(x) = \Delta_0$ for $x < 0$ (see Fig. 3.4). We also adjust the chemical potential $\mu(x)$, from a small value μ_{W} for $x > 0$ to a large value μ_{S} for $x < 0$. For the other parameters we take x-independent values.

3.7.2 Mode matching at the NS interface

We can now follow the mode-matching analysis of the preceding sections, with one simplification and one complication. The simplification is that, because we have the same Weyl Hamiltonian on the two sides of the NS interface, we no longer need an interface matrix to conserve current across the interface. The complication is that the block-diagonalization in the τ degree of freedom on the N side of the interface introduces off-diagonal blocks in the pair potential on the S side.

The unitary transformation that achieves this partial block-diagonalization

is

$$\tilde{\mathcal{H}} = \mathcal{V}\mathcal{H}\mathcal{V}^\dagger, \ \ \mathcal{V} = \begin{pmatrix} \tau_y\sigma_z\Omega_\theta U_0 & 0 \\ 0 & \Omega_\theta U_0 \end{pmatrix}, \tag{3.51}$$

$$\Omega_\theta = \exp(-\tfrac{1}{2}i\theta\tau_y\sigma_z),$$

with U_0 from Eq. (3.47). The k_z-dependent angle θ is defined by

$$\cos\theta = (t_z\sin k_z d)/M_k, \ \ \sin\theta = m_k/M_k,$$

$$M_k = \sqrt{m_k^2 + t_z^2\sin^2 k_z d}. \tag{3.52}$$

For closely-spaced Weyl points (when $|t_z - t_z'| \ll \beta \ll t_z d$) we may approximate $\sin\theta \approx 0$, $|\cos\theta| \approx 1$.

The transformed Hamiltonian is

$$\tilde{\mathcal{H}}(\boldsymbol{k}) = v_\mathrm{F}\nu_z\tau_z(\sigma_x k_x + \sigma_y k_y) + M_k\nu_0\tau_z\sigma_z + \beta\nu_0\tau_0\sigma_z$$

$$- \mu\nu_z\tau_0\sigma_0 + \tilde{\boldsymbol{\Delta}},$$

$$\tilde{\boldsymbol{\Delta}} \equiv \mathcal{V}\boldsymbol{\Delta}\mathcal{V}^\dagger = \Delta(x)\nu_x\tau_y\sigma_z. \tag{3.53}$$

This has the same block-diagonal form (3.23) on the N side $x > 0$ of the interface (where $\Delta = 0$), but on the S side $x < 0$ the transformed pair potential $\tilde{\boldsymbol{\Delta}}$ is off-diagonal in the τ degree of freedom. [3]

We again assume $\mu_\mathrm{S} \gg \mu_\mathrm{W}$ so that in S we may neglect the transverse wave vector component k_y and take k_z at the Weyl point, where $M_k = \beta$. The wave equation in S corresponding to the Hamiltonian (3.53) then reads

$$v_\mathrm{F}\frac{\partial}{\partial x}\psi(x) = X_\mathrm{S}\psi(x), \ \ x < 0, \tag{3.54}$$

$$X_\mathrm{S} = i(E\nu_z + \mu_\mathrm{S}\nu_0)\tau_z\sigma_x - \beta\nu_z(\tau_0 + \tau_z)\sigma_y - \Delta_0\nu_y\tau_x\sigma_y.$$

As derived in Appendix 3.10, the decaying eigenvectors for $E < \Delta_0$ and $x \to -\infty$ satisfy

$$\nu_x\tau_y\sigma_z\psi = \exp(i\alpha\nu_z\tau_z\sigma_x)\psi, \tag{3.55}$$

with $\alpha = \arccos(E/\Delta_0) \in (0, \pi/2)$. The corresponding boundary condition on $\psi = (\psi_e, \psi_h)$ is

$$\psi_h(0) = \mathcal{T}\psi_e(0), \ \ \mathcal{T} = e^{i\alpha\tau_z\sigma_x}\tau_y\sigma_z. \tag{3.56}$$

---

[3]We should note that our Eq. (3.53), with a pair potential that is off-diagonal in τ, disagrees with Eqs. 5–8 of Ref. 60, which have a fully block-diagonal Hamiltonian in the layer degree of freedom. We do agree on the Hamiltonian before the unitary transformation [our Eq. (3.48) and Eqs. 1–3 in Ref. 60] and we have traced the discrepancy to an algebraic error.

Because $\psi(x)$ is now continuous across the interface, we do not need to distinguish 0^+ and 0^- as we needed to do in Sec. 3.4.1.

Substitution of $\mathcal{T}$ into the mode matching equation (3.43) gives $r_{he} \equiv 0$; fully suppressed Andreev reflection at all energies and all angles of incidence. This is the chirality blockade.

3.8 Fermi-arc mediated Josephson effect

While the conductance of a single NS interface is fully suppressed by the chirality blockade, the supercurrent through an SNS junction is nonzero because of overlapping surface states (Fermi arcs) on the two NS interfaces. We have calculated this Fermi-arc mediated Josephson effect (see Appendix 3.12), and we summarize the results.

The Fermi arcs connect the Weyl cones of opposite chirality [62]. As they pass through the center of the Brillouin zone, the chirality blockade is no longer operative and the Fermi arcs acquire a mixed electron-hole character. At $k_z = 0$, the surface states are charge neutral Majorana fermions [61].

The Fermi arcs are bound to the NS interface over a distance of order v_F/β, so a coupling of the two NS interfaces is possible if their separation $L \lesssim v_F/\beta$. For larger L, the critical current is suppressed $\propto \exp(-L/\xi_{\mathrm{arc}})$, with $\xi_{\mathrm{arc}} \simeq v_F/\beta$ the penetration depth of the surface Fermi arc into the bulk (see Fig. 3.5).

3.9 Discussion

In conclusion, we have shown that Andreev reflection at the interface between a Weyl semimetal and a spin-singlet s-wave superconductor is suppressed by a mismatch of the chirality of the incident electron and the reflected hole. Zero-momentum (s-wave) pairing requires that the electron and hole have opposite chirality, while singlet pairing requires that they occupy opposite spin bands, and these two requirements are incompatible, as illustrated in Fig. 3.1.

We have identified two mechanisms that can remove the chirality blockade and activate Andreev reflection. The first mechanism, a spin-active interface, has the same effect as spin-triplet pairing: it enables Andreev reflection by allowing an electron and a hole to be in the same spin band. The second mechanism, inversion-symmetry breaking either at the interface or in the pair potential, is more subtle, as we now discuss.
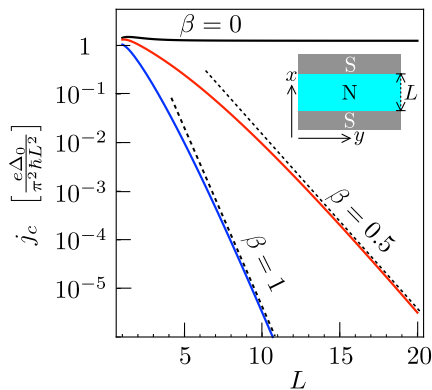
Figure 3.5: Critical current density j_c of the SNS junction as a function of the separation L of the NS interfaces for different values of β, calculated from the Hamiltonian (3.48) for $\mu = 0$, $v_F = t_z = t'_z = d = 1$. The dashed lines indicate the exponential decay $\propto e^{-c\beta L/v_F}$ with $c = 1.7$.

Consider the single-cone Weyl Hamiltonian centered at $\boldsymbol{k} = (0, 0, +K)$,

$$H_+ = v_x k_x \sigma_x + v_y k_y \sigma_y + v_z (k_z - K)\sigma_z. \tag{3.57}$$

By definition, its chirality is $C = \text{sign}\,(v_x v_y v_z)$. For the second Weyl cone centered at $\boldsymbol{k} = (0, 0, -K)$ of opposite chirality, we can take either

$$H_- = -v_x k_x \sigma_x - v_y k_y \sigma_y - v_z (k_z + K)\sigma_z \tag{3.58}$$

or

$$H'_- = v_x k_x \sigma_x + v_y k_y \sigma_y - v_z (k_z + K)\sigma_z, \tag{3.59}$$

or some permutation of x, y, z, but either all three signs or one single sign of the velocity components must flip. The first choice satisfies inversion symmetry, $H_-(-\boldsymbol{k}) = H_+(\boldsymbol{k})$, while the second choice does not. In Fig. 3.6 we show the spin-momentum locking in the pair of Weyl cones $H_W = (H_+, H_-)$ and $H'_W = (H_+, H'_-)$ with and without inversion symmetry. We see that the chirality blockade can be removed by breaking inversion symmetry.

This explains why Uchida, Habe, and Asano [121] (who, with Cho, Bardarson, Lu, and Moore [139], fully appreciated the importance of spin-momentum locking for superconductivity in a Weyl semimetal) did not find any suppression of Andreev reflection at normal incidence on the NS interface. Their two-band model[4] of a Weyl semimetal [130, 140] has the

---

[4]The Hamiltonian $H'_W = (H_+, H'_-)$ is called a two-band model because near the
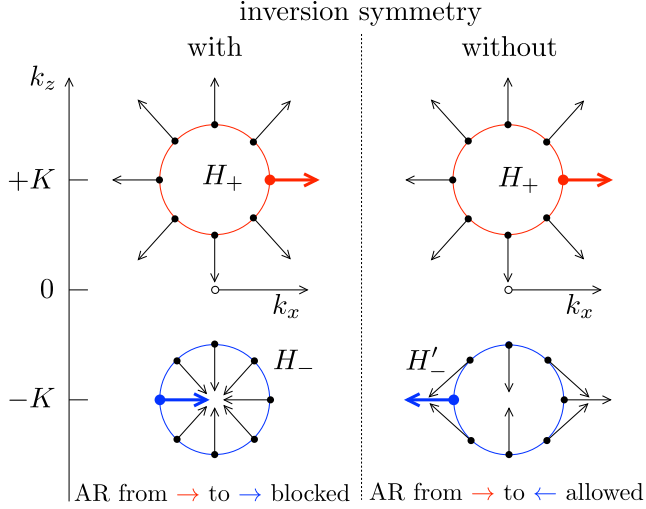
Figure 3.6: Illustration of the spin-momentum locking for states at the Fermi energy in a pair of Weyl cones at $\boldsymbol{k} = (0, 0, \pm K)$. The arrows indicate the direction of the spin polarization for a momentum eigenstate at $k_y = 0$, as a function of k_x and k_z. The left column is for the Hamiltonian $H_W = (H_+, H_-)$ with inversion symmetry, the right column is for $H'_W = (H_+, H'_-)$ without inversion symmetry. Andreev reflection (AR) along the x-direction on a superconductor with zero-momentum spin-singlet pairing is blocked for H_W (the red and blue arrows point in the same direction, so the spin is not inverted, as it should be for spin-singlet pairing), while it is allowed for H'_W (red and blue arrows point in opposite directions).

same spin texture as H'_W — hence it breaks inversion symmetry and does not show the chirality blockade. The relevance of inversion symmetry also explains why no chirality blockade appeared in Refs. 122–124, where a pseudoscalar pair potential was used that breaks this symmetry (see Appendix 3.11.2).

The chirality blockade suppresses the superconducting proximity effect, but since it can be lifted in a controlled way by a Zeeman field (see Fig. 3.2), it offers opportunities for spintronics applications. In the geometry of Fig. 3.1, a magnetic field in the y-direction, in the plane of the NS interface and perpendicular to the magnetization, activates Andreev reflection when the Zeeman energy E_{Zeeman} becomes comparable to the superconducting gap Δ_0. (To prevent pair-breaking effects from this Zeeman field one can

---

Weyl points Eqs. (3.57) and (3.59) can be combined into a single 2×2 matrix of the form $v_x k_x \sigma_x + v_y k_y \sigma_y + (v_z/2K)(k_z^2 - K^2)\sigma_z$. No additional orbital degree of freedom is needed, as in the four-band model (3.1). The inversion-symmetry breaking remains hidden unless there are spin-dependent processes that couple the Weyl cones, as in Andreev reflection.

use a thin-film superconductor with strong spin-orbit coupling [141].) For a typical Zeeman energy of 1 meV/Tesla and a typical gap of 0.1 meV, a 100 mT magnetic field can then activate the transfer of Cooper pairs through the NS interface. This provides a phase-insensitive alternative to the phase-sensitive control of Cooper pair transfer in a Josephson junction.

3.10 Appendix A. Derivation of the boundary condition at a Weyl semimetal − Weyl superconductor interface

Equation (3.26) gives the effective boundary condition at the NS interface between a Weyl semimetal and a conventional superconductor. Here we generalize this to the interface between a Weyl semimetal and a Weyl superconductor. We allow for a more general pairing symmetry than considered in the main text, and in Appendix 3.11 we apply the boundary condition to spin-triplet pairings and to a pseudoscalar spin-singlet pairing.

As discussed in the related context of graphene [133], the *local* coupling of electrons and holes at the NS interface that is expressed by the effective boundary condition holds under three conditions: (i) The chemical potential μ_S in the superconducting region is the largest energy scale in the problem, much larger than the superconducting gap Δ_0 and much larger than the chemical potential μ_N in the normal region; (ii) the interface is smooth and impurity-free on the scale of the superconducting coherence length $\hbar v_\mathrm{F}/\Delta_0$; and (iii) there is no lattice mismatch at the NS interface.

We start from Eq. (3.54), which governs the decay of the wave function in the superconducting region,

$$v_\mathrm{F}\frac{\partial}{\partial x}\psi(x) = X_\mathrm{S}\psi(x), \quad x < 0, \tag{3.60}$$

$$X_\mathrm{S} = (i\mu_\mathrm{S}\tau_z\sigma_x + Y_\mathrm{S}), \quad Y_\mathrm{S} = i\nu_z\tau_z\sigma_x(E - \tilde{\mathbf{\Delta}}).$$

We have omitted the β term, which anticommutes with the μ_S term and can be neglected in the large-μ_S limit. We seek a boundary condition on ψ at $x = 0$ that ensures decay for $x \to -\infty$.

In the most general case, $\tilde{\mathbf{\Delta}}$ is an Hermitian 8×8 matrix that satisfies the electron-hole symmetry relation

$$\nu_y\sigma_y\tilde{\mathbf{\Delta}}^*\nu_y\sigma_y = -\tilde{\mathbf{\Delta}}. \tag{3.61}$$

We make the following four additional assumptions:

1. $\tilde{\boldsymbol{\Delta}}$ anticommutes with ν_z (so it is fully off-diagonal in the electron-hole degree of freedom);

2. $\tilde{\boldsymbol{\Delta}}$ commutes with $\tau_z \sigma_x$ (anticommuting terms do not contribute to the spectrum of X_S in the large-μ_S limit, so they may be ignored);

3. $\tilde{\boldsymbol{\Delta}}$ is independent of the momentum perpendicular to the NS interface (it may depend on the parallel momentum);

4. $\tilde{\boldsymbol{\Delta}}$ squares to a scalar Δ_0^2 (this assumption is not essential, but allows for a simple closed-form answer).

Under these conditions X_S and Y_S commute, so they can be diagonalized simultaneously. Moroever, $Y_S^2 = \Delta_0^2 - E^2$, hence a decaying wave function for $E < \Delta_0$ is an eigenfunction of Y_S with eigenvalue $+\sqrt{\Delta_0^2 - E^2}$,

$$Y_S \psi = \sqrt{\Delta_0^2 - E^2}\, \psi. \tag{3.62}$$

We rearrange this to obtain a relation between the electron and hole components of $\psi = (\psi_e, \psi_h)$:

$$-i\nu_z \tau_z \sigma_x \tilde{\boldsymbol{\Delta}} \psi = \left(-iE\nu_z \tau_z \sigma_x + \sqrt{\Delta_0^2 - E^2} \right) \psi$$

$$\Rightarrow \tilde{\boldsymbol{\Delta}} \psi = \left(E + i\sqrt{\Delta_0^2 - E^2}\, \nu_z \tau_z \sigma_x \right) \psi$$

$$\Rightarrow \tilde{\boldsymbol{\Delta}} \psi = \Delta_0 \exp(i\alpha \nu_z \tau_z \sigma_x) \psi, \tag{3.63}$$

with $\alpha = \arccos (E/\Delta_0) \in (0, \pi/2)$. For a superconducting phase φ we can decompose

$$\tilde{\boldsymbol{\Delta}} = \Delta_0 (\nu_x \cos\varphi - \nu_y \sin\varphi)\boldsymbol{\chi}, \tag{3.64}$$

with $\boldsymbol{\chi}$ a 4×4 Hermitian matrix that squares to unity and commutes with $\tau_z \sigma_x$. We thus arrive at the desired boundary condition,

$$e^{i\varphi} \boldsymbol{\chi} \psi_h(0) = e^{i\alpha \tau_z \sigma_x} \psi_e(0). \tag{3.65}$$

In a more general geometry, with a unit vector $\boldsymbol{n}$ in the x–y plane perpendicular to the NS interface and pointing from N to S, we can write the boundary condition as

$$\psi_h(0) = \mathcal{T} \psi_e(0), \quad \mathcal{T} = e^{-i\varphi} \exp\big[-i\alpha \tau_z (\boldsymbol{n} \cdot \boldsymbol{\sigma})\big]\boldsymbol{\chi}. \tag{3.66}$$

This was derived for subgap energies $E < \Delta_0$. The boundary condition still holds by analytic continuation for $E > \Delta_0$, when $\alpha = -i \operatorname{arcosh}(E/\Delta_0)$ is imaginary, provided that there is no particle current incident on the NS interface from the superconducting side.

3.11 Appendix B. Generalizations to other pairing symmetries

The pair potential $\boldsymbol{\Delta} = \Delta_0 \nu_x \tau_0 \sigma_0$ in the Meng-Balents Hamiltonian (3.48) represents inversion-symmetric, spin-singlet, intra-orbital pairing, appropriate for the heterostructure model of Fig. 3.4. Other types of pairing may be relevant for Weyl semimetals with intrinsic superconductivity.[136, 138] We calculate the corresponding Andreev reflection probabilities.

3.11.1 Spin-triplet pair potential

For the three $s = x, y, z$ spin-triplet pairings, the relationship between the pair potential $\boldsymbol{\Delta}_s$ in the Hamiltonian (3.48) and the transformed pair potential $\tilde{\boldsymbol{\Delta}}_s$ in the Hamiltonian (3.53) is

$$\boldsymbol{\Delta}_s = \Delta_0 \nu_x \tau_y \sigma_s \Rightarrow \tilde{\boldsymbol{\Delta}}_s = -\Delta_0 \nu_y \boldsymbol{\chi}_s, \tag{3.67a}$$

$$\boldsymbol{\chi}_x = -\tau_0 \sigma_x \cos\theta - \tau_y \sigma_y \sin\theta, \tag{3.67b}$$

$$\boldsymbol{\chi}_y = -\tau_0 \sigma_y \cos\theta + \tau_y \sigma_x \sin\theta, \tag{3.67c}$$

$$\boldsymbol{\chi}_z = \tau_x \sigma_z \cos\theta - \tau_z \sigma_0 \sin\theta. \tag{3.67d}$$

Each $\boldsymbol{\chi}_s$ squares to unity but only $\boldsymbol{\chi}_x$ and $\boldsymbol{\chi}_z$ commute with $\tau_z \sigma_x$. The $s = y$ pairing anticommutes and does not open a gap in the large-μ_S limit. For the $s = x$ and $s = z$ pairings we can read off the electron-hole coupling matrix $\mathcal{T}_s$ from Eq. (3.66),

$$\mathcal{T}_s = -i e^{i\alpha \tau_z \sigma_x} \boldsymbol{\chi}_s, \tag{3.68}$$

and then derive the Andreev reflection amplitude by solving Eq. (3.43). The result for normal incidence is

$$r_{he} = \frac{2 \sin\alpha \cos\theta}{\cos^2\theta - e^{2i\alpha}}, \quad \text{for } s = x, \tag{3.69a}$$

$$r_{he} = -\frac{2i \cos\alpha \sin\theta}{\sin^2\theta + e^{2i\alpha}}, \quad \text{for } s = z. \tag{3.69b}$$

More generally, for any angle of incidence, we have at the Fermi level (when $E = 0 \Rightarrow \alpha = \pi/2$) the Andreev reflection probabilities

$$
\begin{aligned}
R_{he} &= \frac{v_{\mathrm{F}}^2 k_x^2}{\mu^2 - v_{\mathrm{F}}^2 k_y^2} \frac{4 \cos^2 \theta}{(1 + \cos^2 \theta)^2}, \quad \text{for } s = x, \\
R_{he} &= 0, \quad \text{for } s = z.
\end{aligned}
\tag{3.70}
$$

3.11.2 Pseudoscalar spin-singlet pair potential

The pairing interaction

$$
\begin{aligned}
H'_{\mathrm{BCS}} &= \Delta \sum_{\boldsymbol{k}} \left[c_{+\uparrow}^\dagger(\boldsymbol{k}) c_{+\downarrow}^\dagger(-\boldsymbol{k}) - c_{-\uparrow}^\dagger(\boldsymbol{k}) c_{-\downarrow}^\dagger(-\boldsymbol{k}) \right] \\
&\quad + \text{H.c.}
\end{aligned}
\tag{3.71}
$$

differs from H_{BCS} in Eq. (3.50) by a π phase shift of the pair potential on the top and bottom surfaces. The corresponding pair potential in the BdG Hamiltonian (3.48) is

$$
\boldsymbol{\Delta}' = \Delta_0 \nu_x \tau_z \sigma_0.
\tag{3.72}
$$

It anticommutes with τ_x and thus changes sign upon inversion, representing a pseudoscalar pairing in the classification of Ref. 120.

Bednik, Zyuzin, and Burkov[136] obtain the pseudoscalar pairing (3.71) in a model where the pairing interaction is intrinsic to the Weyl semimetal, rather than proximity-induced as in the multilayer structure of Fig. 3.4. (The τ degree of freedom then refers to a molecular orbital instead of to a heterostructure layer.)

The change from scalar to pseudoscalar pairing has drastic consequences for Andreev reflection: The transformed pair potential in Eq. (3.53),

$$
\tilde{\boldsymbol{\Delta}}' \equiv \mathcal{V} \boldsymbol{\Delta}' \mathcal{V}^\dagger = -\Delta_0 \nu_x \tau_0 \sigma_0,
\tag{3.73}
$$

is *diagonal* rather than off-diagonal in the τ degree of freedom. We can therefore project the transformed Hamiltonian,

$$
\begin{aligned}
\tilde{\mathcal{H}}'(\boldsymbol{k}) &= v_{\mathrm{F}} \nu_z \tau_z (\sigma_x k_x + \sigma_y k_y) + M_k \nu_0 \tau_z \sigma_z + \beta \nu_0 \tau_0 \sigma_z \\
&\quad - \mu \nu_z \tau_0 \sigma_0 - \Delta_0 \nu_x \tau_0 \sigma_0,
\end{aligned}
\tag{3.74}
$$

onto the $\tau = -1$ subband without losing the pair potential. There is now

no chirality blockade. The Andreev reflection amplitude is

$$r_{he} = -E/\Delta_0 + i\sqrt{1 - E^2/\Delta_0^2}, \tag{3.75a}$$

at normal incidence for any energy,

$$r_{he} = \frac{ik_x}{\sqrt{k_x^2 + k_y^2}}, \tag{3.75b}$$

at the Fermi level for any angle of incidence.

The projected Hamiltonian,

$$\begin{aligned}
\tilde{\mathcal{H}}'_{\tau=-1} = {} & -v_{\rm F}\nu_z(\sigma_x k_x + \sigma_y k_y) + (\beta - M_k)\nu_0\sigma_z \\
& - \mu\nu_z\sigma_0 - \Delta_0\nu_x\sigma_0,
\end{aligned} \tag{3.76}$$

is essentially the one studied in Refs. 122–124. This explains why no chirality blockade was obtained in those studies of Andreev reflection in a Weyl semimetal.

3.11.3 Comparison with tight-binding model simulations

To test these analytical formulas, we have discretized the eight-orbital Hamiltonian (3.48) on a cubic lattice, and we solved the scattering problem at the NS interface numerically, using the Kwant toolbox.[142]

Equation (3.48) is linear in k_x and k_y, and a straightforward discretization, by replacing $k_x \mapsto \sin k_x$, $k_y \mapsto \sin k_y$, would suffer from fermion doubling. To avoid this, we follow Ref. 132 and add quadratic terms in k_x and k_y to the mass term m_k, resulting in the tight-binding Hamiltonian

$$\begin{aligned}
\mathcal{H}(\boldsymbol{k}) = {} & \nu_z\tau_z(-\sigma_y \sin k_x + \sigma_x \sin k_y) + \beta\nu_0\tau_0\sigma_z \\
& + \nu_z(m_{\boldsymbol{k}}\tau_x - \tau_y \sin k_z)\sigma_0 - \mu\nu_z\tau_0\sigma_0 + \boldsymbol{\Delta},
\end{aligned} \tag{3.77a}$$

$$m_{\boldsymbol{k}} = 3 + \cos k_z - \cos k_x - \cos k_y. \tag{3.77b}$$

For simplicity we have set the Fermi velocity $v_{\rm F}$ and the hopping energies t_z, t'_z equal to unity, and we have taken the same lattice constant $d = a \equiv 1$ parallel and perpendicular to the layers.

The Weyl points are at $\boldsymbol{k} = (0, 0, \pi \pm K)$, where

$$(1 - \cos K)^2 + \sin^2 K = \beta^2 \Rightarrow K = \arctan\left(\frac{\beta\sqrt{4 - \beta^2}}{2 - \beta^2}\right). \tag{3.78}$$
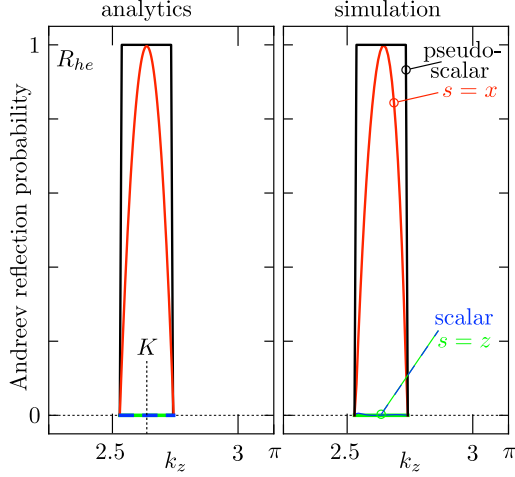
Figure 3.7: Andreev reflection probability at the Fermi level of a Weyl semimetal – Weyl superconductor interface, for four different pairing symmetries in the superconductor (scalar and pseudoscalar spin-singlet, and $s = x$ or $s = z$ spin-triplet). The left panel shows the analytical results (3.80) for $k_y = 0$, $\beta = 0.5$, $\mu_W = 0.1$. The right panel shows the results from a numerical simulation of the tight-binding model (3.77), with additional parameters $\mu_S = 0.4$, $\Delta_0 = 0.55$. There are two Weyl points at $k_z = \pi \pm K$, only one of which is shown (the other gives the same results).

Near the Weyl point, the normal-state dispersion is

$$(E + \mu_W)^2 = k_x^2 + k_y^2 + q_z^2,$$
$$q_z = (\pi - K - k_z)\cos\theta, \quad \cos^2\theta = 1 - \beta^2/4. \tag{3.79}$$

The analytical results for the Andreev reflection probability at the Fermi level ($E = 0$), as a function of the transverse momenta k_y and q_z, are:

$$R_{he} = \frac{4 - \beta^2}{(2 - \beta^2/4)^2} \frac{\mu_W^2 - k_y^2 - q_z^2}{\mu_W^2 - k_y^2}, \quad s = x \text{ triplet pairing}, \quad \mathbf{\Delta} = \Delta_0 \nu_x \tau_y \sigma_x, \tag{3.80a}$$

$$R_{he} = 0, \qquad\qquad s = z \text{ triplet pairing}, \quad \mathbf{\Delta} = \Delta_0 \nu_x \tau_y \sigma_z, \tag{3.80b}$$

$$R_{he} = \frac{\mu_W^2 - k_y^2 - q_z^2}{\mu_W^2 - q_z^2}, \qquad\qquad \text{pseudoscalar singlet pairing}, \quad \mathbf{\Delta} = \Delta_0 \nu_x \tau_z \sigma_0, \tag{3.80c}$$

$$R_{he} = 0, \qquad\qquad \text{scalar singlet pairing}, \quad \mathbf{\Delta} = \Delta_0 \nu_x \tau_0 \sigma_0. \tag{3.80d}$$
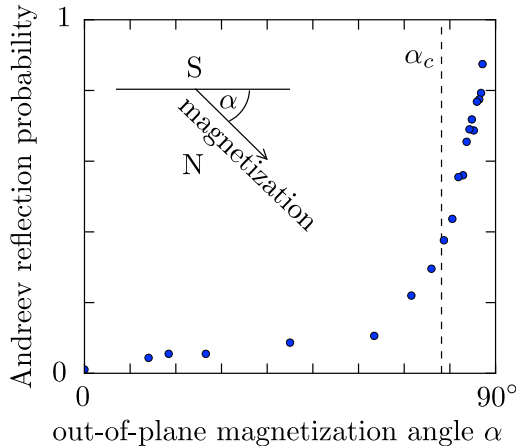
Figure 3.8: Threshold dependence of the chirality blockade on the direction of the magnetization. The horizontal axis shows the out-of-plane rotation angle α of the magnetization, the vertical axis shows the Andreev reflection probability at the Fermi level for normal incidence. The data points are calculated numerically from the tight-binding model (3.77) with a scalar pair potential (parameters $\mu_{\mathrm{W}} = 0.18$, $\mu_{\mathrm{S}} = 0.2$, $\Delta_0 = 0.9$, $\beta = 0.85$). The dashed vertical line is the threshold angle $\alpha_c = \arccos{(\mu_{\mathrm{W}}/\beta)} = 78°$ expected for an isotropic Weyl cone.

In Fig. 3.7 we compare the analytics with the numerical simulation, and find good agreement without any fit parameter.

All of this is for a magnetization in the plane of the NS interface. If the magnetization is rotated out of the plane by an angle α, the Andreev reflection probability for scalar pairing shows the threshold behavior discussed in Sec. 3.2, see Fig. 3.8. The threshold angle given by $\cos\alpha_{\mathrm{c}} = k_{\mathrm{F}}/K \approx \mu_{\mathrm{W}}/\beta$ for an isotropic Weyl cone is in reasonable approximation with the numerical result, with some deviations because the Weyl cone of the Hamiltonian (3.77) has a significant anisotropy.

3.12 Appendix C. Calculation of the Fermi-arc mediated Josephson effect

We calculate the supercurrent flowing through an SNS junction in response to a phase difference ϕ between the superconducting pair potentials. As explained in Sec. 3.8, because of the chirality blockade of Andreev reflection this supercurrent is due entirely to overlapping Fermi arcs on the two NS surfaces. It is exponentially small when the distance L of the NS

interfaces is large compared to the decay length v_F/β of the surface states into the bulk. This is the key difference between the present calculation for the Weyl semimetal Josephson junction and a similar calculation for a graphene Josephson junction in Ref. 133.

3.12.1 Andreev bound states

We start from the Hamiltonian (3.48),

$$
\begin{aligned}
\mathcal{H} = {}& v_F \nu_z \tau_z (-\sigma_y k_x + \sigma_x k_y) + \beta \nu_0 \tau_0 \sigma_z \\
& + \nu_z (m_k \tau_x - \tau_y t_z \sin k_z d) \sigma_0 - \mu \nu_z \tau_0 \sigma_0 \\
& + \Delta_0 (\nu_x \cos \varphi - \nu_y \sin \varphi) \tau_0 \sigma_0,
\end{aligned} \tag{3.81}
$$

generalized to account for a complex pair potential $\Delta_0 e^{i\varphi}$. In the N region $|x| < L/2$ we set $\Delta_0 = 0$, while in the S regions $|x| > L/2$ we have a nonzero gap Δ_0 and a phase φ equal to $\phi/2$ for $x > L/2$ and equal to $-\phi/2$ for $x < -L/2$.

We carry out a (partial) block-diagonalization by means of the unitary transformations $\mathcal{H} \mapsto \mathcal{W}\mathcal{V}\mathcal{H}\mathcal{V}^\dagger\mathcal{W}^\dagger$, with $\mathcal{V}$ defined in Eq. (3.51) and $\mathcal{W}$ defined by

$$
\mathcal{W} = \begin{pmatrix} i\tau_y \sigma_z & 0 \\ 0 & \tau_0 \sigma_0 \end{pmatrix}. \tag{3.82}
$$

The resulting Hamiltonian

$$
\begin{aligned}
\mathcal{H} = {}& v_F \nu_z \tau_z \big(k_x \sigma_x + k_y \sigma_y - M_k \sigma_z \big) + \beta \nu_0 \tau_0 \sigma_z \\
& - \mu \nu_z \tau_0 \sigma_0 + \Delta_0 (\nu_x \cos \varphi - \nu_y \sin \varphi) \tau_0 \sigma_0
\end{aligned} \tag{3.83}
$$

is diagonal in τ. We may therefore replace τ_z by the variable $\tau = \pm 1$ and τ_0 by 1.

At the NS interfaces $x = \pm L/2$ we have the boundary condition (3.66),

$$
\begin{aligned}
& \psi_h(\pm L/2) = \mathcal{T}^{\pm 1} \psi_e(\pm L/2), \\
& \mathcal{T} = e^{-i\phi/2} e^{-i\alpha\tau\sigma_x}, \quad \alpha = \arccos(E/\Delta_0).
\end{aligned} \tag{3.84}
$$

Integration of $\mathcal{H}\psi = E\psi$, with $\psi = (\psi_+, \psi_-)$ the two ν-components of the wave function, gives the x-dependence in the N region,

$$
\psi_\pm(x) = e^{x\,\Xi_\pm} \psi_\pm(0), \quad -L/2 < x < L/2, \tag{3.85a}
$$

$$
\Xi_\pm = i\tau\sigma_x \frac{\mu \pm E}{v_F} - \sigma_y \frac{M_k \pm \tau\beta}{v_F} + \sigma_z k_y. \tag{3.85b}
$$

A bound state in the SNS junction, a socalled Andreev level, appears at energies when[133]

$$\det \left(1 - e^{-L\,\Xi_+}\,\mathcal{T}\,e^{L\,\Xi_-}\,\mathcal{T}\right) = 0. \tag{3.86}$$

We assume that the separation L of the NS interfaces is small compared to the superconducting coherence length $\xi = v_{\mathrm{F}}/\Delta_0$. In this short-junction regime the energy dependence of $\Xi_\pm$ can be neglected and only the energy dependence of $\mathcal{T}$ needs to be retained [143].

Introducing the vector notation $\boldsymbol{\sigma} = (\sigma_x, \sigma_y, \sigma_z)$ and defining

$$\mathbf{d}_\pm = (d_x, d_{\pm,y}, d_z) = \frac{L}{v_{\mathrm{F}}}\big(i\tau\mu, -M_k \pm \tau\beta, v_{\mathrm{F}}\sin k_y\big), \tag{3.87}$$

the bound-state condition can be written as

$$\det \left(e^{-i\phi/2}e^{\mathbf{d}_-\cdot\boldsymbol{\sigma}} - e^{i\phi/2}\,e^{i\alpha\sigma_x}\,e^{\mathbf{d}_+\cdot\boldsymbol{\sigma}}\,e^{i\alpha\sigma_x}\right) = 0. \tag{3.88}$$

To simplify the equations we define

$$\operatorname{sinhc} x = \frac{\sinh x}{x}. \tag{3.89}$$

The identity

$$e^{\mathbf{d}\cdot\boldsymbol{\sigma}} = \sigma_0 \cosh d + (\mathbf{d}\cdot\boldsymbol{\sigma})\operatorname{sinhc} d, \quad d = \sqrt{\mathbf{d}\cdot\mathbf{d}}, \tag{3.90}$$

allows us to evaluate the determinant Eq. (3.88) as

$$\gamma_0^2 = \gamma_1^2 + \gamma_2^2 + \gamma_3^2, \tag{3.91}$$

where

$$\gamma_0 = e^{-i\phi/2}\cosh d_- - e^{i\phi/2}\big(\cos 2\alpha\,\cosh d_+$$
$$+ i\sin 2\alpha\,d_x \operatorname{sinhc} d_+\big), \tag{3.92a}$$

$$\gamma_1 = e^{-i\phi/2}d_x \operatorname{sinhc} d_- - e^{i\phi/2}\big(i\sin 2\alpha\,\cosh d_+$$
$$+ \cos 2\alpha\,d_x \operatorname{sinhc} d_+\big), \tag{3.92b}$$

$$\gamma_2 = e^{-i\phi/2}d_{-,y}\operatorname{sinhc} d_- - e^{i\phi/2}d_{+,y}\operatorname{sinhc} d_+, \tag{3.92c}$$

$$\gamma_3 = e^{-i\phi/2}d_z \operatorname{sinhc} d_- - e^{i\phi/2}d_z \operatorname{sinhc} d_+. \tag{3.92d}$$

The phase dependence of the bound-state energy can be solved exactly from Eq. (3.91) when the Fermi level is near the Weyl points, $|\mu| \ll v_\mathrm{F}/L$:

$$E(\phi) = \Delta_0 \sqrt{\tfrac{1}{2} + p(\phi)} \tag{3.93a}$$

$$p(\phi) = \frac{1 + (\mathbf{d}_- \cdot \mathbf{d}_+) \sinh\!c\, d_- \sinh\!c\, d_+}{2\cosh d_- \cosh d_+}$$

$$\quad - \frac{\sin^2(\phi/2)}{\cosh d_- \cosh d_+}, \tag{3.93b}$$

where the $\mathbf{d}_\pm$ are taken at $\mu = 0$. The energy levels are doubly degenerate in $\tau = \pm 1$. This degeneracy is lifted by a finite chemical potential: The first-order correction $\delta E_\pm$ to the bound state energy reads

$$\delta E_\pm = \pm \frac{L|\mu|\Delta_0}{2v_\mathrm{F}} \left| \frac{\tanh d_+}{d_+} - \frac{\tanh d_-}{d_-} \right| \sqrt{\tfrac{1}{2} - p(\phi)}. \tag{3.94}$$

3.12.2 Josephson current

In the short-junction limit only the Andreev levels contribute to the supercurrent density [143], according to

$$j(\phi) = -\frac{e}{\hbar} \sum_{\tau=\pm 1} \int_{-\pi}^{\pi} \frac{dk_y}{2\pi} \int_{-\pi}^{\pi} \frac{dk_z}{2\pi} \frac{dE(\phi)}{d\phi}. \tag{3.95}$$

We take $\mu \ll v_\mathrm{F}/L$ and substitute Eq. (3.93), to arrive at

$$j(\phi) = \frac{e\Delta_0}{8\pi^2\hbar} \int_{-\pi}^{\pi} dk_y \int_{-\pi}^{\pi} dk_z \frac{\sin\phi}{\cosh d_- \cosh d_+ \sqrt{\tfrac{1}{2} + p(\phi)}}. \tag{3.96}$$

(The integrand is symmetric in $\tau = \pm$, so the sum over τ has been omitted in favor of an overall factor of 2.)

We take parameters $v_\mathrm{F} = t_z = t_z' = d = 1$, when

$$M_k = \sqrt{(1 + \cos k_z)^2 + \sin^2 k_z} = 2\cos(k_z/2). \tag{3.97}$$

The current-phase relationship is close to sinusoidal, see Fig. 3.9. The critical current can then be accurately approximated by $j_c \approx j(\pi/2)$. This is plotted as a function of L in Fig. 3.5. It decays $\propto \exp(-L/\xi_\mathrm{arc})$, with $\xi_\mathrm{arc} \simeq v_\mathrm{F}/\beta$ the penetration depth of the surface Fermi arc into the bulk.
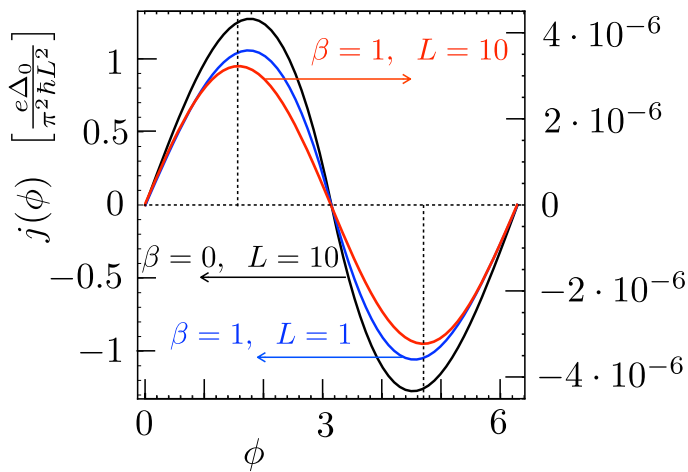
Figure 3.9: Current-phase relationship of the Josephson current density for various values of β and L. The extrema are close to $\pi/2$ and $3\pi/2$, indicated by the dashed lines. This is calculated from Eq. (3.96) for $v_{\mathrm{F}} = t_z = t'_z = d = 1$.

4 Twisted Fermi surface of a thin-film Weyl semimetal

4.1 Introduction

The Fermi surface of degenerate electrons separates filled states inside from empty states outside, thereby governing the electronic transport properties near equilibrium. In a two-dimensional electron gas (2DEG) the Fermi surface is a closed equi-energy contour in the momentum plane. It is a circle for free electrons, with deformations from the lattice potential such as the trigonal warping of graphene or the hexagonal warping on the surface of a topological insulator [144]. These are all smooth deformations which do not change the orientation of the Fermi surface: The turning number is 1, meaning that the tangent vector makes one full rotation as we pass along the equi-energy contour.

The turning number

$$\nu = \frac{1}{2\pi} \oint_\Gamma \mathcal{C} \, dl, \tag{4.1}$$

defined as the contour integral of the curvature $\mathcal{C}$ in units of 2π, identifies topologically distinct deformations of the circle in the plane, socalled "regular homotopy classes" [145]. A theorem going back to Gauss [146] says that a contour Γ with turning number ν has $s \geq \left||\nu| - 1\right|$ self-intersections and that the sum $|\nu| + s$ must be an odd integer. Fig. 4.1 shows examples of contours with $\{\nu, s\} = \{0, 1\}$, $\{1, 0\}$, and $\{2, 1\}$.

The turning number is preserved by any smooth deformation of the contour. This includes socalled "uncrossing" deformations [145]: As illustrated in Fig. 4.1, uncrossing breaks up a self-intersecting contour Γ into a collection of nearly touching oriented contours Γ_i, with turning numbers ν_i. The total turning number $\nu = \sum_i \nu_i$ is invariant against uncrossing deformations, which is another result due to Gauss [146].

All familiar 2D electron gases belong to the $|\nu| = 1$ universality class. Here we show that a thin-film Weyl semimetal with an in-plane magnetization $\boldsymbol{M}$ and broken spatial inversion symmetry can have $\nu = 0$: if the Fermi level lies in between the two Weyl points the circular Fermi surface
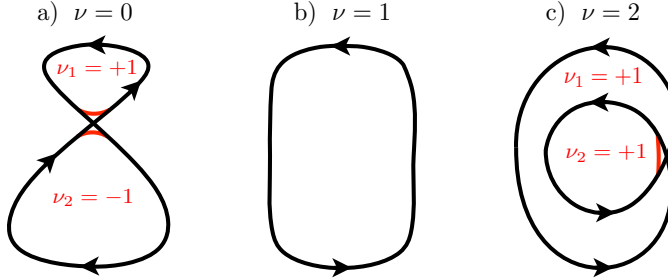
Figure 4.1: Three oriented contours (black curves) with turning number $\nu = 0, 1, 2$. The red segments show the uncrossing deformation that removes a self-intersection without changing the total turning number $\nu = \sum_i \nu_i$.

is twisted into a figure-8 with zero total curvature. To avoid misunderstanding, we emphasise that the figure-8 Fermi surface appears for Weyl fermions with the usual conical dispersion relation. We are not considering materials with a figure-8 dispersion relation, as studied in Refs. [147, 148].

The self-intersection introduced when the Fermi level passes through a Weyl point, to ensure that $|\nu| + s$ remains odd, is a crossing of Fermi arcs on the top and bottom surfaces of the thin film (width W). These have a penetration depth ξ_0 into the thin film that can be much less than the Fermi wavelength of the bulk states, so that we can be in the 2D regime of a single occupied subband [1] without appreciable overlap of the surface states [149–151]. The effect of a nonzero surface state overlap is to open up an exponentially small gap $\delta k \propto e^{-W/\xi_0}$ in the figure-8, as in Fig. 4.1a.

In a perpendicular magnetic field B the signed area enclosed by the Fermi surface is quantized in units of $2\pi/l_m^2$, with $l_m = \sqrt{\hbar/eB}$ the magnetic length. A figure-8 Fermi surface of linear dimension k_F has a signed area much smaller than k_F^2, because the upper and lower loops have opposite orientation. We find that this twisted Fermi surface produces edge states of width $k_F l_m^2$ — much wider than the usual narrow quantum Hall edge states of width l_m. The wide and the narrow edge states are counterpropagating: if the wide channel moves parallel to $\boldsymbol{M}$, the narrow channel moves antiparallel. An applied voltage selectively populates one of the two types of edge states, resulting in a conductance of e^2/h instead of $2e^2/h$ — even though there are two conducting edges.

The outline of the chapter is as follows. In the next section we formulate

---

[1] We count occupied 2D subbands by counting the number of equi-energy contours at the Fermi energy in the (k_y, k_z) plane, allowing for (nearly avoided) self-intersections. All four equi-energy contours in Fig. 4.4 correspond to a single occupied subband.

the problem, on the basis of a two-band model Hamiltonian [130, 140], and calculate the band structure in a slab geometry. The way in which the Fermi arcs reconnect with the bulk Weyl cones is described exactly by a simple transcendental equation (Weiss equation). The Fermi surface in the thin-film regime is calculated in Sec. 4.3, to show the topological transition from turning number 1 to turning number 0 when the Fermi level passes through a Weyl point. In Sec. 4.4 we calculate the edge states in a perpendicular magnetic field, by semiclassical analytics and comparison with a numerical solution. The implications of the two types of counterpropagating edge channels for electrical conduction are investigated in Sec. 4.5. We conclude with an overview of possible experimental signatures of the twisted Fermi surface.

4.2 Weyl semimetal confined to a slab

4.2.1 Two-band model

We consider the two-band model Hamiltonian of a Weyl semimetal [130, 140],

$$
\begin{aligned}
H(\boldsymbol{k}) &= t_x \sigma_x \sin k_x + t_y \sigma_y \sin k_y + m_{\boldsymbol{k}} \sigma_z + \lambda \sigma_0 \sin k_z, \\
m_{\boldsymbol{k}} &= t_z (\cos \beta - \cos k_z) + t'(2 - \cos k_x - \cos k_y).
\end{aligned}
\tag{4.2}
$$

The Pauli matrices are σ_α, $\alpha \in \{x, y, z\}$, with σ_0 the 2×2 unit matrix, acting on a hybrid of spin and orbital degrees of freedom. The momentum $\boldsymbol{k}$ varies over the Brillouin zone $|k_\alpha| < \pi$ of a simple cubic lattice (lattice constant $a_0 \equiv 1$, and we also set $\hbar \equiv 1$). The two Weyl points are at the momenta $\boldsymbol{k} = (0, 0, \pm K)$, $K \approx \beta$, and at energies $E = \pm E_0$, $E_0 \approx \lambda \sin \beta$, displaced along the k_z-axis by the magnetization $\boldsymbol{M} = \beta \hat{z}$ and displaced along the energy axis by the strain λ. Time-reversal symmetry and spatial inversion symmetry are broken by β and λ, respectively.

We take a slab geometry, unbounded in the y–z plane and confined in the x-direction between $x = 0$ and $x = W$. The magnetization along z is therefore in the plane of the slab. We impose the infinite-mass boundary condition [152] on the wave function ψ,

$$
\sigma_y \psi = \begin{cases} -\psi & \text{at} \;\; x = 0, \\ +\psi & \text{at} \;\; x = W. \end{cases}
\tag{4.3}
$$

This boundary condition corresponds to a mass term $m_0(x)\sigma_z$ in H that vanishes inside the slab and tends to $+\infty$ outside.

4.2.2 Dispersion relation

The Schrödinger equation $H\psi = E\psi$ can be solved analytically in the low-energy regime by linearizing in k_x and applying the effective mass approximation [153] $k_x \mapsto -i\partial/\partial x$. Integration of the resulting first-order differential equation in x gives

$$\psi(x) = e^{ix\Xi}\psi(0), \quad \Xi = \frac{1}{t_x}\sigma_x[E - H(0, k_y, k_z)]. \tag{4.4}$$

To ensure that an eigenstate of H satisfies the boundary condition (4.3), we require that

$$\langle -|e^{iW\Xi}|-\rangle = 0, \quad |\pm\rangle = \begin{pmatrix} 1 \\ \pm i \end{pmatrix}, \quad \sigma_y|\pm\rangle = \pm|\pm\rangle. \tag{4.5}$$

This reduces to the following dispersion relation for $E(k_y, k_z)$:

$$(E - \lambda \sin k_z)^2 - t_y^2 \sin^2 k_y - m_{\boldsymbol{k}}^2 = q^2, \tag{4.6}$$

with transverse wave number q given by

$$\frac{m_{\boldsymbol{k}}}{q} \tan(Wq/t_x) + 1 = 0. \tag{4.7}$$

In the mass term $m_{\boldsymbol{k}}$ we should set $k_x = 0$, as required by the linearization in k_x.

For imaginary $q = i\kappa t_x/W$ the transcendental equation (4.7) takes the form

$$\frac{\gamma}{\kappa} \tanh \kappa = 1, \quad \gamma = -\frac{Wm_{\boldsymbol{k}}}{t_x}, \tag{4.8}$$

which is known as the Weiss equation in the theory of ferromagnetism [154]. A unique solution with $\kappa \geq 0$ exists for $\gamma \geq 1$, given by a generalized Lambert function [2] [155]:

$$\kappa = \tfrac{1}{2}\mathcal{W}(2\gamma; -2\gamma; -1). \tag{4.9}$$

A representative band structure is shown in Fig. 4.2.

---

[2]The generalized Lambert function $\mathcal{W}(t; s; a)$ is defined as the solution of the equation $e^{\mathcal{W}}(\mathcal{W} - t) = a(\mathcal{W} - s)$.
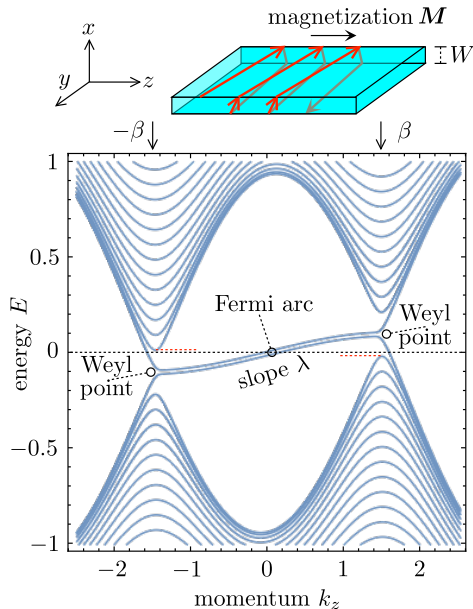
Figure 4.2: Dispersion relation $E(k_y, k_z)$ for $k_y = 0.01$ as a function of k_z, of a thick Weyl semimetal slab (width $W = 40$), calculated from Eqs. (4.6) and (4.7) for $\beta = 1.5$, $\lambda = 0.1$, $t_x = t_y = t_z = t' = 1$. The diagram at the top shows the geometry with the trajectory of an electron in a Fermi arc state spiralling along the surface with velocity $v_z = \lambda \cos k_z$ in the direction of the magnetization $\boldsymbol{M}$. The two branches of the Fermi arc visible in the dispersion relation correspond to states on the top and bottom surface of the slab (assumed to be of infinite extent in this calculation). For this thick slab the range of Fermi energies in which only a single 2D subband is occupied is very narrow (between the red dotted lines). For thinner slabs a larger energy range is available.

4.2.3 Weyl cones and Fermi arcs

In the large-W limit of a thick slab, Eq. (4.7) can be solved separately for the bulk Weyl cones and the surface Fermi arcs. We thus recover the familiar dispersion relations in the bulk and surface Brillouin zones of a Weyl semimetal [14, 116, 156, 157].

The bulk states have wave number $q \gg |m_{\boldsymbol{k}}|$, quantized by $q = (n + \frac{1}{2})\pi t_x/W$, $n = 0, 1, 2, \ldots$, with dispersion

$$E_{\text{bulk}}^{(n)} = \pm\sqrt{(n + \tfrac{1}{2})^2(\pi t_x/W)^2 + t_y^2 \sin^2 k_y + m_{\boldsymbol{k}}^2} + \lambda \sin k_z. \qquad (4.10)$$

The $\pm$ distinguishes the upper and lower halves of the Weyl cones.

The surface Fermi arcs have a purely imaginary $q = im_{\boldsymbol{k}} \Rightarrow \kappa = -\gamma$, which solves Eq. (4.8) in the large-W limit if $m_{\boldsymbol{k}} < 0$. The corresponding
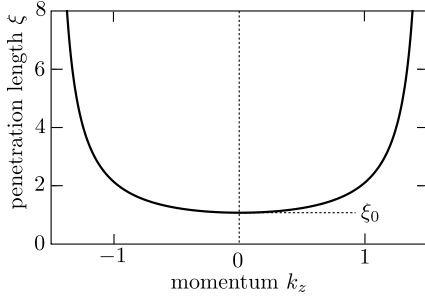
Figure 4.3: Penetration length ξ of the surface Fermi arc into the bulk Weyl semimetal, calculated via $\xi = 1/\mathrm{Im}\, q$ from the solution of the Weiss equation (4.8), for the same parameters as Fig. 4.2. The penetration length diverges at $k_z = \pm 1.475$, according to Eq. (4.13). At this critical momentum the Fermi arc merges with the bulk Weyl cones. The minimal penetration length ξ_0 is given by Eq. (4.12).

surface dispersion (4.6) is

$$E_{\mathrm{surface}} = \lambda \sin k_z \pm t_y \sin k_y, \quad |k_z| < \beta. \tag{4.11}$$

The $\pm$ sign distinguishes the Fermi arcs on opposite surfaces ($-$ at $x = 0$ and $+$ at $x = W$). The trajectory of an electron in a Fermi arc state moves chirally along the surface (see top inset in Fig. 4.2), spiralling in the direction of the magnetization $\boldsymbol{M} = \beta \hat{z}$ with velocity $v_z = \lambda \cos k_z$. The surface Fermi arc reconnects with the bulk Weyl cone near $k_z = \pm \beta$. This "Fermi level plumbing" [158] is described quantitatively by the Weiss equation (4.7), as q switches from imaginary to real at a critical k_z^{crit} for which $\gamma = 1$. The penetration length $\xi = 1/\mathrm{Im}\, q$ of the surface state into the bulk is plotted in Fig. 4.3, as a function of k_z for $k_y = 0$. Its minimal value near the center of the Brillouin zone is

$$\xi_0 = \frac{t_x}{(1 - \cos \beta) t_z}. \tag{4.12}$$

The critical wave vector $\boldsymbol{k} = (0, 0, k_z^{\mathrm{crit}})$ at which the Fermi arc terminates because its penetration length diverges is slightly smaller than the position β of the Weyl point,

$$k_z^{\mathrm{crit}} = \beta - \frac{t_x}{t_z W} + \mathcal{O}(W^{-2}). \tag{4.13}$$
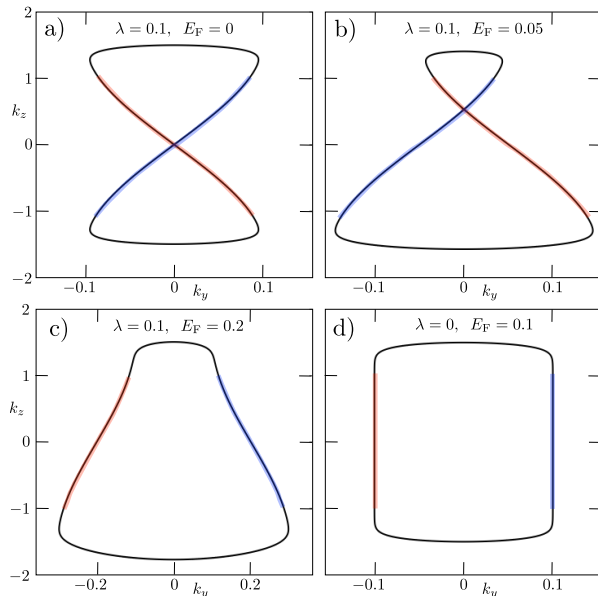
Figure 4.4: Fermi surfaces of the thin-film Weyl semimetal with a single occupied subband ($W = 15$), calculated from Eqs. (4.6) and (4.7) for $\beta = 1.5$, $t_x = t_y = t_z = t' = 1$ at different values of λ and E_{F}. The turning number $\nu = 0$ in the top row, while $\nu = 1$ in the bottom row. The figure-8 in the top row has a narrowly avoided crossing with a gap $\delta k_z = 3 \cdot 10^{-5}$ (not visible on the scale of the figure). The color of the contour indicates whether the state is localized on the top surface (red), on the bottom surface (blue), or extended through the bulk (black).

4.3 Thin-film Fermi surface

For Fermi energies

$$|E_{\text{F}}| < \frac{\pi t_x}{2W} - \lambda \sin \beta, \tag{4.14}$$

a single two-dimensional (2D) subband is occupied at the Fermi level, formed out of hybridized bulk and surface states. This two-dimensional electron gas (2DEG) regime exists for thin films of width

$$W \lesssim W_c = \frac{\pi t_x}{2\lambda \sin \beta}. \tag{4.15}$$

The Fermi surface of the 2DEG, defined by the equi-energy contour $E(k_y, k_z) = E_{\text{F}}$, is plotted in Fig. 4.4 for several parameter values.

As discussed in the introduction, the turning number ν (also known as rotation numbers, not to be confused with winding numbers) is a

topological invariant of the equi-energy contour [145]. We see from Fig. 4.4 that the Fermi surface is twisted into a figure-8 with $\nu = 0$ when the Fermi level lies between the Weyl points, $|E_{\mathrm{F}}| < \lambda \sin \beta$, while for larger Fermi energies the Fermi surface has $\nu = 1$. Because the turning number and the number of self-intersections must have opposite parity, the topological transition when E_{F} passes through a Weyl point must introduce a crossing in the Fermi surface [3].

The crossing of the equi-energy contour for small E_{F} is possible since the intersecting states are spatially separated on the top and bottom surfaces of the slab. For a finite ratio W/ξ_0 of slab width and penetration length (4.12) the crossing is narrowly avoided because of the exponentially small overlap of the states at opposite surfaces. From the Weiss equation (4.8) we calculate that the δk_z gap in the figure-8 is given by

$$\delta k_z = \frac{4t_x}{\lambda \xi_0} e^{-W/\xi_0}. \tag{4.16}$$

When $W \simeq W_c$ the gap in the figure-8 is exponentially small if $W_c \gg \xi_0$, so for

$$(1 - \cos \beta) t_z \gg \lambda \sin \beta. \tag{4.17}$$

To make contact with some of the older literature [159–161], we note that the figure-8 Fermi surface of a Weyl semimetal is essentially different from the figure-8 equi-energy contour of a conventional metal with a saddle point in the Fermi surface. In that case the figure-8 requires fine tuning of the energy to the saddle point, while here the figure-8 persists over a range of energies between two Weyl points. Moreover, the orientation of the two lobes of the figure-8 is the same in the case of a saddle point, while here it is opposite.

4.4 Quantum Hall edge channels

4.4.1 Semiclassical analysis

A magnetic field B in the x-direction, perpendicular to the thin film, introduces Landau levels in the energy spectrum: For a gauge $\boldsymbol{A} = (0, 0, By)$ the momentum k_z is still a good quantum number, we seek the dispersion $E_n(k_z)$ of the n-th Landau level.

---

[3] The turning number $\nu = 1$ universality class may also have self-intersections in the Fermi surface, but there must be a even number of them. An example with $\nu = 1$ and two crossings is Figure 4 of: Zhuo Bin Siu, Mansoor B. A. Jalil, and Seng Ghee Tan, *Dirac semimetal thin films in in-plane magnetic fields*, Sci. Rep. **6**, 34882 (2016).

Semiclassically, the n-the Landau level is determined by the quantization of the signed area $S(E) = \oint k_y dk_z$ enclosed by the oriented equi-energy contour [162],

$$l_m^2 S(E_n) = 2\pi(n + \gamma), \quad n \in \mathbb{Z}, \tag{4.18}$$

with $l_m = (\hbar/eB)^{1/2}$ the magnetic length and $\gamma \in [0, 1)$ a B-independent offset. Depending on the clockwise or anti-clockwise orientation of the contour, the enclosed area is negative or positive. Note that the signed area enclosed by the figure-8 Fermi surface of Fig. 4.4a equals zero. The phase shift $\gamma = 0$ in a bulk Weyl semimetal, when the equi-energy contour encloses a gapless Weyl point [163–166]. For the thin film the numerical data indicates $\gamma = 1/2$.

If the thin film is confined to the strip $0 < y < W_y$, with $W_y \gg l_m$, the spectrum within the strip remains dispersionless, but at the boundaries $y = 0$ and $y = W_y$ propagating states appear. In the quantum Hall effect these are chiral edge channels, moving in opposite directions on opposite edges [167, 168]. The electrical conductance of the strip, for a current flowing in the z-direction, equals the number of edge channels N moving in the same direction times the conductance quantum e^2/h.

The classical skipping orbits that form the edge channels in a magnetic field can be directly extracted from the zero-field Fermi surface: The cyclotron motion in momentum space follows the equi-energy contour $E(k_y, k_z) = E_F$ with period $2\pi m_c/eB$, where

$$m_c = \frac{1}{2\pi} \frac{d}{dE} |S(E)| \tag{4.19}$$

is the cyclotron effective mass. (The figure-8 has $m_c \approx \beta/t_y$.) Because $\boldsymbol{k} = e\dot{\boldsymbol{r}} \times \boldsymbol{B}$, the cyclotron motion in real space is obtained from the momentum space orbit by rotation over $\pi/2$ and rescaling by a factor l_m^2. Specular reflection at the edge (with conservation of k_z) then gives for the figure-8 Fermi surface the skipping orbits of Fig. 4.5. Note that these orbits are 2D projections of 3D trajectories in the thin film: The intersections that are visible in the projected orbit correspond to overpassing trajectories on the top and bottom surfaces. (See Fig. 10b of Ref. [169] for a wave packet simulation of such a trajectory.)

The real-space counterpart of the quantization rule (4.18) is that the Aharonov-Bohm phase $e \oint \boldsymbol{A} \cdot d\boldsymbol{l}$ picked up in one period of the cyclotron motion equals $2\pi(n + \gamma)$. For the skipping orbits this Bohr-Sommerfeld quantization rule still applies if the contour is closed by a segment along the edge, with an additional contribution to γ from reflection at the edge [170, 171].
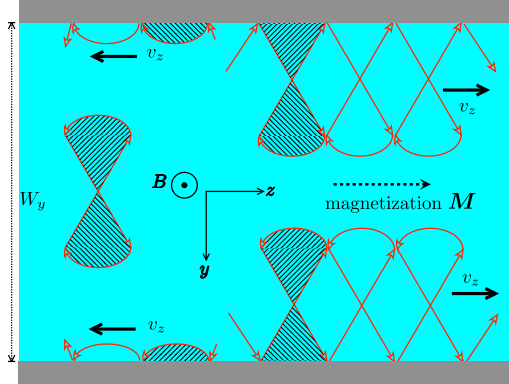
Figure 4.5: Classical cyclotron orbits corresponding to the figure-8 Fermi surface of Fig. 4.4a. Each edge supports counterpropagating skipping orbits. The corresponding quantum Hall edge channel is narrow if it propagates opposite to the magnetization, while it is wide if it propagates in the direction of the magnetization. The area enclosed by the cyclotron orbits is shaded, the direction of the shading distinguishes positive and negative contributions to the Aharonov-Bohm phase $e \oint \boldsymbol{A} \cdot d\boldsymbol{l}$.

For small n the skipping orbit should enclose a flux of the order of the flux quantum h/e, which divides the edge channels into two types, designated narrow and wide: The narrow edge channel propagates along the edge in the direction opposite to the magnetization [4]. It is tightly bound to the edge over a distance of order l_m, so that the enclosed area of order l_m^2 encloses a flux of order h/e. The wide edge channel propagates in the direction of the magnetization and extends further from the edge over a distance of order βl_m^2. It still encloses a small flux of order h/e because contributions to $\oint \boldsymbol{A} \cdot d\boldsymbol{l}$ from the two sides of the crossing point have opposite sign.

The gap δk_z at the crossing point has no effect on the quantization if $l_m \delta k_z \ll 1$, which is satisfied for $l_m \lesssim W$ when

$$(W/\xi_0)e^{-W/\xi_0} \ll \lambda/t_x. \tag{4.20}$$

Because the exponent wins it is sufficient that $W \gg \xi_0$ to ensure that the figure-8 is effectively unbroken: The field-induced tunneling through the gap then occurs with near-unit probability, so to a good approximation the wave packet propagates in an unbroken figure-8.

The presence of counterpropagating edge channels at each edge requires a Fermi energy in between the Weyl points, $|E_{\rm F}| < \lambda \sin \beta$, for a twisted

---

[4]Throughout the chapter we take β and λ positive. The direction of motion of the edge channels indicated in Fig. 4.5 should be inverted if either β or λ change sign.
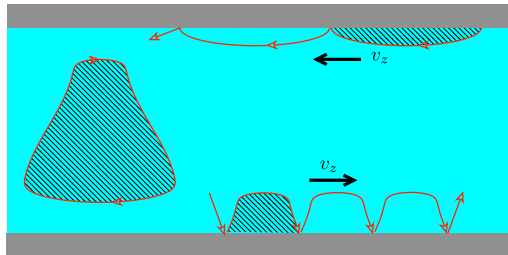
Figure 4.6: Same as Fig. 4.5, but now for the Fermi surface of Fig. 4.4c, without a self-intersection. The equi-energy contour has a single orientation, indicated by the single direction of the shading. The edge states are chiral, propagating in opposite directions on opposite edges.

Fermi surface. When the Fermi surface is a simple contour without self-intersections the edge channels are chiral, propagating in opposite directions on opposite edges as in Fig. 4.6.

4.4.2 Numerical simulation

To go beyond the semiclassical analysis we have diagonalized the model Hamiltonian (4.2) numerically, using the *Kwant* tight-binding code [142]. Fig. 4.7a shows the dispersion relation with four edge states at $E_\mathrm{F} = 0$, two counterpropagating at each edge. The corresponding density profile for each edge state is shown in Fig. 4.7b. The two types of edge channels, one wide and the other narrow, are clearly visible.

In Fig. 4.8 we show the Landau levels in an infinite system as a function of the flux Φ through a unit cell. The Landau fan is fitted to

$$\frac{\hbar}{e\Phi}S_E = 2\pi(n + \gamma),\qquad(4.21)$$

corresponding to the semiclassical formula (4.18). The resulting offset γ is consistent with $\gamma = 1/2$. We checked that the fitted value of S_E is close (within 2%) of the signed area enclosed by the figure-8 equienergy contour. We also checked that the same $\gamma = 1/2$ is obtained when the equienergy contour is a slightly deformed circle, rather than a figure-8.

4.5 Magnetoconductance

To determine the magnetotransport through the Weyl semimetal strip we connect it at both ends $z = 0$ and $z = L$ to a metal reservoir. Following a
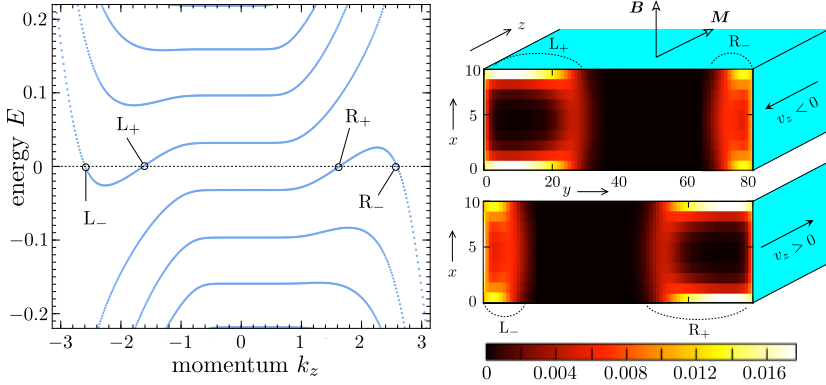
Figure 4.7: Left: Dispersion of a thin-film Weyl semimetal strip ($W = 10$, $W_y = 80$) in a perpendicular magnetic field ($l_m = 4.5$), calculated numerically from the tight-binding Hamiltonian (4.2). The material parameters are $\beta = 1.05$, $\lambda = 0.2$, $t_x = t_y = t_z = t' = 1$. At $E_F = 0$ this system has the figure-8 Fermi surface of Fig. 4.4a. The letters indicate the counterpropagating edge channels, $L_\pm$ at one edge and $R_\pm$ at the opposite edge. Right: Probability density $|\psi(x, y)|^2$ for the four edge states at $E = 0$. The density is translationally invariant in the z-direction, the color plots show a cross section in the x–y plane (separated in two panels for clarity). Each edge has a counterpropagating pair of edge states, one with $v_z < 0$ tightly bound to the edge (width $\approx l_m = 4.5$), the other with $v_z > 0$ penetrating more deeply into the bulk (width $\approx \beta l_m^2 = 21$).

similar approach used for graphene [172], it is convenient to take the same model Hamiltonian (4.2) throughout the system, with the addition of a z-dependent chemical potential term $-\mu(z)\sigma_0$. (Physically, this potential could be controlled by a gate voltage.) We set $\mu(z) = 0$ in the semimetal region $0 < z < L$ and take $\mu(z) \gg E_0$ in the metal reservoirs ($x < 0$ and $x > L$). This corresponds to n-type doping of the reservoir. (For p-type doping we would take $\mu(z) \ll -E_0$.)

We distinguish n-type and p-type edge channels in the Weyl semimetal depending on whether they reconnect at large $|E|$ with the upper Weyl cones (n-type) or with the lower Weyl cones (p-type). Referring to the dispersion of Fig. 4.7a, the channels $L_\pm$ at the $y = 0$ edge are n-type, while the channels $R_\pm$ at the $y = W_y$ edge are p-type. The distinction is important, because only the n-type edge channels can be transmitted into the n-type reservoirs. As indicated in Fig. 4.9, the p-type channels are confined to the semimetal region, without entering into the reservoirs.

Upon application of a bias voltage V between the two n-type reservoirs
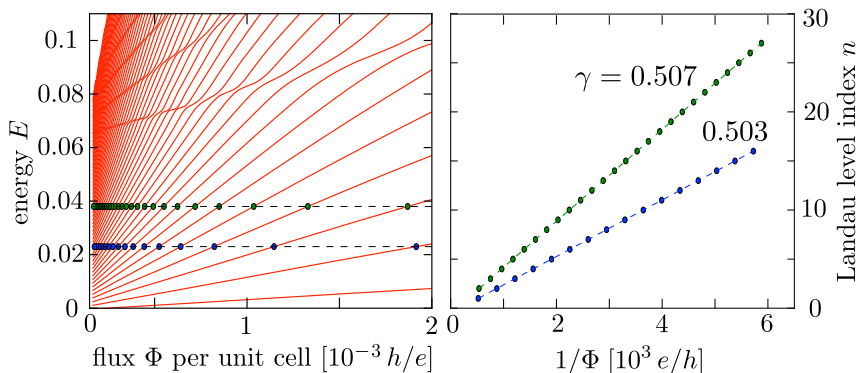
Figure 4.8: Left panel: Sequence of Landau level energies $E_n(B)$ as a function of magnetic field; levels at two values of the energy are marked by colored dots. Right panel: Landau level index n for these two energies as a function of inverse magnetic field. This "Landau fan" is fitted to Eq. (4.21) to obtain the offset γ. The data is calculated numerically from the Weyl semimetal tight-binding model in an unbounded thin film (thickness $W = 30$), for parameters $\beta = 1.05$, $\lambda = 0.1$, $t_x = t_y = t_z = t' = 1$.

a current I will flow along the n-type edge, with a conductance

$$G = I/V = \frac{e^2}{h} T_{y=0} \tag{4.22}$$

determined by the backscattering probability $T_{y=0}$ along the edge at $y = 0$, so $G = e^2/h$ without impurity scattering — see Fig. 4.10.

This is not the usual edge conduction of the quantum Hall effect: As shown in Fig. 4.11, the current flows along the *same* edge when we change the sign of the voltage bias (switching source and drain), while in the quantum Hall effect the current switches between the edges when V changes sign. The only way to switch the edge here is to change the sign of the magnetic field, so that the n-type edge is at $y = W_y$ rather than at $y = 0$.

4.6 Discussion

We have discussed the unusual magnetic response of a two-dimensional electron gas with a twisted Fermi surface. The topological transition from turning number $\nu = 1$ (the usual deformed Fermi circle) to turning number $\nu = 0$ (the figure-8 Fermi surface) happens when the Fermi level passes through the Weyl point of a thin-film Weyl semimetal with an in-plane magnetization and broken spatial inversion symmetry. We discuss several
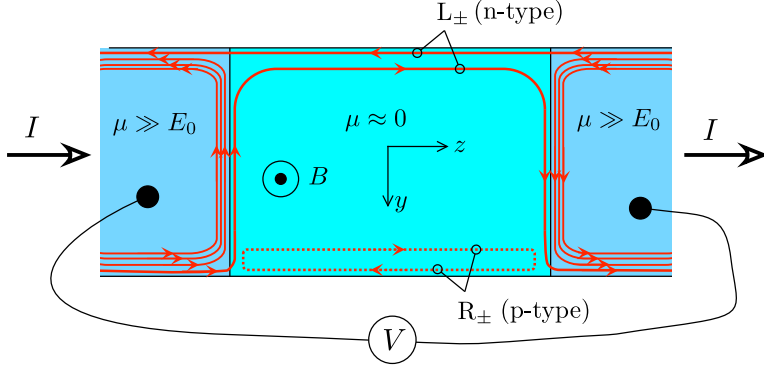
Figure 4.9: Undoped Weyl semimetal (chemical potential $\mu \approx 0$) connected to heavily doped metal reservoirs ($\mu \gg E_0$ for n-type doping). Edge channels in a perpendicular magnetic field are shown in red, with arrows indicating the direction of propagation. The $L_\pm$ edge channels are n-type and can enter into the reservoirs, while the $R_\pm$ edge channels are p-type and remain confined to the semimetal region (dotted lines). The current I flows along the n-type edge in the semimetal, irrespective of the sign of the applied voltage V.

transport properties that could serve as signatures for the topological transition from $\nu = 1$ to $\nu = 0$.

In a magnetic field the figure-8 Fermi surface supports counterpropagating edge channels, see Fig. 4.9. At $E_F = 0$, with an equal number of left-movers and right-movers at each edge, the Hall resistance will vanish. This is the first magnetotransport signature. If we vary the Fermi level and enter the regime of chiral edge channels, we should see the appearance of a voltage difference between the edges in response to a current flowing along the edges.

The second signature is the edge-selectivity: although both edges support counterpropagating states, the current flows entirely along one of the two edges, determined by the direction of $\boldsymbol{M} \times \boldsymbol{B}$. This edge-selective current flow might be detected directly, or indirectly by introducing disorder on one edge only and measuring a difference between the conductance G for positive and negative B. Note that $G(B) \neq G(-B)$ does not violate Onsager reciprocity, since for that we would need to change the sign of both magnetic field $\boldsymbol{B}$ and magnetization $\boldsymbol{M}$.

A third signature is in the cyclotron resonance condition for the optical conductivity $\boldsymbol{\sigma}$. As explained by Koshino [173] in the context of a type-II Weyl semimetal (which has a figure-8 cyclotron orbit at a specific energy where electron and hole pockets touch [81]), the resonance frequency is twice as small for an electric field oriented along the long axis of the figure-8, than it is for an electric field oriented along the short axis. In the
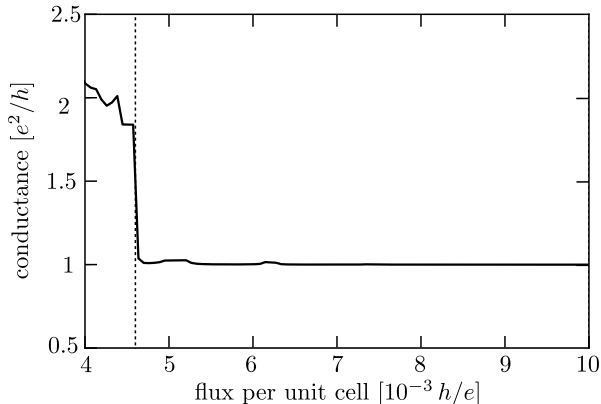
Figure 4.10: Conductance in the geometry of Fig. 4.11 as a function of magnetic field. (The magnetic length $l_m = 4$ of Fig. 4.11 corresponds to a flux per unit cell of $0.01\,h/e$.) The regime of a single pair of counterpropagating edge channels is reached to the right of the vertical dotted line. The conductance in this regime is e^2/h rather than $2e^2/h$, because only one edge is coupled to the electron reservoirs.

geometry of Fig. 4.5, the resonance frequency equals eB/m_c for σ_{yy} and $2eB/m_c$ for σ_{zz}.

In our analysis we have not included disorder effects. The counterpropagating edge channels can be coupled by disorder, and this would reduce the conductance below the quantized value of $G = e^2/h$ seen in Fig. 4.10. There is no symmetry to protect this quantization, like there is for the helical edge channels in the quantum spin Hall effect, but there is a spatial separation of wide and narrow edge channels (see Fig. 4.7b), which may provide some robustness against backscattering by disorder.

We have focused here on Fermi surfaces with turning number $\nu = 0$ and $\nu = 1$. It would be of interest to compare with other values of ν. A model Hamiltonian for $\nu = 2$, that could be a starting point for such a study, is given in the Appendix.

4.7 Appendix. Effective 2D Hamiltonian

We derive an effective Hamiltonian for the thin-film Weyl semimetal. Starting from the full Hamiltonian (4.2), we discretize the x-direction by the substitution

$$
\begin{aligned}
\cos k_x &\mapsto \tfrac{1}{2}\big(\delta_{i,j-1} + \delta_{i,j+1}\big),\\
\sin k_x &\mapsto -\tfrac{1}{2}i\big(\delta_{i,j-1} - \delta_{i,j+1}\big).
\end{aligned}
\tag{4.23}
$$
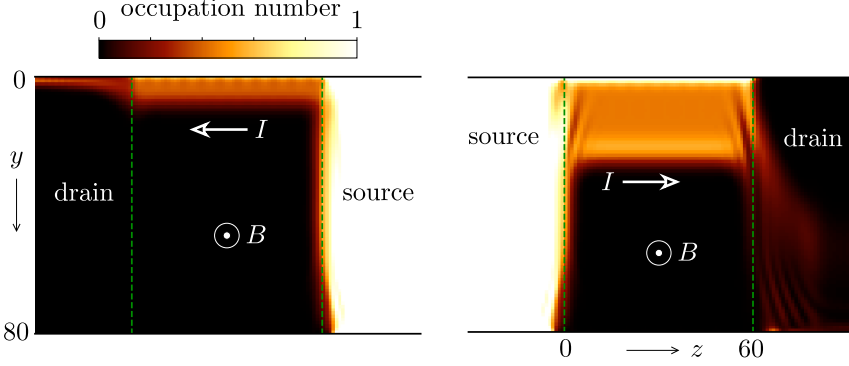
Figure 4.11: Color-scale plot in the y–z plane of the occupation numbers of current-carrying states at the Fermi level, in response to a voltage bias between source and drain. The data is calculated numerically from the tight-binding Hamiltonian (4.2) in the geometry of Fig. 4.9 (parameters $\beta = 1.05$, $\lambda = 0.25$, $t_x = t_y = t_z = t' = 1$, $W = 10$, $l_m = 4$). The chemical potential is $\mu = 0$ in the Weyl semimetal region (between green lines, from $z = 0$ to $z = 60$), while $\mu = 0.75$ in the metal reservoirs ($z < 0$ and $z > 60$). The current keeps flowing along the same edge when source and drain are switched, carried either by a narrow edge channel (left panel) or by a wide edge channel (right panel). The opposite edge is fully decoupled from the reservoirs.

The Kronecker δ_{ij} is set to zero if either layer index i or j is outside of the set $\{1, 2, \dots, W\}$, corresponding to hard-wall boundary conditions at the top and bottom layer. Substitution in Eq. (4.2) leads to

$$H_{ij} = \delta_{ij}\big[\sigma_y \sin k_y + M_{\boldsymbol{k}}\sigma_z\big] - \tfrac{1}{2}\delta_{i,j-1}\big(\sigma_z + i\sigma_x\big)$$
$$- \tfrac{1}{2}\delta_{i,j+1}\big(\sigma_z - i\sigma_x\big) + \delta_{ij}\lambda\,\sigma_0 \sin k_z, \tag{4.24}$$

$$M_{\boldsymbol{k}} = 2 + \cos\beta - \cos k_z - \cos k_y. \tag{4.25}$$

For simplicity we have set $t_x = t_y = t' \equiv 1$. Since the λ term is a scalar, we can set it to zero for now and then add it at the end of the calculation.

After the unitary transformation $H \mapsto U^\dagger H U$ with $U = e^{i\pi\sigma_z/4}e^{i\pi\sigma_y/4}$ we have

$$H_{ij} = \delta_{ij}\big[\sigma_z \sin k_y + M_{\boldsymbol{k}}\sigma_x\big] - \tfrac{1}{2}\delta_{i,j-1}\big(\sigma_x + i\sigma_y\big)$$
$$- \tfrac{1}{2}\delta_{i,j+1}\big(\sigma_x - i\sigma_y\big). \tag{4.26}$$

The square H^2 is block-diagonal in the σ index,

$$(H^2)_{ij} = \delta_{ij}\sigma_0 \sin^2 k_y + \begin{pmatrix} Z_{ij} & 0 \\ 0 & Z'_{ij} \end{pmatrix}, \tag{4.27a}$$

$$Z_{ij} = (M_{\boldsymbol{k}}^2 + 1 - \delta_{iW})\delta_{ij} - M_{\boldsymbol{k}}(\delta_{i,j-1} + \delta_{i,j+1}), \tag{4.27b}$$

$$Z'_{ij} = (M_{\boldsymbol{k}}^2 + 1 - \delta_{i1})\delta_{ij} - M_{\boldsymbol{k}}(\delta_{i,j-1} + \delta_{i,j+1}). \tag{4.27c}$$
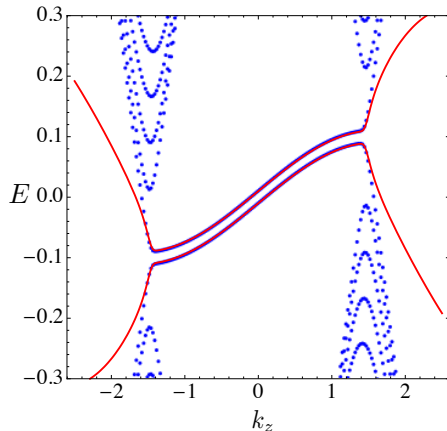
Figure 4.12: Dispersion relation at $k_y = 0.01$ given by the effective Hamiltonian (4.31) (red curve), compared to numerical results from the full Hamiltonian (4.2) (blue dots). The parameters are the same as in Fig. 4.2.

The two $W \times W$ matrices Z and Z' have the same eigenvalues ζ, given by

$$\mathrm{Det}\,(Z - \zeta) = (\mathrm{Det}\,Z)\left[1 - \zeta\,\mathrm{Tr}\,Z^{-1} + \mathcal{O}(\zeta^2)\right] = 0. \tag{4.28}$$

The low-energy spectrum is therefore given

$$E^2 = \sin^2 k_y + \zeta_0, \ \ \zeta_0 = \frac{1}{\mathrm{Tr}\,Z^{-1}} \ll 1, \tag{4.29}$$

which evaluates to

$$\begin{aligned}
\zeta_0 &= \frac{M_{\boldsymbol{k}}^{2W}}{1 + 2M_{\boldsymbol{k}}^2 + 3M_{\boldsymbol{k}}^4 + 4M_{\boldsymbol{k}}^6 + \cdots + W M_{\boldsymbol{k}}^{2W-2}} \\
&= \frac{M_{\boldsymbol{k}}^{2W}\left(1 - M_{\boldsymbol{k}}^2\right)^2}{1 - M_{\boldsymbol{k}}^{2W}\left[1 + \left(1 - M_{\boldsymbol{k}}^2\right)W\right]}.
\end{aligned} \tag{4.30}$$

For $M_{\boldsymbol{k}} \ll 1$ we have simply $\zeta_0 \approx M_{\boldsymbol{k}}^{2W}$.

The corresponding effective low-energy Hamiltonian takes the form

$$H_{\mathrm{eff}} = \sigma_x\sqrt{\zeta_0} + \sigma_y \sin k_y + \lambda\sigma_0 \sin k_z, \tag{4.31}$$

where we have reinsterted the λ term. A comparison of the energy spectrum of the effective Hamiltonian with the result from an exact numerical diagonalization of the full Hamiltonian is shown in Fig. 4.12.
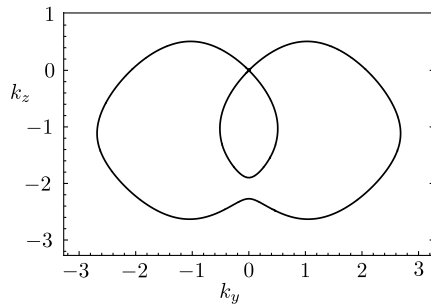
Figure 4.13: Fermi surface at $E = 0$ with turning number $\nu = 2$ given by the Hamiltonian (4.32), for the parameters $W = 40$, $\beta = 1.5$, $\lambda = 1$, $\mu = 0.6$.

In closing, we note that a simple modification of this effective 2D Hamiltonian can be used to describe Fermi surfaces with turning number greater than unity. As an example, the Hamiltonian

$$\tilde{H}_{\text{eff}} = H_{\text{eff}} + \mu \left(2 - \cos k_z - \cos k_y\right)\sigma_0 \tag{4.32}$$

has the $\nu = 2$ Fermi surface shown in Fig. 4.13.

5 Phase shift of cyclotron orbits at type–I and type–II multi–Weyl nodes

5.1 Introduction

Electrons moving along cyclotron orbits in a homogeneous magnetic field are subject to the quantization condition [161]

$$l^2 S = 2\pi(m + \gamma), \quad m \in \mathbb{Z}, \tag{5.1}$$

where S is the zero-field area enclosed by the cyclotron orbit in momentum space, $l = \sqrt{\hbar/eB}$ is the magnetic length, and the offset γ includes quantum corrections, which can be expanded in powers of the magnetic field B [174]. In the semiclassical regime when the magnetic length is much larger than the Fermi wavelength, field-dependent corrections to γ are suppressed and the remaining number of zeroth order in B encodes valuable information about the electronic properties of the system. In particular, the offset includes contributions coming from topological features in the band structure [163–165], which makes it the subject of high current interest. Experimentally it can be deduced from quantum oscillations in the de Haas-van Alphen or the Shubnikov-de Haas effects, widely used nowadays to identify Weyl, Dirac, and nodal-line semimetals [175–179].

Interestingly, in some well-studied systems the offset measures the topological features independent of the specifics of the band structure. So, e.g., in graphene and graphene bilayer exposed to an out-of-plane magnetic field the offset turns out to be given by a winding number—the number of full turns made by the direction of the electron's pseudospin degree of freedom during a single turn around the cyclotron orbit [164]. This integer winding number is a robust feature, determined by the type of the band touching, and is sometimes called the topological charge of the Weyl or Dirac fermion [180]. In contrast to the common belief, however, the topological charge contributes to the offset in such a robust manner only in exceptional cases, namely when particular symmetry constraints are
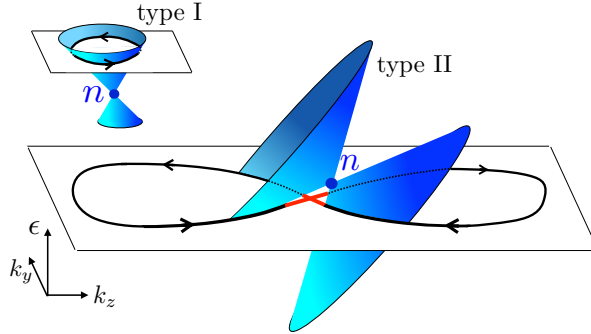
Figure 5.1: Schematic illustration of a breakthrough cyclotron orbit (figure-8 curve) at a type-II Weyl node with topological charge n. The red part indicates quantum tunneling in the magnetic-breakthrough region. The inset shows a cyclotron orbit at a type-I Weyl node.

satisfied [165]. In general, the offset is sensitive also to other parameters of the band touching and it is the aim of this work to characterize this sensitivity.

One important parameter is a linear tilt of the dispersion at the Weyl node, which is generically present in material realizations and, most importantly, leads to the occurrence of two types of Weyl nodes, as sketched in Fig. 5.1. Upon the type-I to type-II transition, the tilt exceeds a critical value, above which an equi-energy surface near the node cuts both bands [58]. The closed cyclotron orbit at a type-I Weyl node is thereby replaced by two open branches, which can be closed at large momenta by higher-order corrections to the Weyl Hamiltonian, resulting in two cyclotron orbits, one electron-like and one hole-like. Band details determine a critical magnetic field, above which the two separate cyclotron orbits effectively merge into a single orbit via magnetic breakthrough [181, 182]. This critical field is zero if the energy and the parallel momentum are exactly at the node where the two contours touch [81, 166], and is larger than zero if the gap between the contours is finite. The magnetic breakdown contributes an additional phase to the offset γ, so one would expect that the offset is even more sensitive to details of the orbit than in the case without magnetic breakdown.

In this work we analyze the offset for orbits at both types of Weyl nodes and find characteristic dependence of γ on the Weyl-node parameters. Most surprisingly, the offset of the breakthrough orbit at a type-II Weyl point turns out to depend only on the topological charge. This striking result is based on two facts, the universality of the phase jump of π acquired in

the magnetic-breakthrough region and a robust phase shift of $n\pi$ induced by the topological charge. The insensitivity of the latter on details of the orbit comes from a cancellation of a non-universal part of the phase in the two loops of the breakthrough orbit, which are traversed in opposite directions.

5.2 Model

We consider a set of Hamiltonians that govern the physics close to topologically distinct band touchings,

$$H_0 = k_-\sigma_+ + k_+\sigma_- + u\,k_z\sigma_0, \tag{5.2a}$$
$$H_n = k_-^n\sigma_+ + k_+^n\sigma_- + u\,k_z\sigma_0 + k_z\sigma_z,\ n \in \{1, 2, \dots\}, \tag{5.2b}$$

where $k_\pm = k_x \pm ik_y$, $(k_x, k_y, k_z) = \mathbf{k}$ are momenta (scaled by velocities), $\sigma_\pm = \sigma_x \pm i\sigma_y$, $\sigma_{x,y,z}$ are Pauli matrices, and σ_0 the identity matrix. The band touching at $\mathbf{k} = 0$ described by H_n corresponds to a topologically protected multi-Weyl node of order n [59], while H_0 describes a trivial, non-protected band touching (a gap is produced by a perturbation $\propto \sigma_z$). The parameter $u > 0$ controls the tilt of the Weyl cone; for $u < 1$ and $u > 1$ the Weyl cone is of type I and II, respectively.

The magnetic field pointing in x direction moves the particles along equi-energy contours $k_z(k_y)$ at fixed energy ϵ and parallel momentum component k_x. The contours are determined by the Schrödinger equation

$$H_n|u_{n\pm}\rangle = \epsilon|u_{n\pm}\rangle, \tag{5.3}$$

where $\pm$ denote the two bands.

In the quantization condition (5.1) one can distinguish three phase shifts that contribute to the offset

$$\gamma = \frac{1}{2\pi}(\phi_0 + \phi_b + \phi_t). \tag{5.4}$$

Here ϕ_0 and ϕ_b are phase shifts that occur at singular points on the orbit. Specifically, turning points give rise to the Maslov phase ϕ_0 [183], in which each turning point contributes a phase jump of $\pm\pi/2$, the sign determined by the sign of the curvature at the turning point. In particular one finds that $\phi_0 = \pi$ and $\phi_0 = 0$ for orbits that can be deformed into a circle and into an 8-shape, respectively. With ϕ_b we denote the phase shifts that occur due to magnetic breakdown. Finally, ϕ_t is the topological phase shift, which includes the Berry phase accumulated during a full turn around the

orbit and the effect of the orbital magnetic moment [163–165, 184]. The explicit calculation of ϕ_{b} and ϕ_{t} is the main result of this work, which will be presented in the following.

5.3 Topological phase shift

The topological phase shift of a closed contour at energy ϵ and the fixed momentum component k_x is given by [164, 185]

$$\phi_{\mathrm{t}} = \oint dk_y' \left[A - \frac{dk_z(k_y')}{d\epsilon} M \right]. \tag{5.5}$$

Here the first term is determined by the Berry connection projected onto the contour,

$$A = i\langle u|\nabla_{\mathbf{k}}|u\rangle \cdot \frac{d\mathbf{k}}{dk_y} = i\langle u|\frac{d}{dk_y}|u\rangle, \tag{5.6}$$

which contributes to ϕ_{t} the usual Berry phase of the closed orbit. The second term is the correction to the zero-field area S coming from the orbital magnetic moment projected onto the direction of the magnetic field [184],

$$M = \frac{i}{2}\Big[\big(\partial_{k_y}\langle u|\big)\big(\epsilon - H\big)\big(\partial_{k_z}|u\rangle\big)$$
$$- \big(\partial_{k_z}\langle u|\big)\big(\epsilon - H\big)\big(\partial_{k_y}|u\rangle\big)\Big]. \tag{5.7}$$

The eigenfunctions of the Hamiltonian H_i can be written as

$$|u_{0\pm}\rangle = \frac{1}{\sqrt{2}} \begin{pmatrix} \mp e^{-i\alpha} \\ 1 \end{pmatrix},$$

$$|u_{n+}\rangle = \begin{pmatrix} -\sin\frac{\beta}{2}e^{-in\alpha} \\ \cos\frac{\beta}{2} \end{pmatrix}, \quad |u_{n-}\rangle = \begin{pmatrix} \cos\frac{\beta}{2}e^{-in\alpha} \\ \sin\frac{\beta}{2} \end{pmatrix}, \tag{5.8}$$

where the angles α and β are defined as

$$\cos\beta = \frac{k_z}{k}, \quad \sin\beta = \frac{\left(k_x^2 + k_y^2\right)^{\frac{n}{2}}}{k},$$

$$\alpha = \mathrm{Arg}(k_x + ik_y), \quad k = \sqrt{\left(k_x^2 + k_y^2\right)^n + k_z^2}. \tag{5.9}$$

For the topologically trivial case we obtain from (5.6)–(5.9)

$$A_{0\pm} = \frac{k_x}{2(k_x^2 + k_y^2)}, \quad M_{0\pm} = 0, \tag{5.10}$$

and the topological phase shift vanishes as it should,

$$\phi_{\mathrm{t}}^{\pm} = \oint dk_y' \, A_{0\pm} = \oint dk_y' \frac{k_x}{2[k_x^2 + (k_y')^2]} = 0 \quad (n = 0), \tag{5.11}$$

independent of the integration contour. For the non-trivial case, we obtain

$$A_{n\pm} = \frac{n k_x \left(k_x^2 + k_y^2\right)^{n-1}}{2k(k \pm k_z)}, \quad M_{n\pm} = -\frac{n k_x \left(k_x^2 + k_y^2\right)^{n-1}}{2k^2}. \tag{5.12}$$

To calculate the topological phase shift, we consider the explicit expression for the equi-energy contours, which is derived from (5.3) in the form

$$k_z^{\pm}(k_y) = \frac{\epsilon \, u \pm \sqrt{(u^2 - 1)\left(k_x^2 + k_y^2\right)^n + \epsilon^2}}{u^2 - 1}. \tag{5.13}$$

For $u > 1$, the contours given by $k_z^{\pm}(k_y)$ are disjoint and we need to introduce an additional orbit segment that connects the two open ends of $k_z^{\pm}(k_y)$ at $k_z \to \pm\infty$. These connecting segment can be realized by an additional mass term $\eta k_z^3 \sigma_z$ in the Hamiltonian, with an infinitesimal $\eta > 0$. The reconnection then occurs at large momenta k_z, with $|k_z| > (u-1)/\eta \to \infty$. In the expressions (5.12) for A and M the additional mass term replaces $k_z \to k_z + \eta k_z^3$. On the connecting segment, A and M go to zero like η^2, while the integration along the connecting segment gives a factor of order $1/\eta$. Hence the contribution of the connecting segment to ϕ_{t} vanishes and the integration reduces to the integration along the main contour $k_z^{\pm}(k_y)$.

Inserting (5.12) and (5.13) into (5.5) we obtain

$$\phi_{\mathrm{t}}^{\pm} = \mp \int dk_y' \frac{(u+1)n k_x \left(k_x^2 + (k_y')^2\right)^{n-1}}{2\left[k^{\pm} \pm k_z^{\pm}\right]\left[k_z^{\pm} \mp u k^{\pm}\right]}. \tag{5.14}$$

For a type-II cone ($u > 1$) we use the substitution $\kappa = k_y'/k_x$ and obtain

$$\phi_{\mathrm{t}}^{\pm} = \int_{-\infty}^{\infty} d\kappa \frac{n(\kappa^2 + 1)^{n-1}}{2\sqrt{(\kappa^2 + 1)^n + \cot^2 \theta}}$$

$$\times \left(\sqrt{(\kappa^2 + 1)^n + \cot^2 \theta} \pm \cot \theta\right)^{-1}, \tag{5.15}$$

where the parameter θ encoding contour details is defined as

$$
\theta = \begin{cases} \operatorname{atan}\left(\frac{k_x^n \sqrt{u^2-1}}{\epsilon}\right) & u > 1 \\ \operatorname{atanh}\left(\frac{k_x^n \sqrt{1-u^2}}{\epsilon}\right) & u < 1. \end{cases} \tag{5.16}
$$

The integral in (5.15) needs to be calculated numerically (see below); for the special case $n = 1$, we find the closed-form solution

$$
\phi_t^{\pm} = \frac{\pi}{2}(1 \mp \operatorname{sign}\theta) \pm \theta \qquad (n=1). \tag{5.17}
$$

While $\phi_t^{\pm}$ are the topological phase shifts of the two (electron/hole) orbits $k_z^{\pm}(k_y)$, the sum $\phi_t^+ + \phi_t^- \equiv \phi_t^{\mathrm{br}}$ is the topological phase shift of the breakthrough orbit, i.e., the figure-of-8 orbit that encloses both the electron and the hole pocket. Using the substitution $z = (\kappa^2 + 1)^n$ the integral for ϕ_t^{br} simplifies to

$$
\phi_t^{\mathrm{br}} = \int_1^{\infty} dz \frac{1}{\sqrt{z^{\frac{2n+1}{n}} - z^2}} = n\pi, \tag{5.18}
$$

where the θ dependent part cancels out. As a result the topological phase shift of the figure-of-8 orbit only depends on the quantized topological charge n, in contrast to the θ-dependent phase shifts of the separate orbits.

For type-I Weyl fermions ($u < 1$) $k_z^{\pm}$ are two parts of a single closed contour, which topological phase is denoted ϕ_t. A closed-form solution for the integral (5.14) is found for $n = 1$,

$$
\phi_t = \pi \operatorname{sign}\theta \qquad (n=1), \tag{5.19}
$$

in agreement with Refs. [164, 186–188]. For $n \geq 2$, we find in the limits $\theta \to 0^{\pm}$ and $\theta \to \pm\infty$,

$$
\phi_t \xrightarrow{\theta \to 0^{\pm}} n\,\pi\,\operatorname{sign}\theta, \quad \phi_t \xrightarrow{\theta \to \pm\infty} \sqrt{n}\,\pi\,\operatorname{sign}\theta. \tag{5.20}
$$

The full θ dependence will be discussed below.

5.4 Breakthrough phase shift

To calculate the additional phase shift of the figure-of-8 orbit due to magnetic breakdown, we follow a standard route [182] and calculate the

scattering matrix that relates the exact wavefunction of the magnetic-breakdown region with the in- and out-going semiclassical wavefunctions.

We start with the non-topological Hamiltonian H_0. Introducing the magnetic field via Peierls substitution $k_z \mapsto k_z + il^{-2}\partial_{k_y}$, followed by a unitary transformation,

$$\tilde{H}_0 = e^{-il^2(k_z - \epsilon/u)k_y} H_0 e^{il^2(k_z - \epsilon/u)k_y}, \tag{5.21}$$

we arrive at

$$\tilde{H}_0 = k_x \sigma_x + k_y \sigma_y + i\, u\, l^{-2} \partial_{k_y} \sigma_0 + \epsilon. \tag{5.22}$$

Rescaling the variables as $k = lk_y/\sqrt{u}$, $\delta_0 = lk_x/\sqrt{u}$, the Schrödinger equation $\tilde{H}_0 \psi = \epsilon\psi$ reads

$$\left[\sigma_x \delta_0 + \sigma_y k + i\partial_k\right]\psi = 0. \tag{5.23}$$

The exact solution of (5.23) is known from the Landau-Zener problem [189]. To obtain the phase shift in comparison to the semiclassical solution of (5.23), the exact wavefunctions are matched with the incoming semiclassical wavefunctions at $k \ll -\delta_0$, denoted $\psi_i^{\pm}$, and outgoing $\psi_f^{\pm}$ at $k \gg \delta_0$. From this standard procedure (recapitulated in Sec. 5.7) we obtain the scattering matrix S that relates the final state in the basis (ψ_f^+, ψ_f^-) to the incoming state in the basis (ψ_i^+, ψ_i^-),

$$S = \begin{pmatrix} \sqrt{1-W}\, e^{i\alpha} & -i\sqrt{W} \\ -i\sqrt{W} & \sqrt{1-W}\, e^{-i\alpha} \end{pmatrix}, \tag{5.24}$$

where

$$W = e^{-\pi\delta_0^2}, \quad \alpha = \frac{\pi}{4} + \frac{\delta_0^2}{2} - \frac{\delta_0^2}{2}\ln\frac{\delta_0^2}{2} + \arg\Gamma\left(i\frac{\delta_0^2}{2}\right). \tag{5.25}$$

The breakthrough orbit dominates if $\delta_0 \ll 1$, $W \approx 1$, in which case each band transition in the breakthrough region contributes a phase jump of $\pi/2$ giving in total the phase shift $\phi_{\mathrm{b}} = \pi$ for the breakthrough orbit.

For the topological case, we linearize the Hamiltonian H_n in k_y, leading to

$$H_n' = k_x^n \sigma_x + nk_x^{n-1} k_y \sigma_y + k_z \sigma_z + uk_z. \tag{5.26}$$

After Peierls substitution we apply the unitary transformation given by

$$\tilde{H}_n = e^{-il^2[k_z - \epsilon/(u^2-1)]k_y} H_n' e^{il^2[k_z - \epsilon/(u^2-1)]k_y}. \tag{5.27}$$

Rescaling and transforming the variables as

$$k = lk_y(u^2-1)^{-1/4}\sqrt{nk_x^{n-1}}, \tag{5.28a}$$

$$\delta_n = l\,\mathrm{sign}(\epsilon)\frac{\sqrt{\epsilon^2 + (u^2-1)k_x^{2n}}}{(u^2-1)^{3/4}k_x^{(n-1)/2}}, \tag{5.28b}$$
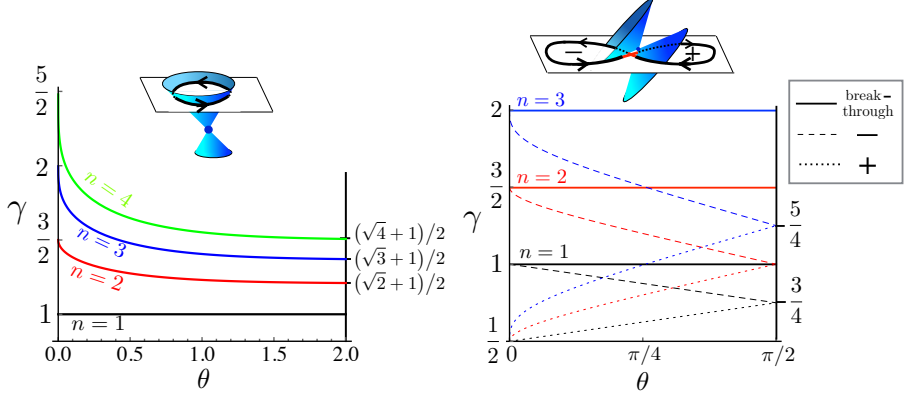
Figure 5.2: a) Parameter dependence of the offset γ of orbits at a type-I Weyl node. b) Parameter dependence of the offset γ of orbits at a type-II Weyl node. The offsets of separate orbits k_z^+ and k_z^- (without magnetic breakthrough) depend on the band parameter θ, while the offset of the figure-8 breakthrough orbit only depends on the topological charge n.

we obtain the Schrödinger equation

$$\Big[\delta_n\sqrt{u^2-1}\sin\theta\,\sigma_x + k\sqrt{u^2-1}\,\sigma_y$$
$$+ i\partial_k(u+\sigma_z) + \delta_n\cos\theta(1+u\sigma_z)\Big]\psi = 0. \tag{5.29}$$

Multiplying (5.29) from the left with $\mathcal{M} = \mathrm{diag}[(u+1)^{-1},(u-1)^{-1}]$ and applying a transformation given by

$$T = -i\begin{pmatrix} \frac{1-u}{\sqrt{u^2-1}} & \frac{u-1}{\sqrt{u^2-1}} \\ 1 & 1 \end{pmatrix}\sigma_z e^{-i\sigma_y\theta/2}, \tag{5.30}$$

we again arrive at the differential equation of the Landau-Zener form (5.23),

$$\hat{H}\hat{\psi}(k) = \big(\delta_n\,\sigma_x + k\,\sigma_y + i\partial_k\big)\hat{\psi}(k) = 0, \tag{5.31}$$

where $\hat{\psi}(k) = T^{-1}\psi(k)$ and $\hat{H} = T^{-1}\mathcal{M}\,\tilde{H}T$. The solution of (5.29) is thus given by the solution of the Landau-Zener problem multiplied from the left with the matrix T. Note that the θ phase brought into the full solution by the matrix T is the topological phase of the full solution induced by the non-trivial topology of the Hamiltonian.

The S matrix is obtained by matching $\psi(k)$ with the semiclassical solution of (5.29). Since H_n' is topologically equivalent to H_1 (note that the

dynamical variables are k_y and k_z, while k_x is fixed), the topological phase shift of the semiclassical solution is given by (5.17), which cancels the θ phase of the full solution and the result is the same θ-independent scattering matrix (5.24), with δ_0 replaced by δ_n. In particular, the breakthrough phase shift $\phi_b = \pi$ also holds in the topological case.

5.5 Discussion

Having thus calculated the phase shifts, we now show the full θ-dependence of the offset γ, defined in Eq. (5.4), in Figs. 5.2a and 5.2b. In practice, the offset can only be measured modulo one, corresponding to one Landau-level spacing. Nevertheless in Figs. 5.2a and 5.2b we plot the full γ for clarity of the graphic. For the figure-of-8 orbit, the magnetic breakthrough contributes an offset $1/2$ and the topological charge adds an extra contribution $n/2$. The θ independence is based on the cancellation of the θ-dependent parts from the hole and the electron pockets. The universality of the breakthrough phase shift is, instead, less surprising, since the same universal value was found previously for non-topological band touchings [182]. In contrast, without breakthrough (dashed/dotted curves in Fig. 5.2b) or in case of a type-I Weyl node (Fig. 5.2a), the offset has a non-trivial dependence on the orbit details that are encoded in θ. The only exception is the case $n = 1$ of the type-I Weyl node, which shows no θ dependence owing to the higher symmetry of the dispersion [165]. This is also the only case with a known full quantum-mechanical solution [164, 186–188, 190, 191]; it agrees with our semiclassical result. In quantum oscillation experiments, the measured phase shift would likely be averaged over a range of values of the energy and of the parallel momentum k_x, corresponding to a weighted (depending on details of the experimental realization) average over the parameter θ. In general, this averaging does not destroy the θ dependence, still allowing to discriminate the two cases of quantized and continuously varying γ.

With regard to the figure-8 breakthrough orbits, our calculations explain recent numerical findings for the offset of a thin-film Weyl semimetal [192] and a type-II Weyl semimetal [81], showing, respectively, $\gamma = 1/2$ and $\gamma = 0$. In the case of the thin film, the Hamiltonian at the figure-8 crossing, given in the appendix of Ref. [192], is equivalent to the non-topological Hamiltonian H_0, thus the only phase contributing is the breakthrough phase $\phi_b = \pi$, which explains the offset $\gamma = \phi_b/2\pi = 1/2$. In case of the type-II Weyl semimetal, the Hamiltonian is equivalent to H_1, where the additional topological phase $\phi_t = \pi$ cancels the breakthrough phase, which

explains the vanishing offset. This contradicts a previous interpretation that relates the vanishing offset of the latter to a vanishing Berry phase and neglects the contribution of the breakthrough phase [166]. In Appendix 5.8 we present extensions of the numerical calculations to the cases $n = 2$ and $n = 3$, tilted type-I Weyl cones, and several values of θ. Also these calculations are in agreement with the analytical results of this work.

5.6 Appendix A. Topological phases

Type-II $(u > 1)$

While the sum of the phases $\phi_{\mathrm{t}}^{\pm}$ has been calculated in the main text, to obtain each of the phases separately we now focus on the difference. From (5.15) we find

$$\phi_{\mathrm{t}}^{-} - \phi_{\mathrm{t}}^{+} = \int_{-\infty}^{\infty} d\kappa \, \frac{n \cot \theta}{(\kappa^2 + 1)\sqrt{(\kappa^2 + 1)^n + \cot^2 \theta}}. \tag{5.32}$$

Using the series expansion

$$\frac{1}{\sqrt{1+q}} = \sum_{m=0}^{\infty} \binom{m - \frac{1}{2}}{m} (-q)^m \tag{5.33}$$

and the integral

$$\int_{-\infty}^{\infty} d\kappa \, \frac{1}{(\kappa^2 + 1)^\alpha} = \frac{\sqrt{\pi}\,\Gamma\!\left(\alpha - \frac{1}{2}\right)}{\Gamma(\alpha)}, \tag{5.34}$$

Eq. (5.32) can be written as

$$\phi_{\mathrm{t}}^{-} - \phi_{\mathrm{t}}^{+} = n \cot \theta \sum_{m=0}^{\infty} (-1)^m \binom{m - \frac{1}{2}}{m}$$

$$\times \frac{\sqrt{\pi}\,\Gamma\!\left(nm + \frac{n+1}{2}\right)}{\Gamma\!\left(nm + \frac{n+2}{2}\right)} (\cot \theta)^{2m}. \tag{5.35}$$

For $n = 1$ the series is the expansion of $2 \arctan(\cot \theta)/\cot \theta$, which gives

$$\phi_{\mathrm{t}}^{-} - \phi_{\mathrm{t}}^{+} = \mathrm{sign}(\theta)\pi - 2\theta. \tag{5.36}$$

Together with (5.18), $\phi_{\mathrm{t}}^{-} + \phi_{\mathrm{t}}^{+} = n\pi$, this leads to

$$\phi_{\mathrm{t}}^{\pm} = \frac{\pi}{2}(1 \mp \mathrm{sign}\theta) \pm \theta. \tag{5.37}$$

Type-I $(u < 1)$

For $u < 1$, $k_z^\pm$ are two parts of a single closed contour. The phase ϕ_{t} of the contour is thus given by the difference $\phi_{\mathrm{t}} = \phi_{\mathrm{t}}^+ - \phi_{\mathrm{t}}^-$, where, using (5.14), (5.16), and the substitution $\kappa = k_y'/k_x$, $\phi_{\mathrm{t}}^\pm$ are given by

$$\phi_{\mathrm{t}}^\pm = -\int_{-\kappa_0}^{\kappa_0} d\kappa \, \frac{n(\kappa^2 + 1)^{n-1}}{2\sqrt{\coth^2\theta - (\kappa^2 + 1)^n}} \left(\sqrt{\coth^2\theta - (\kappa^2 + 1)^n} \pm \coth\theta \right)^{-1},$$
(5.38)

where $\kappa_0 = \sqrt{(\coth\theta)^{2/n} - 1}$. The difference reduces to

$$\phi_{\mathrm{t}} = \int_{-\kappa_0}^{\kappa_0} d\kappa \, \frac{n \coth\theta}{(\kappa^2 + 1)\sqrt{\coth^2\theta - (\kappa^2 + 1)^n}}$$
(5.39)

and, after the substitution $z = (\kappa^2 + 1)^n$, can be rewritten as

$$\phi_{\mathrm{t}} = \int_1^{\coth^2\theta} dz \, \frac{\coth\theta}{z\sqrt{\coth^2\theta - z}\sqrt{z^{1/n} - 1}}.$$
(5.40)

A closed-form solution is found for $n = 1$,

$$\phi_{\mathrm{t}} = \pi \, \mathrm{sign}\theta.$$
(5.41)

For a general n we find in the limits $\theta \to 0^\pm$

$$\phi_{\mathrm{t}} \xrightarrow{\theta \to 0^\pm} n\,\pi\,\mathrm{sign}\theta$$
(5.42)

and $\theta \to \pm\infty$

$$\phi_{\mathrm{t}} \xrightarrow{\theta \to \pm\infty} \sqrt{n}\,\pi\,\mathrm{sign}\theta.$$
(5.43)

5.7 Appendix B. Scattering matrix for magnetic breakdown

Non-topological Hamiltonian

To obtain the full solution in the magnetic-breakthrough region, we solve the differential equation

$$\left[\sigma_x \delta + \sigma_y k + i\partial_k\right]\psi = 0.$$
(5.44)

Multiplying from the left with $U = \exp(-i\sigma_x\pi/4)$ and inserting the ansatz $\psi = U^\dagger(\eta, \xi)^T$ we obtain

$$\left(k^2 + \partial_k^2 - i + \delta^2\right)\eta = 0, \tag{5.45}$$

$$\xi = -\delta^{-1}\left(k + i\partial_k\right)\eta. \tag{5.46}$$

Equation (5.45) can be transformed to Weber's equation for the parabolic cylinder function,

$$\eta'' - \left(\tfrac{1}{4}z^2 + a\right)\eta = 0, \tag{5.47}$$

where

$$z = \sqrt{2}e^{i\pi/4}\, k, \quad a = \tfrac{1}{2} + i\gamma, \quad \gamma = \tfrac{1}{2}\delta^2. \tag{5.48}$$

The two solutions read

$$\eta_a = e^{-z^2/4}\, {}_1F_1\left(\tfrac{1}{2}a + \tfrac{1}{4}; \tfrac{1}{2}; \tfrac{1}{2}z^2\right), \tag{5.49a}$$

$$\eta_b = z\, e^{-z^2/4}\, {}_1F_1\left(\tfrac{1}{2}a + \tfrac{3}{4}; \tfrac{3}{2}; \tfrac{1}{2}z^2\right), \tag{5.49b}$$

where ${}_1F_1()$ is the confluent hypergeometric function. Its general asymptotic form for a large last argument reads

$$_1F_1(\alpha, \beta, ik^2) \xrightarrow{k\to\infty} \Gamma(\beta)\left(\tfrac{1}{\Gamma(\alpha)}e^{ik^2}(ik^2)^{\alpha-\beta} + \tfrac{1}{\Gamma(\beta-\alpha)}(-ik^2)^{-\alpha}\right). \tag{5.50}$$

From this we obtain the asymptotic form of the two solutions (5.49),

$$\eta_a = \frac{\Gamma\left(\tfrac{1}{2}\right)}{\Gamma\left(\gamma\tfrac{i}{2} + \tfrac{1}{2}\right)}e^{ik^2/2 + i\gamma\ln|k| - \pi\gamma/4}, \tag{5.51a}$$

$$\eta_b = \text{sign}(k)\frac{\sqrt{2}\Gamma\left(\tfrac{3}{2}\right)}{\Gamma\left(\gamma\tfrac{i}{2} + 1\right)}e^{ik^2/2 + i\gamma\ln|k| - \pi\gamma/4}. \tag{5.51b}$$

Inserting into (5.46), we obtain the two corresponding expressions for ξ,

$$\xi_a = -\text{sign}(k)\frac{\sqrt{2\pi/\gamma}}{\Gamma\left(-\gamma\tfrac{i}{2}\right)}e^{-ik^2/2 - i\gamma\ln|k| + i\pi/4 - \pi\gamma/4}, \tag{5.52a}$$

$$\xi_b = -\frac{\sqrt{\pi/\gamma}}{\Gamma\left(\tfrac{1}{2} - \gamma\tfrac{i}{2}\right)}e^{-ik^2/2 - i\gamma\ln|k| + i3\pi/4 - \pi\gamma/4}. \tag{5.52b}$$

Altogether, an arbitrary solution of (5.44) at $|k| \gg \delta$ is thus the linear combination

$$\psi(k) = e^{i\sigma_x\pi/4}\Psi(k)\boldsymbol{a}, \quad \Psi(k) = \begin{pmatrix} \eta_a & \eta_b \\ \xi_a & \xi_b \end{pmatrix}, \quad \boldsymbol{a} = \begin{pmatrix} a_1 \\ a_2 \end{pmatrix}, \tag{5.53}$$

Figure 5.3: Classical trajectories along the equi-energy contours $k_z^{\pm}(k)$ approaching and leaving the magnetic-breakdown region. The in- and outgoing scattering states, $\psi_i^{\pm}$ and $\psi_f^{\pm}$, respectively, are also indicated.

where a_1, a_2 are arbitrary coefficients.

The approximate semiclassical solution of (5.44) reads [182, 193]

$$\psi_s(k) = \chi(k) \, e^{-i \int_0^k dk' \, k_z(k') + \phi_t(k)}, \tag{5.54}$$

where $\chi(k)$ and $k_z(k)$ are determined by

$$\left[\sigma_x \delta + \sigma_y k + k_z^{\pm}(k)\right]\chi_{\pm}(k) = 0, \tag{5.55}$$

$$k_z^{\pm}(k) = \pm\sqrt{k^2 + \delta^2} \tag{5.56}$$

and $\phi_t(k)$ is the topological phase shift accumulated on the orbit section between $k_y = 0$ and $k_y = k$,

$$\phi_t(k) = i \int_0^k dk'_y \, \chi_{\pm}^{\dagger}(k)\partial_k \chi_{\pm}(k) = \int_0^k dk' \frac{\delta}{2(\delta^2 + (k')^2)}$$

$$= \arctan(k/\delta)/2. \tag{5.57}$$

The first term in the exponent of the semiclassical wavefunction can be written as

$$\int_0^k dk' k_z^{\pm}(k') = \pm \, \text{sign}(k) f(k) + \mathcal{O}\big(\delta_0^2/k^2\big), \tag{5.58a}$$

$$f(k) = \tfrac{1}{2}\big[k^2 + \delta_0^2\big(\ln|2k/\delta_0| + 1/2\big)\big]. \tag{5.58b}$$

The basis for the scattering matrix is formed by the semiclassical wavefunctions at $k \ll -\delta$ as incoming states ψ_i and at $k \gg \delta$ as outgoing states

ψ_f, as indicated in Fig. 5.3. To leading order in δ/k we obtain

$$\psi_i^\pm = e^{\pm if(k)} \frac{1}{\sqrt{2}} \begin{pmatrix} \mp e^{i\pi/4} \\ e^{-i\pi/4} \end{pmatrix}, \tag{5.59}$$

$$\psi_f^\pm = e^{\mp if(k)} \frac{1}{\sqrt{2}} \begin{pmatrix} \mp e^{-i\pi/4} \\ e^{i\pi/4} \end{pmatrix} \tag{5.60}$$

and combine the scattering states into matrices,

$$\Psi_i(k) = (\psi_i^+, \psi_i^-), \qquad \Psi_f(k) = (\psi_f^+, \psi_f^-). \tag{5.61}$$

We choose the coefficients of the full solution, $\boldsymbol{a}$, such that at $k_y \ll -\delta$ the full solution coincides with the incoming state, $\Psi_i \boldsymbol{c}_i$, where according to (5.61), $\boldsymbol{c}_i = (1,0)$ corresponds to incoming state ψ_i^+ and $\boldsymbol{c}_i = (0,1)$ corresponds to incoming state ψ_i^-. At $k \gg \delta$ the phase and amplitude of the final states, combined in $\boldsymbol{c}_f$, is then determined by matching $\psi(k)$ with $\Psi_f \boldsymbol{c}_f$. Altogether, the matching conditions read

$$\Psi_i(k \ll -\delta)\boldsymbol{c}_i = \Psi(k \ll -\delta)\boldsymbol{a}, \tag{5.62}$$

$$\Psi(k \gg \delta)\boldsymbol{a} = \Psi_f(k \gg \delta)\boldsymbol{c}_f. \tag{5.63}$$

Eliminating $\boldsymbol{a}$ we obtain the expression for the scattering matrix S

$$\boldsymbol{c}_f = \underbrace{\Psi_f(k)^{-1}\Psi(k)\Psi^{-1}(-k)\Psi_i(-k)}_{\equiv S} \boldsymbol{c}_i, \quad k/\delta \to +\infty. \tag{5.64}$$

Inserting the expressions $\Psi_f(k)$, $\Psi_i(k)$, and $\Psi(k)$ given above, we obtain the scattering matrix (5.24) given in the main text.

Topological Hamiltonian

We consider the Schrödinger equation

$$\Big[\delta_n \sqrt{u^2 - 1}\sin\theta\sigma_x + k\sqrt{u^2 - 1}\sigma_y$$
$$+ i\partial_k(u + \sigma_z) + \delta_n \cos\theta(1 + u\sigma_z)\Big]\psi = 0. \tag{5.65}$$

The semiclassical solution reads

$$\psi_s(k) = \chi(k)\, e^{-i\int_0^k dk'\, k_z(k') + \phi_t(k)}, \tag{5.66}$$

where $\chi(k)$ and $k_z(k)$ are given by

$$\left[\delta_n\sqrt{u^2-1}\sin\theta\sigma_x + k\sqrt{u^2-1}\sigma_y + k_z^\pm(k)(u+\sigma_z)\right.$$
$$\left. + \delta_n\cos\theta(1+u\sigma_z)\right]\chi_\pm(k) = 0,$$

$$(5.67)$$

$$k_z^\pm(k) = \pm\sqrt{k^2+\delta_n^2}. \qquad (5.68)$$

The phase $\int_0^k dk' k_z^\pm(k')$ is in analogy to the non-topological case given by (5.58) (with δ_0 replaced by δ_n). The topological phase shift is most easily obtained by considering the original Schrödinger equation

$$H_n'\psi = \epsilon\psi, \qquad (5.69)$$
$$H_n' = k_x^n\sigma_x + nk_x^{n-1}k_y\sigma_y + k_z\sigma_z + uk_z, \qquad (5.70)$$

which is related to (5.65) by a k_z shift introduced in (5.27) in the main text, which leaves the phase shift accumulated between $k=0$ and $k=\pm\infty$ invariant. The Hamiltonian is of the form of H_1. The topological phase shift thus calculates in analogy to the phase $\phi_\mathrm{t}^{1\pm}$ of the main text. Since by symmetry the phase shift from $k=0$ to $k=\pm\infty$ is half the phase shift from $k=-\infty$ to $k=\infty$, we can use Eq. (5.17) to obtain

$$\phi_\mathrm{t}^{n\pm}(k=\infty) = \frac{\pi}{4}(1\mp\mathrm{sign}\theta) \pm \frac{\theta}{2}, \qquad (5.71)$$

which is sufficient for the in- and outgoing states at $k=\pm\infty$. Together with the spinors from (5.67) the scattering states read

$$\psi_i^\pm = e^{\pm if(k)-i\frac{\pi}{4}(1\mp\mathrm{sign}\theta)\mp i\theta/2}\begin{pmatrix}\mp i\sqrt{\frac{u-1}{2u}}\\ \sqrt{\frac{u+1}{2u}}\end{pmatrix}, \qquad (5.72\mathrm{a})$$

$$\psi_f^\pm = e^{\mp if(k)+i\frac{\pi}{4}(1\mp\mathrm{sign}\theta)\pm i\theta/2}\begin{pmatrix}\pm i\sqrt{\frac{u-1}{2u}}\\ \sqrt{\frac{u+1}{2u}}\end{pmatrix}. \qquad (5.72\mathrm{b})$$

To find the full solution $\psi(k)$ we multiply (5.65) from the left with $\mathcal{M} = \mathrm{diag}[(u+1)^{-1}, (u-1)^{-1}]$ and apply a transformation given by

$$T = -i\begin{pmatrix}\frac{1-u}{\sqrt{u^2-1}} & \frac{u-1}{\sqrt{u^2-1}}\\ 1 & 1\end{pmatrix}\sigma_z e^{-i\sigma_y\theta/2}, \qquad (5.73)$$
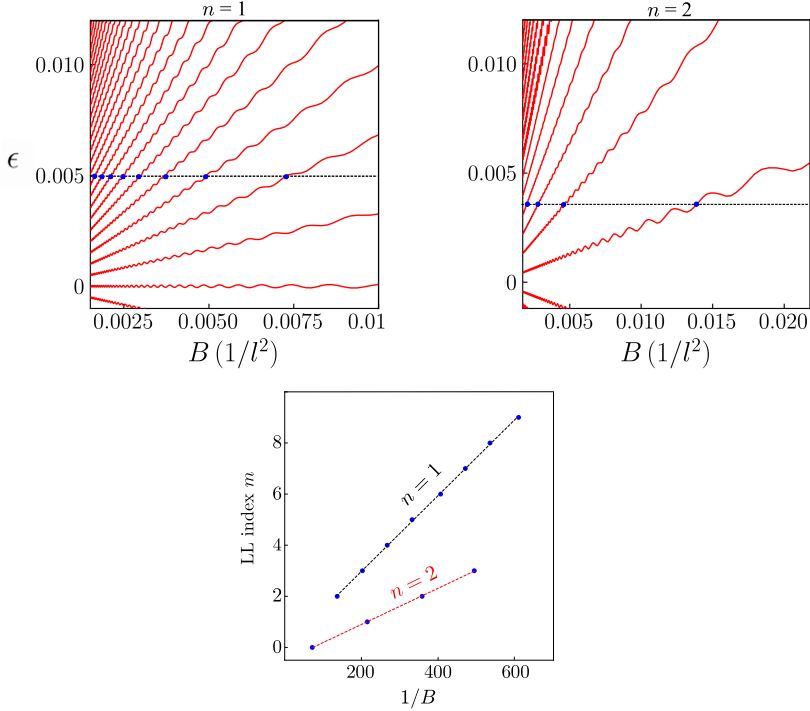
Figure 5.4: (a) Landau fan diagrams for type II Weyl nodes with topological charge $n = 1$ (left) and $n = 2$ (rigth) at $k_x = 0.005$ and $k_x = 0.03$, respectively. Other parameters are $u = 1.6$, $\eta = 0.1$, and $N_{cut} = 2400$. (b) Landau-level (LL) index m as a function of the inverse field for $n = 1, 2$ at fixed energies indicated by the black dashed lines in (a). The dots correspond to the numerical data, the dashed lines to the linear fits according to Eq. (5.77).

which leads to the differential equation of the Landau-Zener form (5.44),

$$\hat{H}\hat{\psi}(k) = \big(i\partial_k\sigma_0 + \delta_n\,\sigma_x + k\,\sigma_y\big)\hat{\psi}(k) = 0, \qquad (5.74)$$

where $\hat{\psi}(k) = T^{-1}\psi(k)$ and $\hat{H} = T^{-1}\mathcal{M}\tilde{H}T$. As in the non-topological case, we obtain the S matrix by matching the full solution with the scattering states, $T^{-1}\psi_{i/f}^{\pm}$, which leads to the scattering matrix (5.24) with δ_0 replaced by δ_n.

5.8 Appendix C. Numerical results

To give support to the analytical calculations, we numerically compute the offset γ for type I and type II single, double, and triple Weyl nodes via numerical diagonalization of the Hamiltonian $H'_n = H_n(\boldsymbol{k'}) + \eta k'^3_z \sigma_z$, with H_n given by Eq. (5.2b) of the main text, and the regularizing term $\eta k'^3_z \sigma_z$ to ensure closed Fermi pockets in the case $u > 1$, as discussed in the main text. The magnetic field in the x direction enters according to the Peierls substitution $\boldsymbol{k'} = \boldsymbol{k} + \boldsymbol{A}$, with

$$k'_x = k_x, \quad [k'_y, k'_z] = -iB\,. \tag{5.75}$$

We make use of the ladder operators a and $a^\dagger$ of the quantum oscillator to construct momentum operators with the required properties. Straightforwardly,

$$k'_y = (a + a^\dagger)\sqrt{\frac{B}{2}}, \quad k'_z = i(a - a^\dagger)\sqrt{\frac{B}{2}} \tag{5.76}$$

with $[a, a^\dagger] = 1$, fulfil the commutator in Eq. (5.75).

The ladder operators are calculated in the basis of the Landau-level eigenstates (eigenstates of $a^\dagger a$), yielding the matrix elements $(a)_{ij} = \delta_{i,j+1}\sqrt{j}$ and $(a^\dagger)_{ij} = \delta_{i,j-1}\sqrt{i}$, respectively. The lowest l Landau levels are obtained by sparse diagonalization of the Hamiltonian constructed from ladder operators truncated to $i, j \in [1, N_{cut}]$ with $N_{cut} \gg l$, ensuring convergence of the eigenvalues with the value of N_{cut}.

The fan diagrams, shown in Fig. 5.4, are obtained by repeating this procedure at different values of the magnetic-field strength. For type-II Weyl orbits the limit of unit breakthrough probability is never achieved in practice, resulting in non-monotonic contribution to Landau-level energies [182, 193], producing oscillations on top of the fans in Fig. 5.4. These, however, are not the subject of our present analytical study. Therefore, in order to better extract the phase shift, we suppress these oscillations for $n = 2$ and $n = 3$ by averaging the energies over a range of magnetic fields containing several oscillation peaks (dips).

At a fixed energy ϵ, we extract the intercept fields $\{B_m\}$, where B_m is the value of the field at which the energy of the mth Landau level equals ϵ. The inverse of the intercept fields are then fitted to the quantization condition, Eq. (5.1) of the main text,

$$\frac{1}{B_m} = \frac{2\pi}{S(\epsilon)}(m + \gamma)\,, \tag{5.77}$$
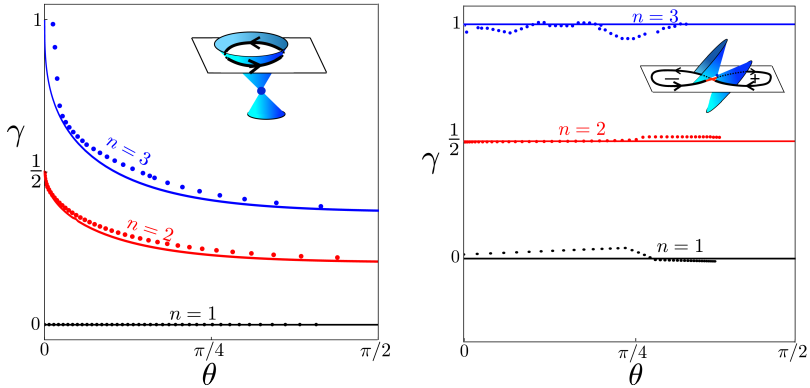
Figure 5.5: Parameter dependence of the offset γ (modulo one) for cyclotron orbits at type-I (left) and type-II (right) Weyl nodes obtained numerically (dots), compared to the analytical results (solid lines) of the main text [cf. Figs. 5.2a and 5.2b]. Parameters for numerical results are $u = 1.6$ ($u = 7$), $\eta = 0.1$ ($\eta = 1$), and $N_{cut} = 2400$ ($N_{cut} = 800$) for $n = 1, 2$ ($n = 3$). The relatively large value of u and η for $n = 3$ were necessary to access large values of θ [cf. Eq. (5.16)], at the same time closing the contour at not too large momenta.

where the zero-field area $S(\epsilon)$ enclosed by the equi-energy contour is calculated numerically from the dispersion at $B = 0$. The offset γ modulo one is thus obtained as the only fitting parameter.

The results, shown in Fig. 5.5, are in good agreement with the analytical results presented in the previous sections, for all the cases that we were able to address numerically. The phase offset $\gamma = 1/2$ corresponding to the non-protected band-touching Hamiltonian (5.2a) was obtained numerically in the context of figure-8 cyclotron orbits in a thin-film Weyl semimetal [192], also in agreement with the analytical results of this chapter.

Bibliography

[1] J. J. Sakurai, *Advanced Quantum Mechanics*, Addison-Wesley, Reading, MA, (1967).

[2] R. Winkler, *Spin-orbit coupling effects in two-dimensional electron and hole systems*, Springer-Verlag, Berlin, Heidelberg, New York, second edition, (2003).

[3] M. Z. Hasan and C. L. Kane, *Topological insulators*, Rev. Mod. Phys. **82**, 3045 (2010).

[4] A. B. Bernevig, T. A. Hughes, and S. C. Zhang, *Quantum spin Hall effect and topological phase transition in HgTe quantum Wells*, Science **314**, 1757 (2006).

[5] L. Fu and C. L. Kane, *Topological insulators with inversion symmetry*, Phys. Rev. B **76**, 045302 (2007).

[6] A. Soumyanarayanan, N. Reyren, A. Fert, and C. Panagopoulos, *Emergent phenomena induced by spin–orbit coupling at surfaces and interfaces*, Nature **539**, 509 (2016).

[7] Y. A. Bychkov and E. I. Rashba, *Oscillatory effects and the magnetic susceptibility of carriers in inversion layers*, J. Phys. C: Solid State Phys. **17**, 6039 (1984).

[8] M. Schultz, F. Heinrichs, U. Merkt, T. Collin, T. Skauli, and S. Løvold, *Rashba spin splitting in a gated HgTe quantum well*, Semicond. Sci. Technol. **11**, 1168 (1996).

[9] S. Datta and B. Das, *Electronic analog of the electro-optic modulator*, Appl. Phys. Lett. **56**, 665 (1990).

[10] S. LaShell, B. A. McDougall, and E. Jensen, *Spin splitting of an Au(111) surface state band observed with Angle Resolved Photoelectron Spectroscopy*, Phys. Rev. Lett. **77**, 3419 (1996).

Bibliography

[11] D. Hsieh, Y. Xia, D. Qian, L. Wray, J. H. Dil, F. Meier, J. Oster-walder, L. Patthey, J. G. Checkelsky, N. P. Ong, A. V. Fedorov, H. Lin, A. Bansil, D. Grauer, Y. S. Hor, R. J. Cava, and M. Z. Hasan, *A tunable topological insulator in the spin helical Dirac transport regime*, Nature **460**, 1101 (2009).

[12] C. L. Kane and E. J. Mele, *Z_2 Topological order and the quantum spin Hall effect*, Phys. Rev. Lett. **95**, 146802 (2005); C. L. Kane and E. J. Mele, *Quantum spin Hall effect in graphene*, Phys. Rev. Lett. **95**, 226801 (2005).

[13] M. König, S. Wiedmann, C. Brüne, A. Roth, H. Buhmann, L. W. Molenkamp, X. L. Qi, and S. C. Zhang, *Quantum spin Hall insulator state in HgTe quantum wells*, Science **318**, 766 (2007).

[14] M. Z. Hasan, S.-Y. Xu, I. Belopolski, and S.-M. Huang, *Discovery of Weyl fermion semimetals and topological Fermi arc states*, Annu. Rev. Condens. Matter Phys. **8** (2017).

[15] Z. Zhong, A. Tóth, and K. Held, *Theory of spin-orbit coupling at $LaAlO_3$ /$SrTiO_3$ interfaces and $SrTiO_3$ surfaces*, Phys. Rev. B **87**, 161102(R) (2013).

[16] C. N. R. Rao, *Transition metal oxides*, Annu. Rev. Phys. Chem. **40**, 291 (1989).

[17] J. G. Bednorz and K. A. Mueller, *Possible high T_c superconductivity in the $Ba-La-Cu-O$ system*, Z. Phys. B **64**, 189 (1986).

[18] S. Hadlington, *Perovskite coat gives hybrid solar cells a boost*, RSC Chemistry world (2012).

[19] O. Prakash, A. Kumar, A. Thamizhavel, and S. Ramakrishnan, *Evidence for bulk superconductivity in pure bismuth single crystals at ambient pressure*, Science **355**, 52 (2017).

[20] J. F. Schooley, W. R. Hosler, and M. L. Cohen, *Superconductivity in semiconducting $SrTiO_3$*, Phys. Rev. Lett. **12**, 474 (1964).

[21] Y.-Y. Pai, A. Tylan-Tyler, P. Irvin, and J. Levy, *Physics of $SrTiO_3$ - based heterostructures and nanostructures: a review*, Rep. Prog. Phys. **81**, 036503 (2018).

[22] E. Sawaguchi, A. Kikuchi, and Y. Kodera, *Dielectric constant of strontium titanate at low temperatures*, J. Phys. Soc. Jpn. **17**, 1666 (1962).

[23] A. Ohtomo and H. Y. Hwang, *A high-mobility electron gas at the LaAlO₃/SrTiO₃ heterointerface*, Nature **427**, 423 (2004).

[24] S. Thiel, G. Hammerl, A. Schmehl, C. W. Schneider, and J. Mannhart, *Tunable quasi-two-dimensional electron gases in oxide heterostructures*, Science **313**, 1942 (2006).

[25] N. Nakagawa, H. Y. Hwang, and D. A. Muller, *Why some interfaces cannot be sharp*, Nat. Mater. **5**, 204 (2006).

[26] M. Ben Shalom, A. Ron, A. Palevski, and Y. Dagan, *Shubnikov-De Haas oscillations in SrTiO₃ / LaAlO₃ interface*, Phys. Rev. Lett. **105**, 206401 (2010).

[27] A. D. Caviglia, S. Gariglio, C. Cancellieri, B. Sacepé, A. Fête, N. Reyren, M. Gabay, A. F. Morpurgo, and J.-M. Triscone, *Two-dimensional quantum oscillations of the conductance at LaAlO₃ / SrTiO₃ interfaces*, Phys. Rev. Lett. **105**, 236802 (2010).

[28] S. Gariglio, A. Fête, and J. M. Triscone, *Electron confinement at the LaAlO₃ / SrTiO₃ interface*, J. Phys.: Condens. Matter **27**, 283201 (2015).

[29] Y.-L. Han, S.-C. Shen, J. You, H.-O. Li, Z.-Z. Luo, C.-J. Li, G.-L. Qu, C.-M. Xiong, R.-F. Dou, L. He, D. Naugle, G.-P. Guo, and J. -C. Nie, *Two-dimensional superconductivity at (110) LaAlO₃ / SrTiO₃ interfaces*, Appl. Phys. Lett. **105**, 192603 (2014).

[30] L. Li, C. Richter, J. Mannhart, and R. C. Ashoori, *Coexistence of magnetic order and two-dimensional superconductivity at LaAlO₃ / SrTiO₃ interfaces*, Nat. Phys. **7**, 762 (2011).

[31] L. Yu and A. Zunger, *A polarity-induced defect mechanism for conductivity and magnetism at polar-nonpolar oxide interfaces*, Nat. Commun. **5**, 5118 (2014).

[32] Y. Li. X. Wei, and J. Yu, *Inevitable high density of oxygen vacancies on the surface of LaAlO₃ / SrTiO₃ heterostructures*, arXiv:1804.04502.

[33] N. Reyren, S. Thiel, A. D. Caviglia, L. F. Kourkoutis, G. Hammerl, C. Richter, C. W. Schneider, T. Kopp, A.-S. Rüetschi, D. Jaccard, M. Gabay, D. A. Muller, and J.-M. Triscone, *Superconducting interfaces between insulating oxides*, Science **317**, 1196 (2007).

[34] A. D. Caviglia, S. Gariglio, N. Reyren, D. Jaccard, T. Schneider, M. Gabay, S. Thiel, G. Hammerl, J. Mannhart, and J.-M. Triscone, *Electric field control of the LaAlO$_3$ / SrTiO$_3$ interface ground state*, Nature **456**, 624 (2008).

[35] A. D. Caviglia, M. Gabay, S. Gariglio, N. Reyren, C. Cancellieri, and J.-M. Triscone, *Tunable Rashba spin-orbit interaction at oxide interfaces*, Phys. Rev. Lett. **104**, 126803 (2010).

[36] A. Joshua, S. Pecker, J. Ruhman, E. Altman, and S. Ilani, *A universal critical density underlying the physics of electrons at the LaAlO$_3$ / SrTiO$_3$ interface*, Nat. Commun. **3**, 1129 (2012).

[37] C. Richter, H. Boschker, W. Dietsche, E. Fillis-Tsirakis, R. Jany, F. Loder, L. F. Kourkoutis, D. A. Muller, J. R. Kirtley, C. W. Schneider, and J. Mannhart, *Interface superconductor with gap behaviour like a high-temperature superconductor*, Nature **502**, 528 (2013).

[38] Ø. Fischer, M. Kugler, I. Maggio-Aprile, C. Berthod, and C. Renner, *Rev. Mod. Phys.* **79**, 353 (2007).

[39] S. Caprara, M. Grilli, L. Benfatto, and C. Castellani, *Effective medium theory for superconducting layers: A systematic analysis including space correlation effects*, Phys. Rev. B **84**, 014514 (2011).

[40] D. Bucheli, S. Caprara, C. Castellani, and M. Grilli, *Metal–superconductor transition in low-dimensional superconducting clusters embedded in two-dimensional electron systems*, New J. Phys. **15**, 023014 (2013).

[41] S. Caprara, J. Biscaras, N. Bergeal, D. Bucheli, S. Hurand, C. Feuillet-Palma, A. Rastogi, R. C. Budhani, J. Lesueur, and M. Grilli, *Multiband superconductivity and nanoscale inhomogeneity at oxide interfaces*, Phys. Rev. B **88**, 020504(R) (2013).

[42] Ariando, X. Wang, G. Baskaran, Z. Q. Liu, J. Huijben, J. B. Yi, A. Annadi, A. Roy Barman, A. Rusydi, S. Dhar, Y. P. Feng, J. Ding, H. Hilgenkamp, and T. Venkatesan, *Electronic phase separation at the LaAlO$_3$ / SrTiO$_3$ interface*, Nat. Commun. **2**, 188 (2011).

[43] J. A. Bert, B. Kalisky, C. Bell, M. Kim, Y. Hikita, H. Y. Hwang, and K. A. Moler, *Direct imaging of the coexistence of ferromagnetism and superconductivity at the LaAlO₃ / SrTiO₃ interface*, Nat. Phys. **7**, 767 (2011).

[44] N. Scopigno, D. Bucheli, S. Caprara, J. Biscaras, N. Bergeal, J. Lesueur, and M. Grilli, *Phase separation from electron confinement at oxide interfaces*, Phys. Rev. Lett. **116**, 026804 (2016).

[45] K. Michaeli, A. C. Potter, and P. A. Lee, *Superconducting and ferromagnetic phases in SrTiO₃ / LaAlO₃ oxide interface structures: possibility of finite momentum pairing*, Phys. Rev. Lett. **108**, 117003 (2012).

[46] F. Bi, M. Huang, S. Ryu, H. Lee, C.-W. Bark, C.-B Eom, P. Irvin, and J. Levy, *Room-temperature electronically-controlled ferromagnetism at the LaAlO₃ / SrTiO₃ interface*, Nat. Commun. **5**, 5019 (2014).

[47] J. Kondo, *Resistance minimum in dilute magnetic alloys*, Progr. Theor. Phys. **32** (1), 37 (1964).

[48] J. Ruhman, A. Joshua, S. Ilani, and E. Altman, *Competition between Kondo screening and magnetism at the LaAlO₃ / SrTiO interface*, Phys. Rev. B **90**, 125123 (2014).

[49] A. Brinkman, M. Huijben, M. van Zalk, J. Huijben, U. Zeitler, J. C. Maan, W. G. van der Wiel, G. Rijnders, D. H. A. Blank, and H. Hilgenkamp, *Magnetic effects at the interface between non-magnetic oxides*, Nat. Mater. **6**, 493 (2007).

[50] A. Joshua, J. Ruhman, S. Pecker, E. Altman, and S. Ilani, *Gate-tunable polarized phase of two-dimensional electrons at the LaAlO₃ / SrTiO₃ interface*, Proc. Natl Acad. Sci. **110**, 9633 (2013).

[51] M. Diez, A. M. R. V. L. Monteiro, G. Mattoni, E. Cobanera, T. Hyart, E. Mulazimoglu, N. Bovenzi, C. W. J. Beenakker, and A. D. Caviglia, *Giant negative magnetoresistance driven by spin–orbit coupling at the LaAlO₃ / SrTiO₃ interface*, Phys. Rev. Lett. **115**, 016803 (2015).

[52] M. Yang, M. Pierre, O. Toressin, M. Goiran, W. Escoffier, S. Zeng, Z. Huang, H. Kun, T. Venkatesan, Ariando, and M. Coey, *High field magneto-transport in two-dimensional electron gas LaAlO₃ / SrTiO₃*, Appl. Phys. Lett. **109**, 122106 (2016).

[53] O. Copie, V. Garcia, C. Bödefeld, C. Carrétéro, M. Bibes, G. Herranz, E. Jacquet, J.-L. Maurice, B. Vinter, S. Fusil, K. Bouzehouane, H. Jaffrès, and A. Barthélémy, *Towards two-dimensional metallic behavior at LaAlO$_3$ / SrTiO$_3$ interfaces*, Phys. Rev. Lett. **102**, 216804 (2009).

[54] G. Khalsa, B. Lee, and A.H. MacDonald, *Theory of t$_{2g}$ electron-gas Rashba interactions*, Phys. Rev. B **88**, 041302 (2013).

[55] C. Herring, *Accidental degeneracy in the energy bands of crystals*, Phys. Rev. **52**, 365 (1937).

[56] H. B. Nielsen and M. Ninomiya, *A no-go theorem for regularizing chiral fermions*, Phys. Lett. B **105**, 219 (1981).

[57] H. Weyl, *Elektron und gravitation*, I. Z. Phys. **56**, 330 (1929).

[58] A. A. Soluyanov, D. Gresch, Z. Wang, Q. Wu, M. Troyer, X. Dai, and B. A. Bernevig, *Type*-II *Weyl semimetals*, Nature **527**, 495 (2015).

[59] C. Fang, M. J. Gilbert, X. Dai, and B. A. Bernevig, *Multi-Weyl topological semimetals stabilized by point group symmetry*, Phys. Rev. Lett. **108**, 266802 (2012).

[60] T. Meng and L. Balents, *Weyl superconductors*, Phys. Rev. B **86**, 054504 (2012).

[61] P. Baireuther, J. Tworzydło, M. Breitkreiz, I. Adagideli, and C. W. J. Beenakker, *Weyl-Majorana solenoid*, New J. Phys. **19**, 025006 (2017).

[62] X. Wan, A. M. Turner, A. Vishwanath, and S. Y. Savrasov, *Topological semimetal and Fermi-arc surface states in the electronic structure of pyrochlore iridates*, Phys. Rev. B **83**, 205101 (2011).

[63] A. A. Burkov and L. Balents, *Weyl semimetal in a topological insulator multilayer*, Phys. Rev. Lett. **107**, 127205 (2011).

[64] D. Bulmash, C.-X. Liu, and X.-L. Qi, *Prediction of a Weyl semimetal in Hg$_{1-x-y}$Cd$_x$Mn$_y$Te*, Phys. Rev. B **89**, 081106(R) (2014).

[65] M. Neupane, S.-Y. Xu, R. Sankar, N. Alidoust, G. Bian, C. Liu, I. Belopolski, T.-R. Chang, H.-T. Jeng, H. Lin, A. Bansil, F. Chou, and M. Zahid Hasan, *Observation of a three-dimensional topological Dirac semimetal phase in high-mobility Cd$_3$As$_2$*, Nat. Commun. **5**, 3786 (2014).

[66] J. Liu and D. Vanderbilt, *Weyl semimetals from noncentrosymmetric topological insulators*, Phys. Rev. B **90**, 155316 (2014).

[67] S. Borisenko, Q. Gibson, D. Evtushinsky, V. Zabolotnyy, B. Büchner, and R. J. Cava, *Experimental realization of a three-dimensional Dirac semimetal*, Phys. Rev. Lett. **113**, 027603 (2014).

[68] Y. Sun, S. C. Wu, and B. Yan, *Topological surface states and Fermi arcs of the noncentrosymmetric Weyl semimetals TaAs, TaP, NbAs, and NbP*, Phys. Rev. B **92**, 115428 (2015).

[69] C. Shekhar, A. K. Nayak, S. Singh, N. Kumar, S.-C. Wu, Y. Zhang, A. C. Komarek, E. Kampert, Y. Skourski, J. Wosnitza, W. Schnelle, A. McCollam, U. Zeitler, J. Kubler, S. S. P. Parkin, B. Yan, and C. Felser, *Observation of chiral magneto-transport in RPtBi topological Heusler compounds*, arXiv:1604.01641.

[70] M. Hirschberger, S. Kushwaha, Z. Wang, Q. Gibson, S. Liang, C. A. Belvin, B. A. Bernevig, R. J. Cava, and N. P. Ong, *The chiral anomaly and thermopower of Weyl fermions in the half-Heusler GdPtBi*, Nat. Mater. **15**, 1161 (2016).

[71] K. Kuroda, T. Tomita, M.-T. Suzuki, C. Bareille, A. A. Nugroho, P. Goswami, M. Ochi, M. Ikhlas, M. Nakayama, S. Akebi, R. Noguchi, R. Ishii, N. Inami, K. Ono, H. Kumigashira, A. Varykhalov, T. Muro, T. Koretsune, R. Arita, S. Shin, T. Kondo, and S. Nakatsuji, *Evidence for magnetic Weyl fermions in a correlated metal*, Nat. Mater. **16**, 1090 (2017).

[72] S. L. Adler, *Axial-vector vertex in spinor electrodynamics*, Phys. Rev. **177**, 2426 (1969).

[73] J. S. Bell and R. W. Jackiw, *A PCAC puzzle: $\pi_0 \rightarrow \gamma\gamma$ in the σ - model*, Nuov. Cim. A60, 47 (1969).

[74] H. B. Nielsen and M. Ninomiya, *The Adler-Bell-Jackiw anomaly and Weyl fermions in a crystal*, Phys. Lett. B **130**, 389 (1983).

[75] A. A. Burkov, *Chiral anomaly and diffusive magnetotransport in Weyl metals*, Phys. Rev. Lett. **113**, 247203 (2014).

[76] A. A. Burkov, *Negative longitudinal magnetoresistance in Dirac and Weyl metals*, Phys. Rev. B **91**, 245157 (2015).

[77] E. V. Gorbar, V. A. Miransky, and I. A. Shovkovy, *Chiral anomaly, dimensional reduction, and magnetoresistivity of Weyl and Dirac semimetals*, Phys. Rev. B **89**, 085126 (2014).

[78] A. A. Zyuzin and A. A. Burkov, *Topological response in Weyl semimetals and the chiral anomaly*, Phys. Rev. B **86**, 115133 (2012).

[79] P. Baireuther, J. A. Hutasoit, J. Tworzydło, and C. W. J. Beenakker, *Scattering theory of the chiral magnetic effect in a Weyl semimetal: interplay of bulk Weyl cones and surface Fermi arcs*, New J. Phys. **18**, 045009 (2016).

[80] N. Bovenzi and M. Diez, *Semiclassical theory of anisotropic transport at LaAlO$_3$ / SrTiO$_3$ interfaces under in-plane magnetic field*, Phys. Rev. B **95**, 205430 (2017).

[81] T. E. O'Brien, M. Diez, and C. W. J. Beenakker, *Magnetic breakdown and Klein tunneling in a type-II Weyl semimetal*, Phys. Rev. Lett. **16**, 236401 (2016).

[82] H. Boschker and J. Mannhart, *Quantum-matter heterostructures*, Annu. Rev. Cond. Matt. Phys. **8**, 145 (2017).

[83] J. Mannhart, D. H. A. Blank, H. Y. Hwang, A. J. Millis, and J.-M. Triscone, *Two-dimensional electron gases at oxide interfaces*, MRS bulletin, **33**, 1027 (2008).

[84] M. Ben Shalom, M. Sachs, D. Rakhmilevitch, A. Palevski, and Y. Dagan, *Tuning spin-orbit coupling and superconductivity at the SrTiO$_3$ / LaAlO$_3$ interface: a magnetotransport study* , Phys. Rev. Lett. **104**, 126802 (2010).

[85] M. Ben Shalom, C. W. Tai, Y. Lereah, M. Sachs, E. Levy, D. Rakhmilevitch, A. Palevski, and Y. Dagan, *Anisotropic magnetotransport at the SrTiO$_3$ / LaAlO$_3$ interface*, Phys. Rev. B **80**, 140403R (2009).

[86] A. Annadi, Z. Huang, K. Gopinadhan, X. Renshaw Wang, A. Srivastava, Z. Q. Liu, H. Harsan Ma, T. P. Sarkar, T. Venkatesan, and Ariando, *Fourfold oscillation in anisotropic magnetoresistance and planar Hall effect at the LaAlO$_3$ / SrTiO$_3$ heterointerfaces: effect of carrier confinement and electric field on magnetic interactions*, Phys. Rev. B **87**, 201102R (2013).

[87] J.-S. Lee, Y. W. Xie, H. K. Sato, C. Bell, Y. Hikita, H. Y. Hwang, and C.-C. Kao, *Titanium d_{xy} ferromagnetism at the $LaAlO_3$ / $SrTiO_3$ interface*, Nat. Mater. **12**, 703 (2013).

[88] M. R. Fitzsimmons, N. W. Hengartner, S. Singh, M. Zhernenkov, F. Y. Bruno, J. Santamaria, A. Brinkman, M. Huijben, H. J. A. Molegraaf, J. de la Venta, and I. K. Schuller, *Upper limit to magnetism in $LaAlO_3$ / $SrTiO_3$ heterostructures*, Phys. Rev. Lett. **107**, 217201 (2011).

[89] Z. Salman, O. Ofer, M. Radovic, H. Hao, M. Ben Shalom, K. H. Chow, Y. Dagan, M. D. Hossain, C. D. P. Levy, W. A. MacFarlane, G. M. Morris, L. Patthey, M. R. Pearson, H. Saadaoui, T. Schmitt, D. Wang, and R. F. Kiefl, *Nature of weak magnetism in $SrTiO_3$ / $LaAlO_3$ multilayers*, Phys. Rev. Lett. **109**, 257207 (2012).

[90] A. Fête, S. Gariglio, A. D. Caviglia, J.-M. Triscone, and M. Gabay, *Rashba induced magnetoconductance oscillations in the $LaAlO_3$ – $SrTiO_3$ heterostructure*, Phys. Rev. B **86**, 201105(R) (2012).

[91] S. Caprara, F. Peronaci, and M. Grilli, *Intrinsic instability of electronic interfaces with strong Rashba coupling*, Phys. Rev. Lett. **109**, 196401 (2012).

[92] D. Bucheli, M. Grilli, F. Peronaci, G. Seibold, and S. Caprara, *Phase diagrams of voltage-gated oxide interfaces with strong Rashba coupling*, Phys. Rev. B **89**, 195448 (2014).

[93] Q. Song, H. Zhang, T. Su, W. Yuan, Y. Chen, W. Xing, J. Shi, J.-R. Sun, and W. Han, *Observation of inverse Edelstein effect in Rashba-split 2DEG between $SrTiO_3$ and $LaAlO_3$ at room temperature*, Sci. Adv., **3**:e1602312 (2017).

[94] A. Fête, S. Gariglio, C. Berthod, D. Li, D. Stornaiuolo, M. Gabay, and J.-M. Triscone, *Large modulation of the Shubnikov-de Haas oscillations by the Rashba interaction at the $LaAlO_3$ / $SrTiO_3$ interface*, New J. Phys. **16**, 112002 (2014).

[95] Y. Kim, R. M. Lutchyn, and C. Nayak, *Origin and transport signatures of spin-orbit interactions in one- and two-dimensional $SrTiO_3$-based heterostructures*, Phys. Rev. B **87**, 245121 (2013).

[96] P. Kim, K.-T. Kang, G. Go, and J.-H. Han, *Nature of orbital and spin Rashba coupling in the surface bands of $SrTiO_3$ and $KTaO_3$*, Phys. Rev. B **90**, 205423 (2014).

[97] J. Zhou, W.-Y. Shan, and D. Xiao, *Spin responses and effective Hamiltonian for the two-dimensional electron gas at the oxide interface LaAlO₃ / SrTiO₃*, Phys. Rev. B **91**, 241302(R) (2015).

[98] P. D. C. King, S. McKeown Walker, A. Tamai, A. de la Torre, T. Eknapakul, P. Buaphet, S.-K. Mo, W. Meevasana, M. S. Bahramy, and F. Baumberger, *Quasiparticle dynamics and spin–orbital texture of the SrTiO₃ two-dimensional electron gas*, Nat. Commun. **5**, 3414 (2014).

[99] H. Fu, K. V. Reich, and B. I. Shklovskii, *Surface roughness scattering in multisubband accumulation layers*, Phys. Rev. B **93**, 235312 (2016).

[100] D. I. Pikulin, C.-Y. Hou, and C. W. J. Beenakker, *Nernst effect beyond the relaxation-time approximation*, Phys. Rev. B **84**, 035133 (2011).

[101] M. Trushin, K. Výborný, P. Moraczewski, A. A. Kovalev, J. Schliemann, and T. Jungwirth, *Anisotropic magnetoresistance of spin-orbit coupled carriers scattered from polarized magnetic impurities*, Phys. Rev. B **80**, 134405 (2009).

[102] J. M. Ziman, *Principles of the theory of solids* (Cambridge University Press, Cambridge, 1972).

[103] J. M. Ziman, *Approximate calculation of the anisotropy of the relaxation time of the conduction electrons in the noble metals*, Phys. Rev. Lett. **121**, 1320 (1961).

[104] C. M. Varma and E. Abrahams, *Effective Lorentz force due to small-angle impurity scattering: magnetotransport in high-T_c superconductors*, Phys. Rev. Lett. **86**, 4652 (2001).

[105] M. Breitkreiz, P. M. R. Brydon, and C. Timm, *Transport in multiband systems with hot spots on the Fermi surface: forward-scattering corrections*, Phys. Rev. B **89**, 245106 (2014).

[106] E. Maniv, M. Ben Shalom, A. Ron, M. Mograbi, A. Palevski, M. Goldstein, and Y. Dagan, *Strong correlations elucidate the electronic structure and phase-diagram of LaAlO₃ / SrTiO₃ interface*, Nat. Commun. **6**, 8239 (2015).

[107] J. R. Tolsma, A. Principi, R. Asgari, M. Polini, and A. H. MacDonald, *Quasiparticle mass enhancement and Fermi surface shape*

modification in oxide two-dimensional electron gases, Phys. Rev. B **93**, 045120 (2016).

[108] A. F. Santander-Syro, O. Copie, T. Kondo, F. Fortuna, S. Pailhès, R. Weht, X. G. Qiu, F. Bertran, A. Nicolaou, A. Taleb-Ibrahimi, P. Le Fèvre, G. Herranz, M. Bibes, N. Reyren, Y. Apertet, P. Lecoeur, A. Barthélémy, and M. J. Rozenberg, *Two-dimensional electron gas with universal subbands at the surface of SrTiO₃*, Nature **469**, 189 (2011).

[109] N. C. Plumb, M. Salluzzo, E. Razzoli, M. Månsson, M. Falub, J. Krempasky, C. E. Matt, J. Chang, M. Schulte, J. Braun, H. Ebert, J. Minár, B. Delley, K.-J. Zhou, T. Schmitt, M. Shi, J. Mesot, L. Patthey, and M. Radović, *Mixed dimensionality of confined conducting electrons in the surface region of SrTiO₃*, Phys. Rev. Lett. **113**, 086801 (2014).

[110] C. Cancellieri, M. L. Reinle-Schmitt, M. Kobayashi, V.N. Strocov, P. R. Willmott, D. Fontaine, Ph. Ghosez, A. Filippetti, P. Delugas, and V. Fiorentini, *Doping-dependent band structure of LaAlO₃ / SrTiO₃ interfaces by soft X-ray polarization-controlled resonant angle-resolved photoemission*, Phys. Rev. B **89**, 121412 (2014).

[111] L. W. van Heeringen, G. A. de Wijs, A. McCollam, J. C. Maan, and A. Fasolino, *k · p subband structure of the LaAlO₃ / SrTiO₃ interface*, Phys. Rev. B **88**, 205140 (2013).

[112] L. Mattheiss, *Effect of the* 110 K *phase transition on the SrTiO₃ conduction bands*, Phys. Rev. B **6**, 4740 (1972).

[113] H. Uwe, T. Sakudo, and H. Yamaguchi, *Interband electronic Raman scattering in SrTiO₃*, Jpn. J. Appl. Phys. **24**, 519 (1985).

[114] K. L. Litvinenko, L. Nikzad, C. R. Pidgeon, J. Allam, L. F. Cohen, T. Ashley, M. Emeny, W. Zawadzki, and B. N. Murdin, *Temperature dependence of the electron Landé g factor in InSb and GaAs*, Phys. Rev. B **77**, 033204 (2008).

[115] X.-L. Qi and S.-C. Zhang, *Topological insulators and superconductors*, Rev. Mod. Phys. **83**, 1057 (2011).

[116] B. Yan and C. Felser, *Topological Materials: Weyl Semimetals*, Annu. Rev. Condens. Matter Phys. **8**, 337 (2017).

Bibliography

[117] M. König, H. Buhmann, L. W. Molenkamp, T. L. Hughes, C.-X. Liu, X.-L. Qi, and S.-C. Zhang, *The quantum spin Hall effect: theory and experiment*, J. Phys. Soc. Jpn. **77**, 031007 (2008).

[118] S. Hart, H. Ren, T. Wagner, P. Leubner, M. Mühlbauer, C. Brüne, H. Buhmann, L. W. Molenkamp, and A. Yacoby, *Induced superconductivity in the quantum spin Hall edge*, Nat. Phys. **10**, 638 (2014).

[119] C. W. J. Beenakker, *Andreev reflection and Klein tunneling in graphene*, Rev. Mod. Phys. **80**, 1337 (2009).

[120] Z. Faraei and S. A. Jafari, *Superconducting proximity in three dimensional Dirac materials: odd-frequency, pseudo-scalar, pseudo-vector and tensor-valued superconducting orders*, Phys. Rev. B **96**, 134516 (2017).

[121] Shuhei Uchida, Tetsuro Habe, and Yasuhiro Asano, *Andreev reflection in Weyl semimetals*, J. Phys. Soc. Jpn. **83**, 064711 (2014).

[122] Wei Chen, Liang Jiang, R. Shen, L. Sheng, B. G. Wang, and D. Y. Xing, *Specular Andreev reflection in inversion-symmetric Weyl semimetals*, EPL **103**, 27006 (2013).

[123] U. Khanna, D. K. Mukherjee, A. Kundu, and S. Rao, *Chiral nodes and oscillations in the Josephson current in Weyl semimetals*, Phys. Rev. B **93**, 121409(R) (2016).

[124] K. A. Madsen, E. J. Bergholtz, and P. W. Brouwer, *Josephson effect in a Weyl SNS junction*, Phys. Rev. B **95**, 064511 (2017).

[125] Y. Kim, M. J. Park, and M. J. Gilbert, *Probing unconventional superconductivity in inversion-symmetric doped Weyl semimetal*, Phys. Rev. B **93**, 214511 (2016).

[126] M. Salehi and S. A. Jafari, *Sea of Majorana fermions from pseudoscalar superconducting order in three dimensional Dirac materials*, Sci. Rep. **7**, 8221 (2017).

[127] U. Khanna, A. Kundu, and S. Rao, *0–π transitions in a Josephson junction of irradiated Weyl semimetal*, Phys. Rev. B **95**, 201115(R) (2017).

[128] L. Aggarwal, S. Gayen, S. Das, R. Kumar, V. Süß, C. Felser, C. Shekhar, and G. Sheet, *Mesoscopic superconductivity and high spin polarization coexisting at metallic point contacts on Weyl semimetal TaAs*, Nature Comm. **8**, 13974 (2017).

[129] He Wang, Hu. Wang, Y. Chen, J. Luo, Z. Yuan, J. Liu, Y. Wang, S. Jia, X.-J. Liu, J. Wei, and J. Wang, *Discovery of tip induced unconventional superconductivity on Weyl semimetal*, Science Bull. **62**, 425 (2017).

[130] K.-Y. Yang, Y.-M. Lu, and Y. Ran, *Quantum Hall effects in a Weyl semimetal: possible application in pyrochlore iridates*, Phys. Rev. B **84**, 075129 (2011).

[131] G. Y. Cho, *Possible topological phases of bulk magnetically doped Bi_2Se_3: turning a topological band insulator into Weyl semimetal*, arXiv:1110.1939.

[132] M. M. Vazifeh and M. Franz, *Electromagnetic response of Weyl semimetals*, Phys. Rev. Lett. **111**, 027201 (2013).

[133] M. Titov and C. W. J. Beenakker, *Josephson effect in ballistic graphene*, Phys. Rev. B **74**, 041401(R) (2006).

[134] G. E. Blonder, M. Tinkham, and T. M. Klapwijk, *Transition from metallic to tunneling regimes in superconducting microconstrictions: excess current, charge imbalance, and supercurrent conversion*, Phys. Rev. B **25**, 4515 (1982).

[135] C. W. J. Beenakker, *Specular Andreev reflection in graphene*, Phys. Rev. Lett. **97**, 067007 (2006).

[136] G. Bednik, A. A. Zyuzin, and A. A. Burkov, *Superconductivity in Weyl metals*, Phys. Rev. B **92**, 035153 (2015).

[137] Haijun Zhang, Chao-Xing Liu, Xiao-Liang Qi, Xi Dai, Zhong Fang, and Shou-Cheng Zhang, *Topological insulators in Bi_2Se_3, Bi_2Te_3 and Sb_2Te_3 with a single Dirac cone on the surface*, Nature Phys. **5**, 438 (2009).

[138] L. Fu and E. Berg, *Odd-Parity Topological Superconductors: Theory and Application to $Cu_xBi_2Se_3$*, Phys. Rev. Lett. **105**, 097001 (2010).

[139] G. Y. Cho, J. H. Bardarson, Y.-M. Lu, and J. E. Moore, *Superconductivity of doped Weyl semimetals: Finite-momentum pairing and electronic analog of the ^{3}He-A phase*, Phys. Rev. B **86**, 214514 (2012).

[140] R. Okugawa and S. Murakami, *Dispersion of Fermi arcs in Weyl semimetals and their evolutions to Dirac cones*, Phys. Rev. B **89**, 235315 (2014).

[141] H. Nama, H. Chena, T. Liub, J. Kima, C. Zhang, J. Yong, T. R. Lemberger, P. A. Kratz, J. R. Kirtley, K. Moler, P. W. Adams, A. H. MacDonald, and C.-K. Shih, *Ultrathin two-dimensional superconductivity with strong spin-orbit coupling*, Proc. Natl. Acad. Sci. (USA) **113**, 10513 (2016).

[142] C. W. Groth, M. Wimmer, A. R. Akhmerov, and X. Waintal, *Kwant: A software package for quantum transport*, New J. Phys. **16**, 063065 (2014).

[143] C. W. J. Beenakker and H. van Houten, *Josephson current through a superconducting quantum point contact shorter than the coherence length*, Phys. Rev. Lett. **66**, 3056 (1991).

[144] M. Z. Hasan and H. Lin, *Warping the cone on a topological insulator*, Physics **2**, 10 (2009).

[145] J. Erickson, *Lecture Notes on Computational Topology: Generic and Regular Curves* [http://tinyurl.com/turningnumbers]

[146] C. F. Gauss, *Zur Geometria Situs*, published in: *Werke*, vol. 8, p. 271–281 (Springer, 1900).

[147] Z. Wang, A. Alexandradinata, R. J. Cava, and B. A. Bernevig, *Hourglass fermions*, Nature **532**, 189 (2016).

[148] M. N. Chernodub, *The Nielsen-Ninomiya theorem, PT-invariant non-Hermiticity and single 8-shaped Dirac cone*, J. Phys. A **50**, 385001 (2017).

[149] A. C. Potter, I. Kimchi, and A. Vishwanath, *Quantum oscillations from surface Fermi-arcs in Weyl and Dirac semi-metals*, Nat. Commun. **5**, 5161 (2014).

[150] Y. Zhang, D. Bulmash, P. Hosur, A. C. Potter, and A. Vishwanath, *Quantum oscillations from generic surface Fermi arcs and bulk chiral modes in Weyl semimetals*, Sci. Rep. **6**, 23741 (2016).

[151] D. Bulmash and X.-L. Qi, *Quantum oscillations in Weyl and Dirac semimetal ultra-thin films*, Phys. Rev. B **93**, 081103 (2016).

[152] M. V. Berry and R. J. Mondragon, *Neutrino billiards: Time-reversal symmetry-breaking without magnetic fields*, Proc. R. Soc. London A **412**, 53 (1987).

[153] J. M. Luttinger and W. Kohn, *Motion of electrons and holes in perturbed periodic fields*, Phys. Rev. **97**, 869 (1955).

[154] V. Barsan and V. Kuncser, *Exact and approximate analytical solutions of Weiss equation of ferromagnetism and their experimental relevance*, Phil. Mag. Lett. **97**, 359 (2017).

[155] I. Mező and G. Keady, *Some physical applications of generalized Lambert functions*, Eur. J. Phys. **37**, 065802 (2006).

[156] A. A. Burkov, *Weyl Metals*, Annu. Rev. Condens. Matter Phys. **9**, 359 (2018).

[157] N. P. Armitage, E. J. Mele, and A. Vishwanath, *Weyl and Dirac semimetals in three-dimensional solids*, Rev. Mod. Phys. **90**, 015001 (2018).

[158] F. D. M. Haldane, *Attachment of surface Fermi arcs to the bulk Fermi surface: Fermi-level plumbing in topological metals*, arXiv:1401.0529.

[159] G. E. Zil'berman, *Motion of electron along self- intersecting trajectories*, JETP **7**, 513 (1958).

[160] M. Ya. Azbel', *Quasiclassical quantization in the neighborhood of singular classical trajectories*, JETP **12**, 891 (1961).

[161] L. M. Roth, *Semiclassical theory of magnetic energy levels and magnetic susceptibility of Bloch electrons*, Phys. Rev. **145**, 434 (1966).

[162] A. M. Kosevich, *Topology in the electron theory of metals*, Springer Series in Solid-State Sciences **150**, 3 (2006).

[163] G. P. Mikitik and Yu. V. Sharlai, *Manifestation of Berry's phase in metal physics*, Phys. Rev. Lett. **82**, 2147 (1999).

[164] J. N. Fuchs, F. Piéchon, M. O. Goerbig, and G. Montambaux, *Topological Berry phase and semiclassical quantization of cyclotron orbits for two dimensional electrons in coupled band models*, Eur. Phys. J. B **77**, 351 (2010).

[165] A. Alexandradinata, C. Wang, W. Duan, and L. Glazman, *Revealing the topology of Fermi-surface wave functions from magnetic quantum oscillations*, Phys. Rev. X **8**, 011027 (2018).

[166] A. Alexandradinata and L. Glazman, *Geometric phase and orbital moment in quantization rules for magnetic breakdown*, Phys. Rev. Lett. **119**, 256601 (2017).

[167] B. I. Halperin, *Quantized Hall conductance, current-carrying edge states, and the existence of extended states in a two-dimensional disordered potential*, Phys. Rev. B **25**, 2185 (1982).

[168] M. Büttiker, *Absence of backscattering in the quantum Hall effect in multiprobe conductors*, Phys. Rev. B **38**, 9375 (1988).

[169] H. Yao, M. Zhu, L. Jiang, and Y. Zheng, *Simulation on the electronic wave packet cyclotron motion in a Weyl semimetal slab*, J. Phys. Condens. Matter **29**, 155502 (2017).

[170] C. W. J. Beenakker, H. van Houten, and B. J. van Wees, *Skipping orbits, traversing trajectories, and quantum ballistic transport in microstructures*, Superlatt. Microstruct. **5**, 127 (1989).

[171] G. Montambaux, *Semiclassical quantization of skipping orbits*, Eur. Phys. J. B **79**, 215 (2011).

[172] J. Tworzydło, B. Trauzettel, M. Titov, A. Rycerz, and C. W. J. Beenakker, *Sub-Poissonian shot noise in graphene*, Phys. Rev. Lett. **96**, 246802 (2006).

[173] M. Koshino, *Cyclotron resonance of figure-of-eight orbits in a type*-II *Weyl semimetal*, Phys. Rev. B **94**, 035202 (2016).

[174] Y. Gao and Q. Niu, *Zero-field magnetic response functions in Landau levels*, Proc. Natl. Acad. Sci. U. S. A. **114**, 7295 (2017).

[175] Y. Zhang, Y.-W. Tan, H. L. Stormer, and P. Kim, *Experimental observation of the quantum Hall effect and Berry's phase in graphene*, Nature **438**, 201 (2005).

[176] L. P. He, X. C. Hong, J. K. Dong, J. Pan, Z. Zhang, J. Zhang, and S. Y. Li, *Quantum transport evidence for the three-dimensional Dirac semimetal phase in Cd_3As_2*, Phys. Rev. Lett. **113**, 246402 (2014).

[177] X. Huang, L. Zhao, Y. Long, P. Wang, D. Chen, Z. Yang, H. Liang, M. Xue, H. Weng, Z. Fang, X. Dai, and G. Chen, *Observation of the chiral-anomaly-induced negative magnetoresistance in 3D Weyl semimetal TaAs*, Phys. Rev. X **5**, 031023 (2015).

[178] J. Hu, Z. Tang, J. Liu, X. Liu, Y. Zhu, D. Graf, K. Myhro, S. Tran, C. N. Lau, J. Wei, and Z. Mao, *Evidence of topological nodal-line fermions in ZrSiSe and ZrSiTe*, Phys. Rev. Lett. **117**, 016602 (2016).

[179] S. Pezzini, M. R. van Delft, L. Schoop, B. Lotsch, A. Carrington, M. I. Katsnelson, N. E. Hussey, and S. Wiedmann, *Unconventional mass enhancement around the Dirac nodal loop in ZrSiS*, Nat. Phys. **14**, 178 (2017).

[180] A. A. Burkov, *Topological semimetals*, Nat. Mater. **15**, 1145 (2016).

[181] M. H. Cohen and L. M. Falicov, *Magnetic breakdown in crystals*, Phys. Rev. Lett. **7**, 231 (1961).

[182] M. I. Kaganov and A. A. Slutskin, *Coherent magnetic breakdown*, Phys. Rep. **98**, 189 (1983).

[183] J. B. Keller, *Corrected Bohr-Sommerfeld quantum conditions for nonseparable systems*, Ann. Phys. (N. Y.). **4**, 180 (1958).

[184] G. Panati, H. Spohn, and S. Teufel, *Effective dynamics for Bloch electrons: Peierls substitution and beyond*, Commun. Math. Phys. **242**, 547 (2003).

[185] D. Xiao, M.-C. Chang, and Q. Niu, *Berry phase effects on electronic properties*, Rev. Mod. Phys. **82**, 1959 (2010).

[186] Z.-M. Yu, Y. Yao, and S. A. Yang, *Predicted unusual magnetoresponse in type-II Weyl semimetals*, Phys. Rev. Lett. **117**, 077202 (2016).

[187] S. Tchoumakov, M. Civelli, M. O. Goerbig, *Magnetic-field-induced relativistic properties in type-I and type-II Weyl semimetals*, Phys. Rev. Lett. **117**, 086402 (2016).

[188] M. Udagawa and E.J. Bergholtz, *Field-selective anomaly and chiral mode reversal in type-II Weyl materials*, Phys. Rev. Lett. **117**, 086401 (2016).

Bibliography

[189] L. D. Landau and E. M. Lifshitz, Course of Theoretical Physics (Elsevier, Oxford, 1977).

[190] G. P. Mikitik and Y. V. Sharlai, *Semiclassical energy levels of electrons in metals with band degeneracy lines*, J. Exp. Theor. Phys. **87**, 747 (1998).

[191] G. P. Mikitik and Y. V. Sharlai, *Magnetic susceptibility of topological nodal semimetals*, Phys. Rev. B **94**, 195123 (2016).

[192] N. Bovenzi, M. Breitkreiz, T. E. O'Brien, J. Tworzydło, and C. W. J. Beenakker, *Twisted Fermi surface of a thin-film Weyl semimetal*, New J. Phys. **20**, 023023 (2018).

[193] A. Alexandradinata and L. I. Glazman, *Semiclassical theory of Landau levels and magnetic breakdown in topological metals*, Phys. Rev. B **97**, 144422 (2018).

Summary

Electrons in a crystal lattice have properties that may differ from those of a free electron in vacuum. The effective mass can be different from the bare electron mass, and it may even vanish, so that the electron behaves in some respects as a relativistic massless particle such as a photon. The magnetic moment of the intrinsic angular momentum, the electron spin, may be also different from that of an elementary particle. Moreover, electrons can acquire spin-like degrees of freedom, referred to as "lattice pseudospin" or "valley isospin".

These various degrees of freedom are of interest as ways to store and transport information — one speaks of "spintronics" and "valleytronics" as alternatives to "electronics" — and they have recently gained additional relevance in the context of topological quantum phases. For those purposes it is of interest to study the interplay between the orbital motion of electrons and their spin (spin-like) degrees of freedom, the so-called "spin-orbit coupling".

This thesis contains results about the effects of strong spin-orbit coupling, and in particular of the "spin-momentum locking", on two classes of materials: oxide-interfaces and Weyl semimetals.

The high-mobility two-dimensional electron system at the (strontium-titanate / lanthanum-aluminate) $LaAlO_3$ / $SrTiO_3$ interface is endowed with many properties that have no analogues in conventional semiconductor-heterostructures. The interface can indeed carry electrical current despite $LaAlO_3$ and $SrTiO_3$ being both insulators, and it becomes superconducting at sub-Kelvin temperatures.

There is an ongoing search for the connection between superconductivity, on the one hand, and spin-orbit coupling and inversion-symmetry breaking, on the other hand. This requires a good characterization of the spin-orbit coupling. Previous studies in the literature dismissed this effect as being too weak to produce observable signatures in the transport properties of the interface, which were instead related to many-body interactions. In a collaboration with experimentalists in Delft, we found evidence that the experimentally measured giant negative magnetoresistance may be a single-particle effect, driven by spin-orbit coupling.

In chapter two of this thesis, we show that also the anisotropy of the

magnetoresistance can be likewise explained. Remarkably, we found that the amplitude and the shape of the magnetoresistance oscillations directly map to the spin and orbital textures of the Bloch states at the Fermi level.

From chapter three onwards, the focus shifts to Weyl semimetals. These are three-dimensional materials with the unique combination of gapless linear dispersion in the bulk ("three-dimensional graphene") and topological surface states (Fermi arcs). In the absence of time-reversal and/or spatial-inversion symmetry, the band-degeneracy points, so-called "Weyl nodes", are robust against local perturbations and carry a definite "chirality".

In this thesis, we have studied "magnetic" Weyl semimetals — time-reversal symmetry is intrinsically broken — with a single pair of Weyl cones in the Brillouin zone. Chiral Weyl fermions have the spin tied to the direction parallel or antiparallel to the momentum. Type–I Weyl semimetals, with a point-like Fermi surface at the energy of the Weyl nodes, are the subject of chapters three and four. In chapter five we extend our study to type-II Weyl points, created when the Weyl cone is tipped over the momentum axis, and to multi-Weyl points that have topological charge larger than one.

In chapter three, we show that at the interface between a magnetic Weyl semimetal and an *s*-wave spin-singlet superconductor, Andreev reflection is blocked. The reason is that the combined requirements of zero momentum and zero spin transfer to the Cooper pairs are at odds with the spin-momentum locking of the Weyl fermions.

In chapter four, we investigate the magnetotransport signatures of the figure–8 Fermi surface formed out of hybridized surface and bulk states in a thin film of a magnetic Weyl semimetal with additionally broken inversion-symmetry. In a strong perpendicular magnetic field, two types of counterpropagating edge channels coexist at each spatial boundary of the system, distinguished in "narrow" and "wide" channels depending on how much they extend into the bulk. Through a voltage bias one can selectively populate either the wide or the narrow channel, while the current flow shifts from one edge to the opposite upon reversing the direction of the field. These signatures are unique to the figure–8 Fermi surface and can be observed in magnetoconductance experiments.

In chapter five, we calculate the quantum corrections to the Bohr-Sommerfeld quantization condition of cyclotron orbits encircling different types of Weyl points. These corrections shift the phase of magnetic oscillations of quantities such as the magnetization and the conductance. The total phase is the sum of several contributions: the Maslov phase due to the caustics on the cyclotron orbit, the Berry phase that carries information about the topology of the band-structure, and the phase

associated with tunneling between different orbits that merge into one via magnetic breakthrough. We find that for figure–8 cyclotron orbits at multi-Weyl points the phase shift is nicely quantized due to cancellation of non-universal contributions between the electron and hole part of the orbit.

Samenvatting

Elektronen in een kristal hebben eigenschappen die kunnen verschillen van de eigenschappen van vrije elektronen in vacuüm. De effectieve massa kan verschillen van de vrije elektronenmassa, en deze kan zelfs nul worden, zodat het elektron in sommige opzichten beweegt zoals een relativistisch massaloos deeltjes als een foton zou bewegen. Het magnetische moment van het intrinsieke draaimpuls, de elektronenspin, kan ook verschillen van dat van een elementair deeltje. Bovendien kunnen elektronen spin-achtige vrijheidsgraden ontwikkelen, genaamd "pseudospin" of "isopspin".

Al deze vrijheidsgraden zijn interessant omdat men er informatie in kan opslaan en mee kan vervoeren — men spreekt van "spintronics" en "valleytronics" als alternativen voor "electronics" — en recent zijn ze van belang geworden in de contekst van topologische quantumtoestanden. Om deze redenen is het van belang om het samenspel te onderzoeken tussen de ruimtelijke beweging van de elektronen en hun spin (of spinachtige) vrijheidsgraden. Dit heet "spin-baankoppeling".

Dit proefschrift bevat het resultaat van onderzoek naar de effecten van sterke spin-baankoppeling, in het bijzonder de gevolgen van "spin-momentum locking", in twee klassen van materialen: oxide-grenslagen en Weyl halfmetalen.

Wat betreft de oxide-grenslagen is onze aandacht uitgegaan naar het $LaAlO_3$ / $SrTiO_3$ (strontium-titanaat / lanthaan-aluminaat) grensvlak, dat een twee-dimensionaal elektronengas bevat met hoge mobiliteit. Het is een uniek systeem, met eigenschappen die niet in andere halfgeleider heterostrukturen voorkomen. Hoewel $LaAlO_3$ and $SrTiO_3$ isolatoren zijn, kan het grensvlak toch geleidend worden, en zelfs supergeleidend bij temperaturen onder 1 Kelvin.

Men is actief op zoek naar het verband tussen supergeleiding enerzijds, en spin-baankoppeling vanwege gebroken inversiesymmetrie anderzijds. Hiervoor is een goed begrip van de spin-baankoppeling nodig. Eerdere studies in de literatuur hebben dit effect afgedaan als te zwak om van invloed te kunnen zijn op de geleiding in het grensvlak. Men legde in plaats daarvan de nadruk op de effecten van interacties tussen de elektronen. In samenwerking met experimentatoren in Delft hebben we aanwijzigen gevonden dat de gemeten grote magnetoweerstand gedreven wordt door

de spin-baankoppeling, zelfs in afwezigheid van interacties.

In hoofdstuk twee van dit proefschrift laten we zien dat de anisotropie van de magnetoweerstand ook op deze manier kan worden verklaard. We hebben gevonden dat de amplitude en de vorm van de magnetoweerstand-oscillaties direct gerelateerd zijn aan de spin-baankoppeling in Blochtoestanden aan het Fermi-niveau.

Vanaf hoofdstuk drie richten we ons op Weyl halfmetalen. Dit zijn drie-dimensionale materialen met de bijzondere combinatie van een lineaire dispersie binnenin het materiaal ("drie-dimensionaal grafeen") en topologische toestanden aan het oppervlak ("Fermi arcs"). In de afwezigheid van tijdomkeersymmetrie en/of inversiesymmetrie heeft de bandstruktuur een conische vorm met snijpunten, zogenaamde "Weyl nodes", die ongevoelig zijn voor lokale verstoringen en een bepaalde "chiraliteit" bezitten.

In dit proefschrift hebben we "magnetische" Weyl halfmetalen onderzocht (dus met gebroken tijdomkeersymmetrie), die een enkel paar Weyl conussen hebben in de Brillouinzone. Chirale Weylfermionen hebben een spin die is uitgelijnd met de impuls, parallel of antiparallel. Weyl halfmetalen van type I, met een puntvormig Fermi-oppervlak, zijn het onderwerp van hoofdstuk drie en vier. In hoofdstuk vijf breiden we de studie uit naar type II, waarin de Weyl conus is gekanteld, en naar Weylfermionen met een topologische lading groter dan één (hogere orde Weylpunten).

In hoofdstuk drie laten we zien dat er geen Andreev-reflectie optreedt aan het grensvlak tussen een magnetisch Weyl halfmetaal en een conventionele supergeleider (*s*-wave spin-singlet). De reden hiervoor is dat de vereisten van afwezigheid van transport van impuls of spin aan de Cooperparen niet te rijmen zijn met de "spin-momentum locking" van de Weylfermionen.

In hoofdstuk vier onderzoeken we het magnetotransport in een Fermi-oppervlak dat een 8-vorm heeft. Dit treedt op in een dunne film van een magnetisch Weyl halfmetaal waarin eveneens de inversiesymmetrie is gebroken. De kruising in de "8" is het gevolg van menging van toestanden aan het oppervlak van de dunne film en binnenin. In een sterk loodrecht magnetisch veld ontstaan twee type van randkanelen, die in tegengestelde richting bewegen: het ene type is nauw, het andere breed, afhankelijk van hoe diep het randkanaal zich in het binnenste van het materiaal uitstrekt. Door middel van een aangelegde spanning kan men selectief het nauwe of het brede randkanaal bevolken, en de elektrische stroom kan zo van de ene naar de andere rand verschoven worden door de richting van het magneetveld te inverteren. Deze effecten zijn karakteristiek voor de 8-vorm van het Fermi-oppervlak en zouden gemeten kunnen worden.

In hoofdstuk vijf bereken we de quantumcorrecties op de Bohr-Sommerfeld quantisatieregel voor cyclotronbeweging in verschillende soorten Weylpun-

ten. Deze correcties verschuiven de fase van de magneto-oscillaties van grootheden zoals de magnetisatie of de geleiding. De faseverschuiving heeft verschillende bijdragen: er is de Maslov-fase ten gevolge van de brandpunten in de cyclotronbaan, er is de Berry-fase die informatie bevat over de topologie van de bandstruktuur, en er is de fase ten gevolge van tunnelen tussen banen dicht bij het Weylpunt ("magnetic breakthrough"). We vinden dat voor de 8-vormige cyclotronbanen de faseverschuiving bij een hogere orde Weylpunt goed gequantiseerd is, ten gevolge van het wegvallen van bijdragen van elektronen en van gaten.

Curriculum Vitæ

I was born in Capua, Italy, on March 23rd 1989. I spent my childhood and most of my youth in Calvi Risorta, a town in the south of Italy where I attended primary school. I received the secondary education with a focus on scientific-oriented studies at the "Liceo Scientifico Leonardo Da Vinci".

In September 2007, I enrolled in the Physics Department at "Sapienza, University of Rome", where I completed my bachelor's studies in 2011 with the thesis *Statistical physics of systems with long-range interactions* (advisor Andrea Gabrielli). Then I started a master in Condensed Matter Physics at the same University, where I graduated cum laude in January 2014 with the thesis *Inhomogeneous quantum Hall states in oxide interfaces with strong Rashba spin-orbit interaction* (advisors Marco Grilli and Sergio Caprara). After my graduation I continued this research project for another half a year.

In October 2014 I started my employment at Leiden University, as a Ph.D. student in the group of Carlo Beenakker. The results of my research are described in this thesis. For the study of oxide interfaces I collaborated with experimental physicists in the group of Andrea Caviglia at the Kavli Institute of Nanoscience in Delft. My research on Weyl semimetals was performed in collaboration with Jakub Tworzydło from Warsaw University.

In the past four years I had the opportunity to attend several schools and workshops, to present my work in the Netherlands, France, Ukraine, Italy, Germany, and Spain.

I served as a teaching assistant to the bachelor's course "Solid-state physics" and to the master's course "Quantum theory".

In the years 2017–2018 I was Leiden's representative at the PhD Student Council of the Dutch Research School of Theoretical Physics.

List of publications

- M. Diez, A.M.R.V.L. Monteiro, G. Mattoni, E. Cobanera, T. Hyart, E. Mulazimoglu, N. Bovenzi, C.W.J. Beenakker, and A.D. Caviglia. *Giant negative magnetoresistance driven by spin-orbit coupling at the LAO/STO interface.* Phys. Rev. Lett. **115**, 016803 (2015).

- N. Bovenzi, F. Finocchiaro, N. Scopigno, D. Bucheli, S. Caprara, G. Seibold, and M. Grilli. *Possible mechanisms of electronic phase separation in oxide interfaces.* J. Supercond. Nov. Magn. **28**, 1273 (2015).

- N. Bovenzi, S. Caprara, M. Grilli, R. Raimondi, N. Scopigno, and G. Seibold. *Density inhomogeneities and Rashba spin-orbit coupling interplay in oxide interfaces.* J. Phys. Chem. Solids https://doi.org/10.1016/j.jpcs.2017.09.013 (2017).

- N. Bovenzi and M. Diez. *Semiclassical theory of anisotropic transport at LaAlO$_3$/SrTiO$_3$ interfaces under in-plane magnetic field.* Phys. Rev. B **95**, 205430 (2017). [Chapter 2]

- N. Bovenzi, M. Breitkreiz, P. Baireuther, T.E. O'Brien, J. Tworzydło, I. Adagideli, and C.W.J. Beenakker. *Chirality blockade of Andreev reflection in a magnetic Weyl semimetal.* Phys. Rev. B **96**, 035437 (2017). [Chapter 3]

- N. Bovenzi, M. Breitkreiz, T.E. O'Brien, J. Tworzydło, and C.W.J. Beenakker. *Twisted Fermi surface of a thin-film Weyl semimetal.* New J. Phys. **20**, 023023 (2018). [Chapter 4]

- M. Breitkreiz, N. Bovenzi, and J. Tworzydło. *Phase shift of cyclotron orbits at type-I and type-II multi-Weyl nodes.* Phys. Rev. B **98**, 121403(R) (2018). [Chapter 5]

Stellingen

behorende bij het proefschrift
*"Spin-momentum locking in oxide interfaces
and in Weyl semimetals"*

1. The large anisotropic magnetoresistance measured in LAO / STO interfaces can be explained in terms of a single-particle scattering mechanism, without relying on the Kondo effect.

    Chapter 2

2. Andreev reflection at the interface between a time-reversal–symmetry breaking Weyl semimetal and an *s*-wave superconductor requires a pseudoscalar pair potential, that changes sign under inversion symmetry.

    Chapter 3

3. In a two-dimensional electron gas, a deformation of the Fermi circle that changes the turning number can be observed in the magnetoconductance.

    Chapter 4

4. Magnetic breakthrough between the electron and hole cyclotron orbits in a type–II Weyl semimetal is associated with a $\pi/2$ phase shift.

    Chapter 5

5. Non-Abelian exchange statistics does not apply to Majorana fermions.

6. The collision integral in the Boltzmann transport equation is linear in the distribution function regardless of any assumption of detailed balance, contrary to textbook statements.

    N. W. Ashcroft and N. D. Mermin, *Solid State Physics*, Saunders (1976).

7. The correspondence between Klein tunneling and Andreev reflection discussed by Beenakker *et al.* [Phys. Rev. B **77**, 075409 (2008)] can be extended to explain the universal phase shift of $\pi/2$ acquired by the electron wave function upon a magnetic breakthrough transition of the type studied in Chapter 5.

8. The electrical current through a slab of Weyl semimetal can mainly flow along the boundaries, even if there are many more bulk states than surface states at the Fermi level.

9. The quasi-Majorana states studied by Vuik *et al.* [arXiv:1806.02801] in topologically trivial semiconductor nanowires may serve more efficiently as building blocks of quantum gates than topologically non-trivial Majorana zero-modes.

<center>

Nicandro Bovenzi

23 October 2018

</center>